STARS

University of Central Florida
STARS

Electronic Theses and Dissertations, 2020-

2020

Study on Comprehensive Mechanical Properties of Metallic Matrix CNT Nano-composites

Shutao Song
University of Central Florida

Part of the Mechanical Engineering Commons
Find similar works at: https://stars.library.ucf.edu/etd2020
University of Central Florida Libraries http://library.ucf.edu

This Doctoral Dissertation (Open Access) is brought to you for free and open access by STARS. It has been accepted for inclusion in Electronic Theses and Dissertations, 2020- by an authorized administrator of STARS. For more information, please contact STARS@ucf.edu.

STARS Citation
Song, Shutao, "Study on Comprehensive Mechanical Properties of Metallic Matrix CNT Nano-composites" (2020). *Electronic Theses and Dissertations, 2020-*. 418.
https://stars.library.ucf.edu/etd2020/418

STUDY ON COMPREHENSIVE MECHANICAL PROPERTIES OF METALLIC MATRIX CNT NANO-COMPOSITES

by

SHUTAO SONG
M.S. University of Central Florida, 2018
B.S. Dalian University of Technology, China, 2015

A dissertation submitted in partial fulfillment of the requirements
for the degree of Doctor of Philosophy
in the Department of Mechanical and Aerospace Engineering
in the College of Engineering and Computer Science
at the University of Central Florida
Orlando, Florida

Fall Term
2020

Major Professor: Yuanli Bai

© 2020 Shutao Song

ABSTRACT

Carbon nanotubes (CNT) have excellent mechanical strengths, electrical conductivity, and thermal conductivity. CNT reinforced metallic nano-composites are viewed as a great candidate to replace traditional alloy materials. It has been shown that CNTs can greatly enhance the strength, thermal conductivity, and electrical conductivity of composites. However, the ductility of composites would deteriorate due to the addition of CNTs if the fabrication or/and processing methods are not improved or well designed. This dissertation investigated (1) the strengthening mechanisms of CNT on metallic matrix, such as mechanical strength and thermal conductivity, and (2) analytical modeling on the strength-ductility trade-off of CNT reinforced composites under different temperatures and loading conditions. This work involves many experiments, finite element (FE) simulations, and analytical model studies. In experiments, different types of pure copper specimens were designed and tested under a wide range of loading conditions. These experimental data provided the baseline of pure copper's ductility characteristics for composite study. Both analytical method and finite element analysis were used to study the strengthening mechanisms of CNT reinforced aluminum matrix composites. For the analytical analysis, the Orowan looping effect, thermal mismatch effect, and load bearing effect are considered all together. A series of finite element analyses using representative volume element (RVE) method were conducted considering influences of CNTs aspect ratios, volume fraction of hardened zone, and the hardened plastic strain of hardened zone. The results show that the aspect ratio of CNTs is very important in the strengthening of CNT reinforced nano-composites. A digital workflow was proposed to investigate the mechanical and thermal properties of composites, and a three dimensional (3D) RVE method was implemented for the analysis and achieved better accuracies. The influence of CNT anisotropy was also studied based on the digital workflow. At last, the strength-ductility trade-off

phenomenon was thoroughly investigated, and a new analytical solution considering different loading conditions and elevated temperatures was proposed and verified by experimental data of Cu/CNTs.

KEYWORDS: Metal Matrix Composites, Carbon Nanotube, Finite Element Analysis, Representative Volume Element, Material Strength, Strength-Ductility Trade-off, Thermal Conductivity, Interface

ACKNOWLEDGEMENT

First of all, I would like to express my sincere gratitude to my academic advisor, Professor Yuanli Bai, for his guidance, encouragement, and patience through the past years of my study at the University of Central Florida (UCF). I am extremely grateful for Professor Bai's suggestions and daily discussions throughout my doctoral research and this dissertation would not have been possible without his help. Partial financial supports from the U.S. Department of Energy and UCF are greatly appreciated.

I would love to thank my committee members: Professor Kawai Kwok, Professor Quanfang Chen, and Professor Kevin Mackie. Their guidance and suggestions are valuable to me and their insightful advice inspires me in different areas of my research. I would also like to thank Professor Jihua Gou. He is always ready to answer my questions about graduate study. Special thanks go to Dr. Md Muktadir Billah, Dr. Liangfu Zheng, and Dr. Luyang Ren for their help on the fabrication of carbon nanotube reinforced metal matrix composites.

My life at UCF would be less fantastic without the companion and help of my colleagues from the Lab of Solid and Structure Mechanics: Dr. Mohammed Algarni, Dr. Yangyang Qiao, Dr. Sami Ghazali, Dr. Hao Pan, Ms. Erin Shoemaker, Mr. Qiang Zhou, Dr. Xu He, Mr. Sami Musalli, and Ms. Yeting Sun. I will miss the days spent in the Lab of Solid and Structure Mechanics. Particularly, I would like to acknowledge Dr. Yangyang Qiao and Dr. Hao Pan for their help on both experiments and modeling work.

Finally, I want to express my deepest gratitude to my parents. They always support me and have faith in me.

TABLE OF CONTENTS

LIST OF FIGURES ix

LIST OF TABLE xix

CHAPTER 1 INTRODUCTION 1

1.1 Background 1

1.2 Motivation and Objectives 2

1.3 Outline of the thesis 3

CHAPTER 2 LITERATURE REVIEW 7

2.1 Mechanical Properties of CNT composites 7

2.2 Thermal Conductivity of CNT Composites 16

CHAPTER 3 PLASTICITY AND DUCTILITY OF PURE COPPER 20

3.1 Experiment Method 23

3.1.1 Specimen Design 23

3.1.2 Experiments 27

3.2 Plasticity Model and Fracture Criterion 29

3.3 Calibration of Material Models 35

3.3.1 Linear Function of Hydrostatic Pressure Effect 36

3.3.2 Piecewise Function of Hydrostatic Pressure Effect 52

3.4 Summary 54

CHAPTER 4 STRENGTHENING MECHANISM OF NICKEL COATED AL/CNT COMPOSITES 56

4.1 Experimental Results 56

4.2 Finite Element Simulation using RVE 59

4.2.1 Model Setup 59

4.2.2 Mechanical Properties of Aluminum Matrix 62

4.2.3 Mechanical Properties of CNTs and Nickel Coating 63

4.3 Simulation Results and Parametric Studies 65

4.3.1 Effects of CNTs Aspect Ratio, Hardened Zone Volume Fraction, and Residual Plastic Strain 66

4.3.2 Correlations between FE Simulations and Experimental Results 71

4.4 Analytical Solutions of Strengthening Effects 72

CHAPTER 5 DIGITAL WORKFLOW OF 3D RVE MODEL 78

5.1 Methodology 78

5.2 Toolbox Interface 88

5.2.1 Preprocessing Phase for Model Setup 88

5.2.2 Postprocessing Phase of Simulations 92

5.3 Application Examples 93

5.3.1 Influence of Anisotropy and Interface on Elasticity 93

5.3.2 Plasticity of Metal Matrix Composites 98

CHAPTER 6 THERMAL CONDUCTIVITY OF CU/CNT COMPOSITES 102

6.1 Methodology 103

6.1.1 Random Sequential Adsorption Procedure 103

6.1.2 Model Assumptions and Boundary Conditions 104

6.2 Results and Discussions 105

6.2.1 Model Validation 106

6.2.2 Influence of Porosity 107

6.2.3 Composites with a better Thermal Conductivity of Inclusions 111

6.3 Summary 118

CHAPTER 7 STRENGTH AND DUCTILITY TRADE-OFF OF COMPOSITES 121

7.1 Theoretical Models of Strengthening Mechanism and Ductility of CNT Reinforced Metal Matrix Composites 121

7.1.1 Theoretical Model of Strengthening Mechanism with Temperature Effects..... 121

7.1.2 An sMMC Model Based Theoretical Model for Ductility Loss of Nano Composites 124

7.2 Model Prediction for Cu/CNT Nano Composites 130

7.3 Model Prediction for Al/NiCNT Nano Composites..... 138

7.4 Summary 143

CHAPTER 8 CONCLUSIONS AND FUTURE STUDIES 145

REFERENCES 148

LIST OF FIGURES

Figure 1. Comparison of strengthening effects among metal matrix composites with different strengthening inclusions. It presents that CNT reinforced composites have a great strengthening effect. Ref: (Chai et al., 2008; B Chen, Kondoh, Li, & Qian, 2020; F. Chen et al., 2016; HJ Choi, Shin, & Bae, 2011; Hyunjoo Choi, Shin, Min, Park, & Bae, 2009; Cöcen & Önel, 2002; Fan et al., 2018; Ferkel & Mordike, 2001; Fu, Chen, & Liu, 2020; Hwang et al., 2013; P. Li, Chen, & Qin, 2017; Jiapeng Liu et al., 2018; Nie, Deng, Wang, & Wu, 2017; Reddy et al., 2017; Saravanan & Surappa, 2000; Shin, Choi, Shin, & Bae, 2015; H. Wang et al., 2018; Xu et al., 2017; D. Zhang & Zhan, 2016; H. Zhang et al., 2017; C. Zhao & Wang, 2014) 8

Figure 2. A comparison of yield stress and fracture strain for different composites (CNT reinforced composites, graphene reinforced composites, and SiC reinforced composites). The yield strength ratio is defined as the yield stress of composites versus that of the corresponding matrix, and the fracture strain ratio is defined as the fracture strain of composites versus that of the corresponding matrix. The results show that nano composite materials are usually strengthened by the compromise of ductility loss. Data took from Ref: (Chai et al., 2008; B Chen et al., 2020; F. Chen et al., 2016; HJ Choi et al., 2011; Hyunjoo Choi et al., 2009; Cöcen & Önel, 2002; Fan et al., 2018; Ferkel & Mordike, 2001; Fu et al., 2020; He et al., 2020; Hwang et al., 2013; P. Li et al., 2017; Jiapeng Liu et al., 2018; Nie et al., 2017; Reddy et al., 2017; Saravanan & Surappa, 2000; Shin et al., 2015; H. Wang et al., 2018; Xu et al., 2017; D. Zhang & Zhan, 2016; H. Zhang et al., 2017; C. Zhao & Wang, 2014) 9

Figure 3. CAD drawings and dimensions of tensile and torsional specimens. 24

Figure 4. CAD drawings and dimensions of compression specimens 24

Figure 5. Machined samples of OFHC copper 24

Figure 6. Round notched bars (Bai, 2007) 25

Figure 7. MTS Bionix EM torsion test system setup for torsion test. 28

Figure 8. The force-displacement curves for different specimens. (a). shows the results for all the tensile specimens; (b). shows the results for both compression specimens; (c). shows the result of the torsional specimen test. 28

Figure 9. Schematic representation of three types of coordinate systems in the space of principal stresses (Bai & Wierzbicki, 2008) 30

Figure 10. An example of the $f\theta$ function of parameter $c\theta s$ which is Lode angle parameter (θ) dependent on the material plasticity 34

Figure 11. Finite element mesh convergency study of uniaxial tension simulation. The results show that the mesh size of 0.25 mm is fine enough. 39

Figure 12. Finite element mesh convergence study for small compression cylinder. The results show that the mesh size of 0.5 mm is fine enough. 39

Figure 13. Finite element mesh convergence study for torsion simulation. The results show that the mesh size of 0.1 mm can provide a convergent result when the plastic deformation is not too large ($rotation \leq 300o$). When the plastic deformation is very large, the results are not exactly the same. For instance, there is a 1.9% difference of the resultant torque for the two mesh sizes when the rotation=$450o$. Shear deformation is essentially a localized phenomenon, and this means that mesh size would have an important influence on the simulations. To keep the computational time at a reasonable level, a mesh size of 0.1 mm is used. 40

Figure 14. Finite element meshes of different types of specimens. 40

Figure 15. Comparison between experiment and simulation for smooth round tension bar. 42

Figure 16. Comparison between experiment and simulation for large notch tensile bar. 42

Figure 17. Comparison between experiment and simulation for sharp notch tensile bar. 43

Figure 18. Comparison between experiment and simulation for large compression bar..... 43

Figure 19. Comparison between experiment and simulation for small compression bar. 44

Figure 20. Comparison between experiment and simulation for torsion bar test. 44

Figure 21. Numerical stress triaxiality vs. equivalent plastic strain in the necking center of each tensile specimen, and numerical stress triaxiality vs. equivalent plastic strain in the edge of torsion specimen. 45

Figure 22. Numerical results of the Lode angle parameter vs. equivalent plastic strain in the necking center of each tensile specimen, and numerical stress triaxiality vs. equivalent plastic strain in the edge of torsion specimen..... 46

Figure 23. Comparison among calibrated MMC ductile fracture locus, theoretical values, and simulation results. Note that the used stress triaxiality values for the theoretical values of tension are assumed to be constant..... 48

Figure 24. stress triaxiality and Lode angle parameter history of three tensile specimens from the necking edge element..... 49

Figure 25. Calibrated MMC 3D fracture locus corresponding to monotonic testing results of OFHC copper..... 51

Figure 26. Evolution of yield locus with PPL plasticity model correction under plane stress loading condition. 51

Figure 27. The initial yield surface in the deviatoric stress plane 52

Figure 28. Comparison between experiment and simulation for (a). compression bars and (b). torsion bar. 53

Figure 29. The initial yield surface in the deviatoric stress plane with the calibrated PPL plasticity model parameters 54

Figure 30. (a). Ni-coated CNTs where CNTs are fully encapsulated. (b). An example of the fracture surface of Al/NiCNTs nano-composites showing no interface debonding during loading. 57

Figure 31. Calibrated engineering stress-strain curves of both pure aluminum and Al/NiCNTs with different weight fractions of NiCNTs 59

Figure 32. A sketch of RVE model for Al/NiCNT nano-composites 61

Figure 33. A simulation flow chart for parametric studies 61

Figure 34. Comparison of engineering plastic strain- stress curves between experiment and simulation for pure aluminum matrix. A good correlation is achieved. 63

Figure 35. True stress-strain curve of CNT used in finite element simulations. Data adapted from Ref. (Long et al., 2015) 64

Figure 36. Stress-strain relationship of pure nickel used in simulations. Data adapted from Ref. (Ayer et al., 2014) 65

Figure 37. Convergence study of mesh size in FE simulations which shows that a minimum mesh size of 0.056nm is fine enough. 66

Figure 38. (a). An example result of the RVE model (axisymmetric elements) which shows the contour plot of effective plastic strain distribution at different overall tensile strains. The plastic strain which concentrates at the interface zone is an important factor of the material strengthening and fracture initiation. (b). The zoomed plastic strain contour plot at the last loading step in 3D space. 68

Figure 39. Simulation results of the initial yield stress of Al/NiCNTs for different aspect ratios, different volume fraction of hardened zone, and different hardened/residual plastic strain of

interfacial aluminum. The z-axis is the initial yield stress of nano-composites (σy) normalized by the initial yield stress of pure aluminum ($\sigma 0 = 72$MPa). 70

Figure 40. Simulation results of initial yield stresses of Al/NiCNTs under different aspect ratios and different hardened/residual plastic strain of interfacial aluminum. The z-axis is the initial yield stress of nano-composites (σy) normalized by the initial yield stress of pure aluminum ($\sigma 0 = 72$MPa). 70

Figure 41. Engineering stress-strain curves from FE simulations, which are close to the range of experiment data (0.5% wt. and 1.0% wt. NiCNT aluminum composites). 71

Figure 42. Comparisons between test results and FE simulations. A very good correlation is achieved. 72

Figure 43. Comparisons between experiments and analytical solutions. A very good correlation was achieved 76

Figure 44. The effect of different influencing factors on CNT reinforced aluminum matrix based on Eq. (34). Orowan looping is the most important among the three strengthening factors. 77

Figure 45. Influence of CNT diameter on the strengthening effect of aluminum composites based on the analytical solution. It shows that smaller diameter can greatly enhance the strength of CNT reinforced aluminum composites 77

Figure 46. 3D RVE modeling procedures. V_f represents the designated volume fraction of inclusions; C(x,y,z) is the randomly generated inclusion location in the 3D space. 79

Figure 47. A diagrammatic sketch to show the arrangement of inclusions intersecting with RVE boundary planes. 83

Figure 48. An example of the RVE model with transversely isotropic properties of inclusions. (a) represents an RVE model with local coordinate systems that are created for inclusions; (b) shows the orientations of material properties of inclusions. 85

Figure 49. (a) An RVE model with different material properties which are represented by different colors. Shared faces are formed between the matrix and all interfaces and between all interfaces and all inclusions to generate shared nodes in the meshing period. (b) A zoom-in view between an inclusion and an interface. 86

Figure 50. A diagrammatic sketch of the RVE model for the demonstration of boundary conditions. The bottom, left, and back surfaces are assumed to be symmetric. The finite element nodes on the other three surfaces (Front F, Right R, and Top T) are constrained to have the same displacement along the normal directions of the corresponding surface. 87

Figure 51. The interface of the *3D RVE Toolbox* plug-in for mechanical analysis. This plug-in considers the influence of interface. The interface plays an important role in metal matrix composites due to, for example, the thermal mismatch strengthening (George et al., 2005)..... 89

Figure 52. A diagrammatic sketch of inclusions' distribution patterns. (a) The inclusions are assumed to be vertically aligned if all the inclusions' height direction is the same as the model displacement direction. (b) the inclusions are horizontally aligned if all the inclusions' height direction is perpendicular to the displacement direction. 90

Figure 53. The interface of the 3D RVE Toolbox plug-in for heat transfer analysis. Besides random generation for the inclusions, the inclusions can also be generated via certain patterns, like all inclusions are horizontally aligned vertically aligned with the help of this plug-in. 91

Figure 54 The comparison between FEA simulation results and input stress-strain data. It shows a perfect fit between these two sets of data which verifies the FEA model. 96

Figure 55 (a) shows a RVE model of 0.3 wt. CNT reinforced epoxy composites with interface considered and different color in the model represents different material; (b) the contour plot of maximum principal logarithmic strains corresponding to RVE model shown in the left, the model is loaded along z axis. 97

Figure 56. The different stress-strain curves under different types of CNTs and interfaces. The result shows that the CNTs can strengthen the aluminum matrix, and different configuration has a different strengthening effect. The RVE model with isotropic CNTs and interface gives the best mechanical strengthening among the four configurations. 100

Figure 57 (a): the contour plot of accumulated equivalent plastic strain (PEEQ) of the 3D RVE model for the anisotropic CNT reinforced aluminum composites at 2.96% equivalent strain under uniaxial tension along the z-axis; (b): the cut view of the 3D model from y plane view which shows the local plastic strain of matrix and interface; (c): presents the contour plot of von Mises stresses of the corresponding cut view. 101

Figure 58: Finite element meshes of composites (left) and inclusions (right). 105

Figure 59: (a). A 2D parallel model of composites consisting of matrix and inclusions. (b). FE simulation results of temperature distribution. 106

Figure 60: Comparison of theoretical solutions and numerical predictions for the parallel models and series models. An excellent correlation is achieved. 107

Figure 61: Influence of pore size on the effective thermal conductivity of porous materials. Keeping the same volume fraction of pores, the radius of pores has a negligible effect on effective thermal conductivity. 108

Figure 62: Influence of pore orientation on the thermal conductivity of porous materials 109

Figure 63: Influence of aspect ratios on the thermal conductivity of porous materials with pores vertically aligned. 110

Figure 64: Influence of aspect ratios on the thermal conductivity of porous materials with pores horizontally aligned. 110

Figure 65: Composites with spherical inclusions. (a) whole composite RVE model. (b) Inclusions only. 111

Figure 66: Influence of inclusion size on the effective thermal conductivity of composites is negligible. The volume fraction of inclusions has a significant effect instead. 112

Figure 67: An RVE model of the matrix (left) and inclusions (right). The contour plot shows the temperature distribution in the FE simulation. 113

Figure 68: Influence of inclusion orientations on the effective thermal conductivity of composites. 113

Figure 69: Influence of inclusion aspect ratios on the effective thermal conductivity of composites while inclusions are vertically aligned 114

Figure 70: Influence of inclusion aspect ratios on the effective thermal conductivity of composites while inclusions are horizontally aligned 115

Figure 71: Influence of interfacial thermal resistance on the effective thermal conductivity of composites while inclusions are all vertically aligned. Two different trends are observed based on interfacial thermal resistance: The effective thermal conductivity (ETC) decreases with the increase of volume fraction of inclusions if interfacial thermal resistance is small; vice versa. 116

Figure 72: (a). A 3D RVE model where the inclusions have anisotropic thermal conductivity property; (b). the contour plot of the magnitude of the heat flux vector for the corresponding RVE model 117

Figure 73: Influence of thermal conductivity anisotropy on the effective thermal conductivity of composites. The matrix material is aluminum with a thermal conductivity of 250 $Wm^{-1}K^{-1}$, ... 118

Figure 74. Geometrical representation of a general stress state in the principal-stress-space. Ref. (Bai & Wierzbicki, 2008) 126

Figure 75. Tensile true stress-strain curves of the CNT reinforced copper composites with different volume fractions (0, 0.5 vol.%, and 1 vol.%)) of CNTs and under different testing temperatures (293K, 573K, and 773K) (Jiapeng Liu et al., 2019; Jiapeng Liu et al., 2018)..... 131

Figure 76. Temperature effects on the average yield stresses of different CNT reinforced copper composites..... 134

Figure 77. Comparison between experimental data and analytical solutions for CNT reinforced copper composites. A good correlation has been achieved for the strengthening effect. Note that ductility loss has not been considered here..... 135

Figure 78. A comparison between experimental fracture strains (uniaxial tension) and analytical model predicted strains. The experimental data are presented with round dots and the analytical results are shown in the colored surface. A very good correlation is achieved between the experiment and the analytical model. 136

Figure 79. A comparison between the experimental data and the analytical predictions. Both the strengthening effect and ductility loss are well predicted by the proposed analytical models. The material softening which is caused by elevated temperature is also well captured. 137

Figure 80. The multiaxial stress 3D fracture locus of Cu-0.5%vol. CNT composite under room temperature based on the calibrated ductility model. 138

Figure 81 (a). An SEM image of Ni-coated CNTs. (b). An example of the fracture surface of Al/NiCNTs nanocomposites showing no interface debonding during loading. Dimples show material ductile fracture mode. 139

Figure 82 Calibrated true stress-strain curves of both pure aluminum and Al/NiCNTs with different weight fractions of NiCNTs 140

Figure 83. Comparison of fracture strain (uniaxial tension) between experimental data and analytical predictions for Al/NiCNT composites. The weight fraction means weight fraction of Ni coated CNTs..... 142

Figure 84. 2D fracture loci under plane stress condition of pure Al and Al-0.5%wt. NiCNT composites based on the calibrated analytical ductility model. 143

LIST OF TABLE

Table 1. The measured dimensions of all specimens before and after tests stress and the corresponding fracture strain. 27

Table 2. Gauge lengths of different specimens. Torsion specimen is not analyzed by DIC software. 29

Table 3. Stress triaxialities and Lode angle parameters for different types of specimens. R is the radius of a notch, a is the radius of a notch for a round bar, and t is the thickness of the groove for a grooved plate (Bai & Wierzbicki, 2008). 31

Table 4. Calibrated material elastic-plastic properties for the finite element simulations..... 37

Table 5. Calibrated material plasticity parameters for PPL model 37

Table 6. Calibrated material fracture parameters for the MMC model 37

Table 7. The comparison among experimental fracture strains, MMC fracture criterion, and finite element simulations. The simulation data are extracted from the specimen necking edge point. Based on averages of the stress triaxiality history and Lode angle parameter history, the MMC fracture strains are calculated and compared with experimental data. 49

Table 8. Calibrated material plasticity parameters for PPL model with piecewise function of hydrostatic pressure effect 53

Table 9. Calibrated material fracture parameters for the MMC model with piecewise function of hydrostatic pressure effect 53

Table 10 Ni Plating Bath Composition 58

Table 11 Mechanical properties of pure aluminum matrix used in FE simulations 62

Table 12. Mechanical properties of CNTs and nickel used in FE simulations, Data adapted from Refs. (Ayer et al., 2014; CheapTubes; Long et al., 2015) 65

Table 13 Some key parameters used in RVE models 68

Table 14 The optimized best combinations of model parameters that well fit experimental data with different weight fractions of NiCNTs 72

Table 15. 3D model boundary condition information 95

Table 16: The elastic modulus of composites represented by RVE with different types of CNT and interfaces. Isotropic CNT has the same elastic modulus (1 TPa) along different directions, while the elastic modulus of anisotropic CNT is different along different directions: 1 TPa along the axial direction and 30 GPa along radial and circumferential directions. The volume fraction of the interface is 6% when the interface is considered. 97

Table 17 Mechanical properties of pure aluminum used in finite element simulations. 98

Table 18. Lode angle parameter and stress triaxiality for typical loading conditions (Bai & Wierzbicki, 2008). 127

Table 19. Material parameters of CNT and copper, and the fabrication process parameters (Bai & Wierzbicki, 2008; Jiapeng Liu et al., 2019; Jiapeng Liu et al., 2018; Schelling & Keblinski, 2003; Shirasu et al., 2015) 132

Table 20. The average yield stresses of copper matrix composites with different volume fractions of CNT and under different temperatures before and after normalization 133

Table 21. Calibrated parameter values for the strengthening analytical model and ductility loss analytical model of Cu/CNT composites. 137

Table 22 Composition of Ni Plating Bath..... 140

Table 23. Material parameters of CNT and aluminum for the current case study, and the fabrication process parameters 141

Table 24. Calibrated parameters for the ductility analytical model of Al/NiCNT composites .. 142

CHAPTER 1 INTRODUCTION

1.1 Background

Upon introduction by Iijima (Iijima, 1991) in 1991, carbon nanotubes (CNTs) have drawn much attention because of their high stiffness and exceptional thermal and electrical conductivities (Berber, Kwon, & Tománek, 2000; Ebbesen et al., 1996; Hone, Whitney, Piskoti, & Zettl, 1999; Treacy, Ebbesen, & Gibson, 1996), and these extraordinary properties of CNTs make many new technologies and applications possible. Lightweight metal matrix composites (MMCs) also possess very attractive mechanical properties and meet the demand of lightweight design in various industries such as aerospace and automobile industries (An et al., 2011; He, Liu, & An, 2017; Jia & Bai, 2016; Jinling Liu, Zhao, Zhang, Wang, & An, 2015). So the metal matrix composites reinforced by CNTs (Metal/CNT) is a fast-emerging research area. Aluminum carbon nanotube (Al/CNT) composites have been used to produce microelectromechanical systems (MEMS) because Al/CNT composites can provide a large elastic modulus which is necessary for high frequency resonators in MEMS (Bakshi, Lahiri, & Agarwal, 2013). Composites reinforced by CNTs can also be used on light-weight bicycles, tennis rackets (sports industry), brake shoes, cylinder liners (automobile industry), and so on (Bakshi et al., 2013).

Electrical wiring is another example of the application of CNTs. Electrical wiring is defined as the electrical installation of cables and related devices like distribution boards, light fitting, and switches (contributors, 2019). There are very high standards of electrical wire like safety and energy consumption, since the electrical wire is used by everyone, every day. Copper and aluminum are widely used in electrical wire and industrial machinery due to the high electrical conductivity, high thermal conductivity, low thermal expansion, and relatively high strength

(Emsley, 2011). Though there are competitions from other materials, they are always the preferred electrical conductors in a lot of categories of electrical wire like power generation, power distribution, electronics, and power transmission. However, power loss is inevitable due to the existence of electrical resistance, and this happens wherever electricity is used (for example, transmission lines and electronics). According to the International Electrotechnical Commission (Commission, 2007), the Joule effect in transmission cables accounts for losses of 2.5%, and the losses in transformers range between 1% and 2%. This means that saving just 1% on the electrical energy produced by a power plant of 1000 megawatts means transmitting 10 MW more to consumers and this can supply 1000 – 2000 more homes. It is promising if more electrically conductive materials are fabricated and used for electrical wire, as this would save a lot of electrical power. CNT reinforced metal matrix composites have the potential to achieve this goal considering the exceptional thermal conductivity and electrical conductivity of CNTs. CNT reinforced composites are also a great candidate as efficient cooling material for electronics like supercomputers.

1.2 Motivation and Objectives

In the past decade, the excellent properties of CNTs are reported in different kinds of literature. It is always important to know how a small number of CNTs change the properties of composites. The current work is to investigate the strengthening mechanisms and ductility of CNT reinforced metal matrix composites. Experiments, analytical methods, and finite element simulations are all employed in this thesis. The overview of this work is summarized as follows:

- Investigate the strengthening effect of CNT reinforced aluminum composites by the analytical method and finite element analysis (2D representative volume element (RVE) method).
- Develop a digital workflow to study the strengthening effect of CNT reinforced composites with 3D representative volume element (RVE).
- Study the influence of inclusions on the thermal conductivity of metallic matrix composites based on the developed digital workflow above.
- Develop an analytical solution for the strength-ductility trade-off phenomenon of CNT reinforced composites considering the influence loading conditions and elevated temperatures.

1.3 Outline of the thesis

The present dissertation consists of eight chapters. Chapter 1 presents a brief introduction to the background, motivations, and objectives of this dissertation. Chapter 2 gives the literature reviews on the mechanical properties and thermal conductivity of CNT reinforced composites which includes experimental method, numerical method, and analytical models.

In Chapter 3, a set of mechanical experiments for pure copper are conducted under different loading conditions, including uniaxial tension, uniaxial compression, notch tensions with different notch sizes, and torsion. Based on the mechanical testing data, finite element analysis is carried out for all the testing cases and a good fit is achieved between the experiments and finite element simulations. To capture the mechanical behaviors of pure copper, the plasticity with pressure and Lode angle effects (PPL) plasticity model and modified Mohr-Coulomb (MMC) fracture model are implemented during the finite element analysis. The experimental data and finite element

simulation results provide a baseline of the copper matrix's mechanical properties for future studies of copper-based composites.

Chapter 4 develops the finite element models in Abaqus to simulate the strengthening and deformation behaviors of nickel-coated carbon nanotube reinforced aluminum-based composites with different weight fractions of CNTs. Representative volume element (RVE) is employed to save the computational power and is implemented in 2D axisymmetric FE model which is consisted of four parts: metal matrix, CNT, nickel, and the hardened zone between metal matrix and nickel-coated CNTs which is mainly caused by thermal expansion effect and Orowan looping effect. A parametric study is carried out to investigate the influence of different influencing factors. The simulation results are correlated well with the experimental data reported by Dr. Chen's group and show that the aspect ratio of CNTs and the Orowan effect play important roles in the strengthening effect of CNT reinforced composites. Moreover, an analytical solution is derived, and a good fit is achieved to the experiment data. This work is published in the journal of Composite Interfaces (Song et al., 2020).

In Chapter 5, in order to have a better understanding of the influences like CNT aspect ratio, volume fraction, distribution in the 3D space, hardened zone volume fraction, and residual plastic strain the hardened zone, a digital workflow is proposed to investigate the mechanical and thermal properties of composites, and the 3D RVE method is implemented for the analysis. Based on Abaqus and Python, a graphical user interface (GUI) is then developed as an Abaqus plug-in for the automatic generation of the 3D RVE model. Random sequential adsorption (RSA) algorithm is employed to generate inclusions in order to avoid interference among inclusions. This GUI is capable of model creation, material property assignment, boundary condition assignment, solving, and corresponding postprocessing for both mechanical analysis and thermal conduction analysis.

This plug-in can be used to investigate the strengthening effects of composites like carbon nanotube reinforced nanocomposites and chopped carbon fiber-reinforced composites where the inclusions are randomly distributed in 3D space. Reinforcing materials like carbon nanotube and carbon fiber are generally anisotropic. For the first time, the anisotropic material properties (i.e., transversely isotropy or orthotropy) of inclusions are considered and modeled in this work for composites with 3D randomly distributed inclusions. Moreover, the interface between the matrix and inclusions is considered, and its influence is investigated, which would provide more accurate results for the study of strengthening mechanisms of composites. Two case studies of carbon nanotube reinforced composites were performed and proved the accuracy of this tool. Compared with modeling by hand, the automatic generation of RVE models greatly reduces the possibility of handling errors and improves reliability. This work is submitted for publication.

In Chapter 6, based on the developed Abaqus plug-in in Chapter 5, the influence study of inclusions' shapes, distributions, and anisotropy on the effective thermal conductivity of composites is then carried out. Both spherical and cylindrical inclusions are generated to study the effect of inclusion shape. Simulation results are correlated with analytical solutions for the modeling methodology. The results show that the orientations of inclusions can greatly influence the effective thermal conductivity of composites, and the effective thermal conductivity is the largest when the principal axis of cylindrical inclusions is aligned with the heat flow direction. The effective thermal conductivity of composites gets worse as the interfacial thermal resistance gets higher than the matrix. At last, this study, as the first one using the 3D RVE method, shows that the anisotropy of inclusions has an important effect on the effective thermal conductivity of composites. This developed 3D RVE model provides useful guidance on material design and property evaluation for porous materials and composites. This work is submitted for publication.

Carbon nanotubes can greatly enhance the strength of metal matrix composites while resulting in ductility loss. This strength-ductility trade-off dilemma always confines the development of material design and real-life applications. In Chapter 7, a temperature-dependent strengthening analytical model is proposed for CNT reinforced metal matrix composites which considers three common strengthening mechanisms: Orowan looping effect, thermal expansion mismatch effect, and load bearing effect. The proposed model can predict composite material strength with different volume fractions of CNTs and under different temperatures. Combining the strengthening model with the stress based modified Mohr-Coulomb (sMMC) ductile fracture model, a ductility analytical model is then derived. This ductility analytical model includes the influences of temperature, multi-axial stress loading conditions, as well as the aforementioned three strengthening mechanisms. A good agreement has been achieved between literature published experimental data and analytical predictions for both composite material strength and ductility loss. The proposed two analytical models can provide a straightforward way to study the strength-ductility relationship for CNT reinforced metal matrix composites over a wide range of temperatures and different stress states, and provide guidance on new material design and processing. This work is submitted for publication.

Chapter 8 provides a summary of the main contributions of the current dissertation and recommends some interesting and important topics for future study.

CHAPTER 2 LITERATURE REVIEW

2.1 Mechanical Properties of CNT composites

Inclusions like carbon nanotubes (CNTs) and graphene nanoplatelets can improve the strength of matrix materials, and CNT is viewed as one of the ideal reinforcements for metal matrix composites due to the excellent physical properties (high specific strength, low density, high thermal conductivity, and high electrical conductivity) of CNTs (Bakshi et al., 2013; Billah & Chen, 2017; Chai, Sun, & Chen, 2008; Daviran, Mohasseb, Kasaeian, & Mahian, 2017; A. M. K. Esawi, Morsi, Sayed, Taher, & Lanka, 2010; Jiapeng Liu et al., 2019). For example, Cha et al. improved the yield strength of aluminum by 300% with a 10% volume fraction of CNTs (Cha, Kim, Arshad, Mo, & Hong, 2005). Qian et al. showed that Young's modulus of polystyrene is improved from 1.2 GPa to 1.62 GPa with the addition of 1wt% of CNTs (Qian, Dickey, Andrews, & Rantell, 2000). Currently, CNTs reinforced composites have been used in different applications, like transistors, bikes, ships, and spacecraft (Cao, Andrews, Kumar, & Franklin, 2016; De Volder, Tawfick, Baughman, & Hart, 2013). A collection of strengthening effects for different shapes of reinforcements, including SiC particles, CNT, and Graphene, are illustrated in Figure 1. One can see that the cylindrical shape of CNT plays a vital role in enhancing composites' mechanical properties.

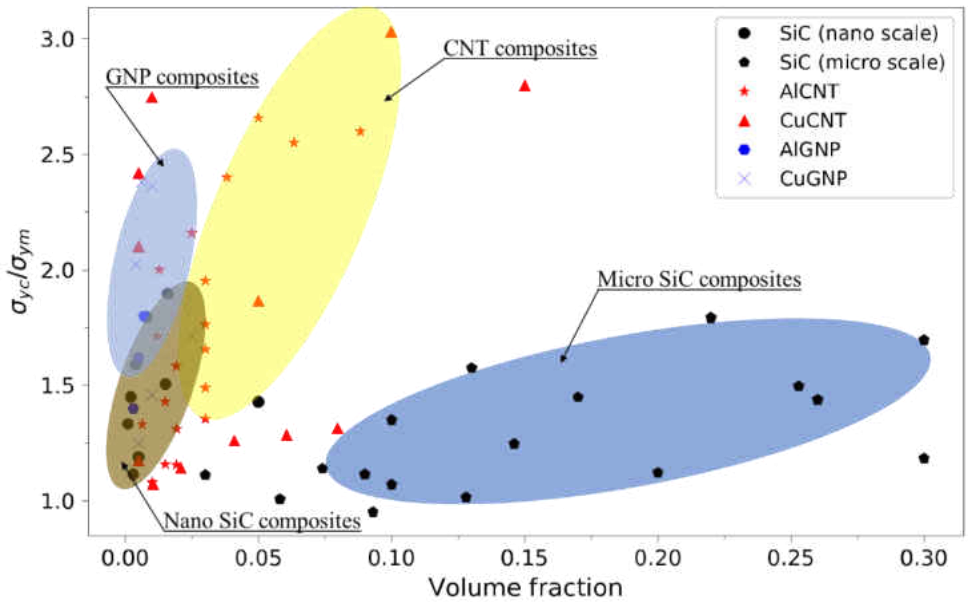

Figure 1. Comparison of strengthening effects among metal matrix composites with different strengthening inclusions. It presents that CNT reinforced composites have a great strengthening effect. Ref: (Chai et al., 2008; B Chen, Kondoh, Li, & Qian, 2020; F. Chen et al., 2016; HJ Choi, Shin, & Bae, 2011; Hyunjoo Choi, Shin, Min, Park, & Bae, 2009; Cöcen & Önel, 2002; Fan et al., 2018; Ferkel & Mordike, 2001; Fu, Chen, & Liu, 2020; Hwang et al., 2013; P. Li, Chen, & Qin, 2017; Jiapeng Liu et al., 2018; Nie, Deng, Wang, & Wu, 2017; Reddy et al., 2017; Saravanan & Surappa, 2000; Shin, Choi, Shin, & Bae, 2015; H. Wang et al., 2018; Xu et al., 2017; D. Zhang & Zhan, 2016; H. Zhang et al., 2017; C. Zhao & Wang, 2014)

However, the ductility of composites would deteriorate due to the addition of CNT if the fabrication or/and processing methods are not improved. Figure 2 presents the fracture strain and yield stress relationship for different nano composite materials, and it shows that, for the same matrix material, the ductility decreases as the increase of composite material yield strength.

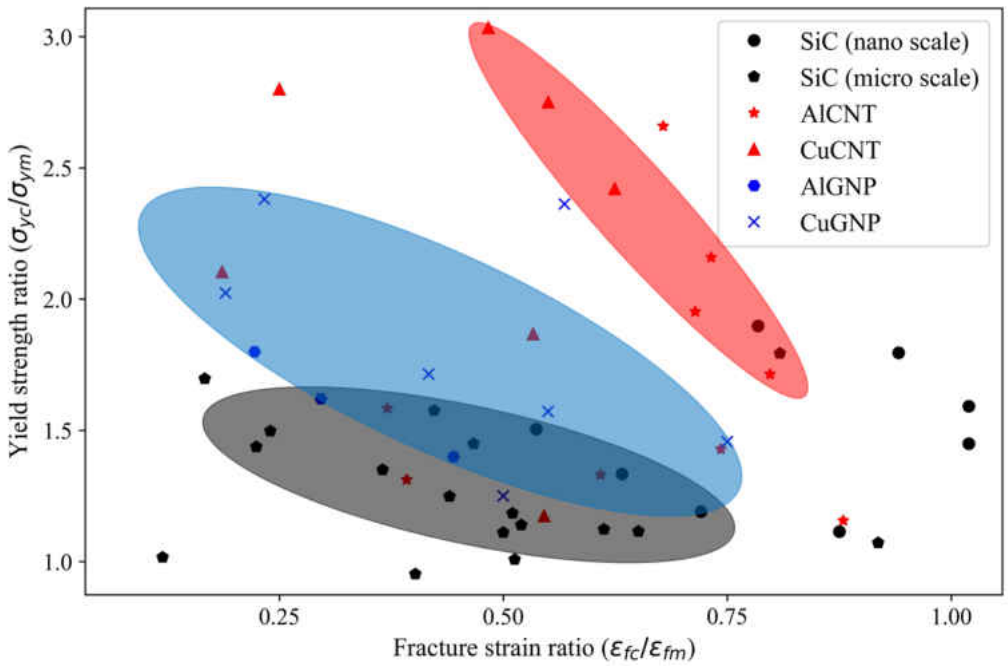

Figure 2. A comparison of yield stress and fracture strain for different composites (CNT reinforced composites, graphene reinforced composites, and SiC reinforced composites). The yield strength ratio is defined as the yield stress of composites versus that of the corresponding matrix, and the fracture strain ratio is defined as the fracture strain of composites versus that of the corresponding matrix. The results show that nano composite materials are usually strengthened by the compromise of ductility loss. Data took from Ref: (Chai et al., 2008; B Chen et al., 2020; F. Chen et al., 2016; HJ Choi et al., 2011; Hyunjoo Choi et al., 2009; Cöcen & Önel, 2002; Fan et al., 2018; Ferkel & Mordike, 2001; Fu et al., 2020; He et al., 2020; Hwang et al., 2013; P. Li et al., 2017; Jiapeng Liu et al., 2018; Nie et al., 2017; Reddy et al., 2017; Saravanan & Surappa, 2000; Shin et al., 2015; H. Wang et al., 2018; Xu et al., 2017; D. Zhang & Zhan, 2016; H. Zhang et al., 2017; C. Zhao & Wang, 2014)

In real-life applications, light-weight design becomes a hot topic and thus the strength and ductility of composites play an increasingly important role. Furthermore, CNT reinforced metal matrix composites are ideal materials in the automotive industry, aerospace industry, and electronics industry for different applications like load-bearing members and tribological coatings to functional applications (Bakshi et al., 2013). Under such circumstances, the composites will encounter a high temperature environment which will also affect their mechanical properties. The temperature-dependent material strength and ductility would play important roles in the functions and reliability of CNT reinforced metal matrix composites under elevated temperatures. Moreover, it has been proven that the effect of multiaxial stress loading conditions is very important on the fracture of metallic materials (Bai & Atkins, 2012; Dunand & Mohr, 2011; Y. Li & Wierzbicki,

2010) and it is necessary to consider the influence of different stress states on the fracture of CNT reinforced metal matrix composites (He et al., 2020).

The mechanical properties of Metal/CNT composites are key factors for many of their applications, and there are several different methods for investigating the mechanical properties of Metal/CNTs. Experimental testing, numerical method, and theoretical models all have been implemented to study the elasticity, plasticity, and fracture properties in open literature (Bakshi et al., 2013; Coleman, Khan, Blau, & Gun'ko, 2006). Some studies were focused on the elastic properties of Metal/CNT composites under different loading conditions (Laborde-Lahoz et al., 2005; Seidel & Lagoudas, 2006; Zalamea, Kim, & Pipes, 2007), and some work were more focused on the plasticity and fracture of the composites (Barai & Weng, 2011; Dong, Zhou, Hui, Wang, & Zhang, 2015; Duan, Wang, Liew, & He, 2007; L. Jiang, Li, Fan, Cao, & Zhang, 2012; Long, Bai, Algarni, Choi, & Chen, 2015; Nakayama, 2007; Yengejeh, Kazemi, & Öchsner, 2017).

Mechanical testing is one of the traditional and reliable ways to characterize the strength and ductility properties of materials and it is widely used in both academia and industry. The material strength of CNT reinforced metal matrix composites has been widely reported by the experimental method, and excellent properties of CNTs are reported in different reports. Cha et al. (Cha et al., 2005) fabricated Al/CNT composites with 10% volume fraction of CNTs, and increased the yield strength by 300%. Esawi et al. (A. M. K. Esawi et al., 2010) employed a ball milling technique to disperse 2% weight fraction of CNTs into the aluminum matrix, and fabricated tensile testing samples based on these Al/CNT composites. They found that the tensile strength of aluminum was increased by 50% with the dispersion of CNTs. Wang et al. (H. Wang et al., 2018) reported a new method of fabricating Cu/CNTs by sintering and realigning quasi-1D CNTs into the 3D metal matrix. The yield strength was improved by 29%, while the ductility was only decreased by 19.4%.

Chen et al. (Q. Chen, Chai, & Li, 2005) demonstrated that the material strength of the copper matrix can be improved by 300% with a 4% volume fraction of CNTs. Chen et al. (Biao Chen et al., 2015) investigated the load transfer strengthening effect of CNT reinforced aluminum matrix composites. They confirmed the contribution of the load transfer effect by conducting the in-suit tensile tests. Liu et al. (Jiapeng Liu et al., 2019) fabricated CNT reinforced copper matrix composites and conducted high temperature tensile testing for both pure copper and CNT copper composites. The results reveal that CNTs can enhance the copper matrix, but the elevated temperatures would make the composites softening. Mokdad et al. (Mokdad et al., 2016) explored the deformation and strengthening mechanism of CNT reinforced aluminum matrix composites under different temperatures. The downside of mechanical testing is that the cost of mechanical testing is relatively high, and the whole process is time-consuming. Besides, there is a high requirement for fabrication facilities and testing facilities. Sometimes, it is very hard or even impossible to do thorough testing when the influence of loading conditions (or stress states) is considered.

Numerical method is another very common tool for the mechanical property study of materials. Through numerical simulations with a limited amount of mechanical testing for verification and calibration, for example, molecular dynamics and finite element analysis, one can predict the strength and ductility of materials with good accuracy and provide an easier and more efficient way to investigate material properties where the traditional sole mechanical testing cannot or hardly work (Imani Yengejeh, Kazemi, & Öchsner, 2017; Shokrieh & Rafiee, 2010). Liew et al. (Liew, He, & Wong, 2004) studied the elastic and plastic properties of multi-walled carbon nanotubes (MWCNTs) by the molecular dynamics method. This method can predict the mechanical properties well for nano-composites at the micro-scale level, currently, it is not

practicable to predict material properties at a macro-scale level due to the limitation of computing capacities for the time being (Long et al., 2015). Llorca et al. (Llorca, Needleman, & Suresh, 1991) employed a numerical method to study the deformation and fracture of metal-matrix composites, and it is proved that the numerical method was an effective way to study the nano-composite properties at the macro-scale level. Namilae et al. investigated the effect of the interface of CNT reinforced composites on the composite strength by both molecular dynamics and finite element analysis (Namilae & Chandra, 2005). Mayandi et al. (Mayandi & Jeyaraj, 2015) studied the vibration, bending, and buckling properties of functionally graded carbon nanotube reinforced composite beam by finite element method. They conclude that the bending deformation moderates with the increase of volume fraction of CNTs. Compared to mechanical testing, the cost of the numerical method is lower, and the process is less time-consuming. However, numerical simulations have high requirements for computational skills and computational capacities.

Due to the nature of complexity, sometimes numerical calculation of composites can also be very time-consuming. Finite element analysis on a representative volume element (RVE) is very common in the composite investigation. RVE is defined as the smallest element that can represent the material properties of the whole. This tool has been proven to have the function to investigate both mechanical properties and thermal properties of composites (Bargmann et al., 2018; Fang, Qi, & Tu, 1996; Y. Liu & Chen, 2003). Sharma et al. (Sharma, Misra, & Sharma, 2017) studied the effect of thermal residual stress on the thermal-mechanical deformation process for $\mathrm{Al}/\mathrm{B}_4C$ composites with RVE method, and spherical inclusions are used for the analysis. Sun et al. (Sun & Vaidya, 1996) predicted elastic constants by FEA with the RVE method. The results agreed well with analytical solutions and experimental results. Long et al. (Long et al., 2015) investigated the mechanical strengthening mechanism of carbon nanotube reinforced copper

composites by the 2D RVE method, and the results showed that the aspect ratio of CNTs (CNT height versus diameter) and the hardened zone at the interface between the Cu matrix and CNTs plays an important role on the mechanical strengthening of composites.

For most real applications, the inclusions show a random distribution characteristic inside the matrix during the manufacturing process. When the RVE models for composites are generated, the most-used inclusion distribution pattern is the ideal distribution which means that the inclusions are equally distributed inside the matrix, like square inclusion packing and hexagonal inclusion packing, and a lot of work has been done in this area (Bargmann et al., 2018). A more realistic result could be predicted if the random distribution property is considered for the inclusions. Bohm et al. (Böhm, Eckschlager, & Han, 2002) explored the elasticity and plasticity of metal matrix composites which are reinforced by randomly oriented short fibers using the finite element method. Bohm et al. presented that the inclusion shapes have a big influence on the mechanical properties of composites. Bailakanavar et al. (Bailakanavar, Liu, Fish, & Zheng, 2012) employed a hierarchical random sequential algorithm to automatically generate RVE models with randomly generated inclusions, which include spheres and cylinders. They also showed the influence of the inclusions' aspect ratio on the elastic property of composites.

Abaqus is one of the very popular finite element software packages and is widely used by industries and academia (Systèmes, 2012). Abaqus has also been used in FEA-RVE analysis for a long time. Tchalla et al. (Tchalla, Belouettar, Makradi, & Zahrouni, 2013) developed an Abaqus toolbox which is capable of building multi-level finite element models for fiber-reinforced composites and running simulations for mechanical problems. This toolbox greatly simplifies the FEA modeling process and saves solving time. Omairey et al. (Omairey, Dunning, & Sriramula, 2018) created an Abaqus toolbox called EasyPBC which is used to automatically set up the RVE homogenization

technique. This plug-in can perform all steps from 3D modeling, setting boundary conditions, applying loads, meshing to solving once all the model parameters are given. Riano et al. (Riaño & Joliff, 2019) presented an Abaqus plug-in to generate representative volume elements with randomly distributed long fibers. This toolbox is mainly used for the study of unidirectional composite micromodels. Moreover, the influence of interface is also taken into consideration in this plug-in, and a case study is carried out which shows the importance of the interface. However, to the best of the authors' knowledge, no study has been found on the influence of interface and anisotropic properties of inclusions for the 3D RVE study of composites where the inclusions are randomly distributed in three dimensions. For instance, carbon nanotubes, chopped short fibers, and graphene have strong anisotropy since they are low dimensional materials (Ni et al., 2010; Salvetat et al., 1999), but currently, they are mainly modeled as isotropic material in RVE studies.

On the contrary, analytical solutions have their unique advantages. Analytical models can also provide guidance on material development and product design and can greatly reduce research cycles. In 1969, Amirbayat et al. (Amirbayat & Hearle, 1969) derived the matrix-fiber load transfer expression for unit composites. This model applies the basic elasticity theory and works for any type of matrix-fiber bond in the composites. They investigated the effect of different variables on the system for the case of no perfect bond in which slippage is inhibited by frictions. After that, several models have been derived for the elasticity study of the general fiber reinforced composites (Fukuda & Kawata, 1974; Hsueh, 2000; Tandon & Weng, 1984; Weng, 1984). The Shear-lag model is a popular method to investigate the elastic properties of CNT reinforced composites from the perspective of continuum mechanics (Biao Chen et al., 2015; X. L. Gao & Li, 2005; Nairn, 2011; Tsai & Lu, 2009). Gao et al. (X. L. Gao & Li, 2005) proved that the capped nanotube is equivalent to an effective (solid) fiber having the same length and diameter, but Young's modulus

should be determined from that of the nanotube under the isostrain condition. They then showed that aspect ratio is a critical controlling parameter for the CNT reinforced composites. Nairn (Nairn, 2011) evaluated the influence of the aspect ratio of carbon nanotubes in the composites by the shear-lag model and compared it with classic fibers. Their study shows that the interface between matrix and inclusions is very important for the reinforcements. Moreover, other strengthening mechanisms are also developed as the development of science (Suh, Joshi, & Ramesh, 2009) (George, Kashyap, Rahul, & Yamdagni, 2005; Z. Liu, Xiao, Wang, & Ma, 2017; Long et al., 2015; X. Zhang et al., 2020). Among them, Suh et al. (Suh et al., 2009) pointed out that the size of reinforcements is very important for the reinforcing effect. The Orowan strengthening effect plays more effect on metallic matrix nanocomposites as the size of reinforcement decreases. Zhang et al. present an analytical model which can predict the temperature-dependent yield stress of CNT reinforced metal composites (X. Zhang et al., 2020).

However, the theoretical study on the ductility of CNT reinforced metal matrix composites has only few been carried out though the ductility of composites is of high importance for both the fabrication and application of composites. For example, extrusion is one of the widely adopted methods to fabricate densified CNT composites and can make the CNT more aligned in the matrix (Kwon, Estili, Takagi, Miyazaki, & Kawasaki, 2009; Kwon & Leparoux, 2012). But due to the addition of CNTs, the ductility of composites would decrease, and high temperature is necessary for the extrusion to ensure that the extruded composites have good quality like great interface bonding. Different volume fractions of CNT, loading conditions, and hot extrusion temperature all affect the ductility of composites (Bai & Wierzbicki, 2008, 2009; Kwon et al., 2009) and a theoretical method that can characterize different influencing factors on the ductility would provide valuable guidance on material design and product development.

2.2 Thermal Conductivity of CNT Composites

Precise prediction of thermal conductivity can help the design and application of various materials like porous materials and composites. For example, cellular metals have the advantages of both a metal which is strong and has excellent thermal conductivity, and the foam which is lightweight, thus cellular metals have been used in different fields, like structural panels, heat exchangers, etc. (Solórzano et al., 2008). Carbon nanotubes (CNTs) have excellent thermal conductivity (Berber et al., 2000; Iijima, 1991). It is of great interest to know how a small number of CNTs can improve the thermal conductivity of matrix materials like copper, aluminum, and most of the polymers. The CNT reinforced composites would have better thermal conductivity than that of the matrix (Han & Fina, 2011; Shi et al., 2007; So et al., 2018). Shi et al. (Shi et al., 2007) improved the thermal conductivity of monolithic W-Cu alloy by 27.8% after adding 0.4 wt.% multi-walled carbon nanotubes. The effective thermal conductivity of composites is influenced by many factors: inclusion size, volume fraction, shape, and orientation, the volume fraction of voids (or inclusions), and the interfacial thermal resistance between matrix and inclusions. Knowing how these parameters affect the thermal conductivity of composites would be helpful to the applications of composites. However, it is nearly impossible to run a quantitative analysis for certain parameters as it is very difficult to exclude the influence of other parameters through an experimental approach. Theoretical and numerical approaches would be a great way to help understand the influences of the parameters.

Different methods were proposed to predict thermal conductivity, including analytical solutions and numerical methods (Ondracek & Schulz, 1973) (Maxwell, 1881) (Q. Z. Xue, 2005) (Z. Wang, Kulkarni, Deshpande, Nakamura, & Herman, 2003). Different methods can provide unique advantages compared with other methods.

A set of constitutive equations of thermal conductivity were proposed by many researchers. Maxwell proposed an equation that can be used to predict the thermal conductivity of porous media with spherical inclusions, where the volume fraction of pores can be as high as 40%. Many analytical solutions were developed based on the Maxwell equation (Maxwell, 1881). Ondracek et al.(Ondracek & Schulz, 1973) stated that the effective thermal conductivity of materials depended on not only the void volume fraction, but also pores' shape, orientation, distribution, and relative size, and they presented an equation for a porous medium with isolated closed non-conducting inclusions. She et al. summarized five concise expressions for simple two-phase systems (She, Zhao, Cai, Jiang, & Cao, 2018). These concise expressions can provide solutions to simplified cases but cannot be applied to complex material structures. Xue (Q. Z. Xue, 2005) proposed a model to predict the thermal conductivity of CNT reinforced composites which also took aspect ratio of CNTs into consideration. Yang et al.(X. Yang, Lu, & Kim, 2013) provided the analytical equation that can predict the effective thermal conductivity of porous materials which was applicable to closed cell foams and honeycombs.

Finite element analysis (FEA) is a convenient and powerful tool to predict the thermal conductivity of materials as the fast development of computer computation capability, and a lot of work has been done based on this method. Compared with the trial-and-error process, FEA can tremendously improve product development speed and decrease costs. Wang et al.(Z. Wang et al., 2003) studied the influence of pores and interfaces on the effective thermal conductivity of plasma sprayed zirconia coatings. She et al. (She et al., 2018) employed a numerical method to mainly investigate the influence of pore shapes on the equivalent thermal conductivity of cellular concrete by two-dimensional models. Representative volume element (RVE) was deployed to represent the structure, and the model was verified by both analytical expressions and experiments from

literature. Finite element analysis can also be used to predict the equivalent thermal conductivity of composites. Jiang et al. (L.-l. Jiang, Xu, Cheng, Lu, & Zeng, 2014) studied the temperature distribution and thermal conductivity of 3D braided composites by a modified finite element method. Representative volume element was used to simplify the calculation.

In most of the above-stated literature, a simplified model which assumes a perfect interface contact between matrix and inclusions is taken. But in most of the cases, the influence of interface between matrix and inclusions cannot be neglected when the effective thermal conductivity of composites is of interest. Kapitza (Swartz & Pohl, 1989) found that there is temperature discontinuity at the metal-liquid interface, which, as we know now, is the interfacial resistance. Hasselman et al. (Hasselman & Johnson, 1987) firstly integrated interfacial thermal resistance into a theoretical method by Maxwell-Garnett-type effective medium approximation. Nan et al. (C.-W. Nan, Birringer, Clarke, & Gleiter, 1997; C. W. Nan, Shi, & Lin, 2003) took the concept of Kapitza's thermal contact resistance (Swartz & Pohl, 1989) and proposed a calculational procedure to predict the equivalent thermal conductivity of composites with an imperfect interface between matrix and inclusions. The analytical solution predicts higher thermal conductivity results than experiments. The authors believe that this might be caused by three reasons. First, there are aggregation and twist of the carbon nanotubes in the composites. Second, the poor bonding between matrix and carbon nanotubes. Third, there is still room for the improvement of the analytical expression.

Some materials, like diamond thin film (Graebner, Jin, Kammlott, Herb, & Gardinier, 1992), polyimide film (Park, Dillard, & Ward, 2000), and pyrolytic graphite (Hartmann, Voigt, Reichling, & Matthias, 1996), exhibit strong anisotropic thermal conductivity behavior: the thermal conductivity in one direction is higher than that in other directions. Such materials are great candidates to work as both heat spreaders (in one direction) and insulators (in other directions)

(Smalc et al., 2005) and can be used as thermal management materials (Ma, Guo, Zhang, & Chang, 2017; Pop, Varshney, & Roy, 2012). To the best of the authors' knowledge, no work has been done on the effect of anisotropic thermal conductivity of inclusions for the 3D RVE composite study where the inclusions are distributed in three dimensions. This study will be shown in this work.

CHAPTER 3 PLASTICITY AND DUCTILITY OF PURE COPPER

Copper has been widely used in different areas like electrical wires, electronics and, electric motors because of its great electrical conductivity, thermal conductivity, ductility, and mechanical strength. In recent years, since the development of science and technology has made it possible for more advanced devices, materials with better mechanical, electrical, and thermal properties are in demand (Kurzepa, Lekawa - Raus, Patmore, & Koziol, 2014).

Copper-based composites have drawn more and more attention around the world which are expected to fabricate more advanced composite materials (Kim, Lee, & Han, 2014; Subramaniam et al., 2013; H. Wang et al., 2018). Carbon nanotube reinforced copper composites is one type of materials that can provide better thermal conductivity, electrical conductivity, and mechanical strength (Subramaniam et al., 2013).

The mechanical properties of high purity copper have been investigated regarding the influence of strain rate (Johnson & Cook, 1985; Meyers, Andrade, & Chokshi, 1995; Mishra et al., 2008), temperature (Johnson & Cook, 1985; Lennon & Ramesh, 2004; Tanner, McGinty, & McDowell, 1999), and grain size (Meyers et al., 1995; Mishra et al., 2008; Tanner et al., 1999). One of the most famous works on the mechanical properties of oxygen-free high thermal conductivity (OFHC) copper was presented by Johnson and Cook when they introduced the Johnson-Cook plasticity model (Johnson, 1983). Johnson and Cook then brought the Johnson-Cook fracture model in 1985 by studying the mechanical properties of OFHC copper (Johnson & Cook, 1985). In these works, their focus was the influence of high strain rates, high temperature, and large strains on the plasticity of materials, but the influence of stress states is not covered. On the other hand, these two models are suited for computations because they both have simple forms, but the

accuracy of these two models are not very high with certain materials. The effect of strain rate has also drawn much attention since then. Rittel et al. (Rittel, Ravichandran, & Lee, 2002) study the constitutive behavior of OFHC copper under a wide range of strain rates by a newly-designed shear compression specimen. Bhattacharyya et al. also show that the increase of strain rate leads to the increase of strain hardening and this then leads to different deformation texture for OFHC copper (Bhattacharyya, Rittel, & Ravichandran, 2005).

J2 plasticity model has been widely used for metal and alloys for its simplicity, but the accuracy of this model may not be very high for some materials because it does not consider the effect of the third deviatoric stress invariant (which is associated with the Lode angle) and hydrostatic pressure on plastic yielding. Different works of literature have shown that the accuracy of plasticity models can also be increased for some materials when these two influencing factors are considered. Decades ago, Richmond et al. (Richmond & Spitzig, 1980; Spitzig & Richmond, 1984) first presented the influence of hydrostatic pressure on the plasticity of aluminum alloys. Starting in the year of 2004, Cazacu et al. (Cazacu & Barlat, 2004; Cazacu, Plunkett, & Barlat, 2006) developed new a model that considers the effect of the Lode angle parameter on the plastic yielding. But their model has the limitation on predicting plane strain yielding. Based on the experimental phenomenon, Bai et al. (Bai & Wierzbicki, 2008) proposed a new metal plasticity model that considers the effects of hydrostatic pressure and the third deviatoric stress invariant.

It has also been proven that both the stress triaxiality (Hancock & Brown, 1983; Hancock & Mackenzie, 1976; F. McClintock, 1968; F. A. McClintock, 1968; Rice & Tracey, 1969) and the Lode angle (Algarni, Bai, & Choi, 2015; Bai, 2007; Bai & Wierzbicki, 2008, 2009; T. S. Cao, J. M. Gachet, P. Montmitonnet, & P. O. Bouchard, 2014) play important roles in accurately predicting the fracture of ductile materials. McClintock (F. McClintock, 1968), Rice et al. (Rice &

Tracey, 1969), and Hancock et al. (Hancock & Mackenzie, 1976) presented that hydrostatic pressure has an influence on the ductile fracture property of materials. The John-Cook ductile fracture model (Johnson & Cook, 1985) was then proposed based on the previous study by Johnson and Cook. After that, the Lode angle has been proven to have an important role in predicting the ductility of metallic materials (Bai & Wierzbicki, 2008, 2009; T.-S. Cao, J.-M. Gachet, P. Montmitonnet, & P.-O. Bouchard, 2014; X. Gao, Zhang, Hayden, & Roe, 2009; Gruben, Hopperstad, & Børvik, 2012; Nahshon & Hutchinson, 2008; L. Xue, 2008). Bai et al. (Bai & Wierzbicki, 2008, 2009) proposed a new fracture model called the modified Mohr-Coulomb (MMC) fracture criterion based on the Mohr-Coulomb fracture model. This MMC criterion can predict both crack initiation and crack direction, and it contains good accuracy to predict tensile crack and shear fracture in multiaxial loading conditions. A series of literature has proven that this model is applicable to different materials (Bai & Atkins, 2012; Dunand & Mohr, 2011; Y. Li & Wierzbicki, 2010; Luo, Dunand, & Mohr, 2012). However, the influence of different stress states (stress triaxiality and lode angle) on the mechanical properties of OFHC copper has not been thoroughly studied.

It is now increasingly necessary to conduct such research because the copper matrix would experience various stress states inside composites when copper is reinforced by inclusions like carbon nanotubes or graphene (Bakshi et al., 2013; Berber et al., 2000; Cha et al., 2005; Imani Yengejeh et al., 2017; Jiapeng Liu et al., 2019; Jiapeng Liu et al., 2018). This work will focus on the plasticity and ductile fracture of OFHC copper by employing the uncoupled continuum mechanics based model of plasticity with pressure and Lode angle effects (PPL) and the modified Mohr-Coulomb (MMC) ductile fracture model. Mechanical tests that cover different stress states (different stress triaxialities and Lode angles) are designed and performed. The material models of

plasticity and fracture were implemented in commercial finite element software ABAQUS by using a user defined material subroutine (VUMAT). The results show that the plasticity and fracture of OFHC copper are highly related to stress triaxiality and the Lode angle. The proposed models can well predict the plastic behavior and ductile fracture of this material. The fracture propagation behavior is also well captured. A significant correlation between experiments and simulations is found.

3.1 Experiment Method

3.1.1 Specimen Design

OFHC copper is defined as a group of wrought copper alloys with high conductivity and the level of oxygen within it is less than 0.001%.

In this study, 6 types of specimens are designed which include smooth round bar, round bar with large external circular notch (large notch bar), round bar with small external circular notch (sharp notch bar), round bar for torsion (torsion bar, Figure 3), round cylindrical bar with small height (small compression bar) and round cylindrical bar with large height (large compression bar, Figure 4). Three dimensional (3D) sketches and the detailed dimensions are listed in Figure 3 for tensile and torsional specimens, and that for compression specimens are shown in Figure 4. Figure 5 presents the different types of manufactured samples. These samples are designed to test the plasticity and fracture of copper under different stress triaxialities and the Lode angles,

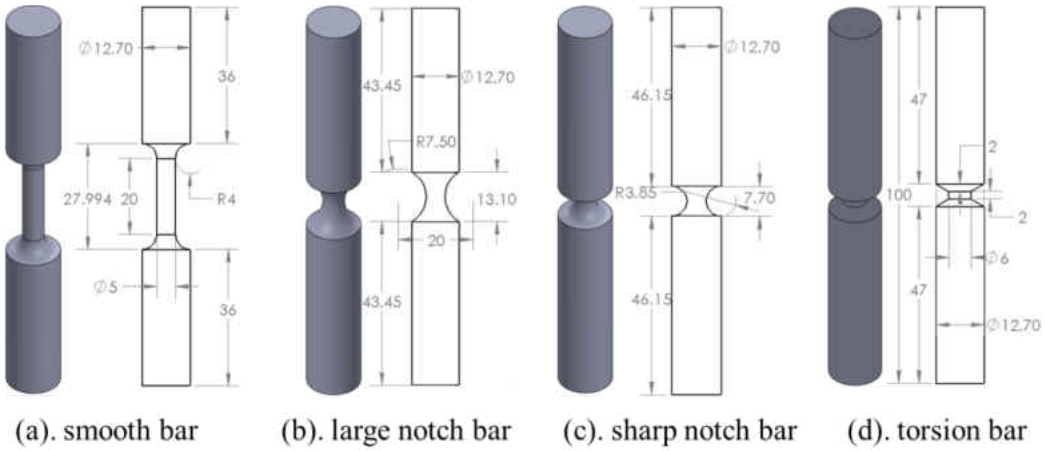

Figure 3. CAD drawings and dimensions of tensile and torsional specimens.

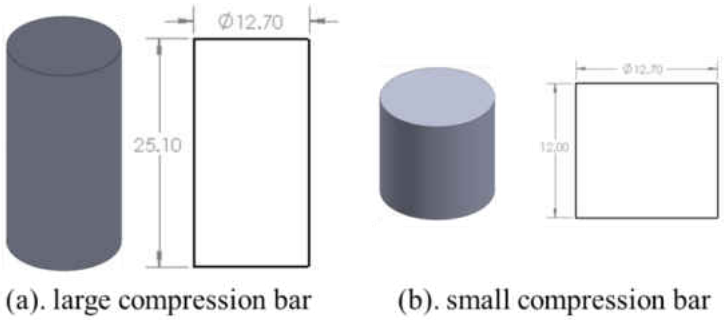

Figure 4. CAD drawings and dimensions of compression specimens

Figure 5. Machined samples of OFHC copper

The smooth bar specimens (Figure 3a) were under uniaxial tension loading condition and they were designed to bear uniaxial tension ($\eta = \frac{1}{3}, \bar{\theta} = 1$) for the critical point.

For the compression specimens, the theoretical value of stress triaxiality is $-\frac{1}{3}$. However, due to the existence of the friction between the specimen and compression pad, the stress triaxiality value would deviate from this theoretical value. So two different types of compression specimens are design. The torsion bars are designed to bear pure shear loading condition ($\eta = 0, \bar{\theta} = 0$).

The notched bar specimens are primarily used to check the influence of stress triaxialities on the plasticity and fracture of the materials. Bridgman (Bridgman, 1952) studied the stress distribution inside the notched bar specimens, which is shown in Figure 6, and proposed the formula to calculate the stress triaxiality, and the equation is shown in Eq. (1).

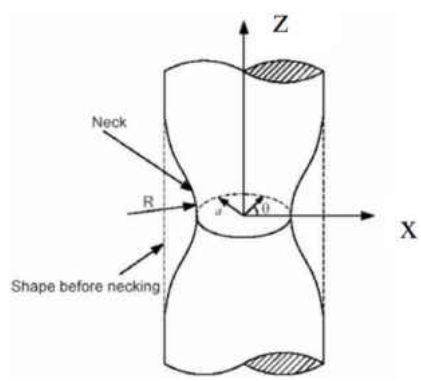

Figure 6. Round notched bars (Bai, 2007)

$$\eta = \frac{1}{3} + \ln\left(1 + \frac{a}{2R}\right) \tag{1}$$

where R is the local radius of the neck and a is the radius of the necking area.

In this work, two types of notched bar specimens (Figure 3b and Figure 3c) were designed so that they would cover a wide range of stress triaxiality ($\eta = 0.487$ and $\eta = 0.615$ respectively while $\bar{\theta} = 1$ for both the types)

The uniform equivalent strain to fracture in the necking area can be calculated by this equation.

$$\bar{\varepsilon}_f = 2\ln\left(\frac{a_0}{a_f}\right) \tag{2}$$

where a_0 is the cross-section radius for the round bar sample in the initial stage and a_f is the cross-section radius for the round bar sample at the fracture moment. The estimated initial stress triaxialities and Loge angle parameters of the specimens are summarized in Table 1. It should be noted that the stress triaxiality will change as the development of necking. Moreover, there is a little difference between the designed dimensions of the specimens and the measured dimensions of manufactured specimens due to machining accuracy and measurement accuracy. The dimensions listed below are all from the measurement.

Table 1. The measured dimensions of all specimens before and after tests stress and the corresponding fracture strain.

Specimen type	Radius of the neck (mm)	Initial diameter (mm)	Fracture diameter (mm)	Stress triaxiality ($\boldsymbol{\eta}$)	$\bar{\boldsymbol{\varepsilon}}_f$
Smooth bar	∞	5.04	2.2	0.333	1.658
Large notch bar	7.5	4.96	2.32	0.487	1.520
Sharp notch bar	7.7	5.05	2.59	0.615	1.335
Torsion bar	/	5.95	5.95	0	/
Large compression bar	/	12.7	/	-0.333	/
Small compression bar	/	12.7	/	-0.333	/

3.1.2 Experiments

All the samples with different geometries were fabricated from the same piece of copper rod. The tests were performed at room temperature and a quasi-static loading condition is used for all the tests.

The MTS Bionix EM torsion test system, which is shown in Figure 7, is used for the torsion experiment. Other types of specimens are tested with MTS servo-hydraulic test system with a 110kN load cell capacity. All the experiments are carried out with displacement control. The loading rate of the torsion test is 1 deg/s, and the loading rate of all the tension tests and compression tests are 0.01 mm/s. Image acquisition software (Vic-Snap Image Acquisition, Correlated Solutions, Inc.) was employed to capture images during the experiments where the samples are all painted in white then speckle patterned in black for image correlation purpose. Digital image correlation (DIC) equipment was used (Vic-2D Version 2009, Correlated Solutions, Inc.) to track and measure deformation history alongside mechanical testing for tension tests and compression tests. The data acquisition frequency was set to 1 Hz for both the force data and

displacement data for all the tests. For each sample, the displacement data was extracted from the recorded images by DIC software where a virtual extensometer was set up in the center of each specimen. The extensometer length of the smooth bar is 20 mm, and the other extensometer lengths are 7.6 mm, 13.1 mm, 8.47 mm, and 21.93 mm for sharp notch bar, large notch bar, small compression bar, and large compression bar, respectively. Table 2 presents the summary of gauge lengths for different specimens when the tested samples are processed by DIC software. The force-displacement curves are collected and plotted in Figure 8. It should be noted that due to the nature of the torsion test, the torsion samples keep rotating and DIC equipment does not apply to this type of test. So the displacement (rotational) data of torsion tests is from the MTS machine.

Figure 7. MTS Bionix EM torsion test system setup for torsion test.

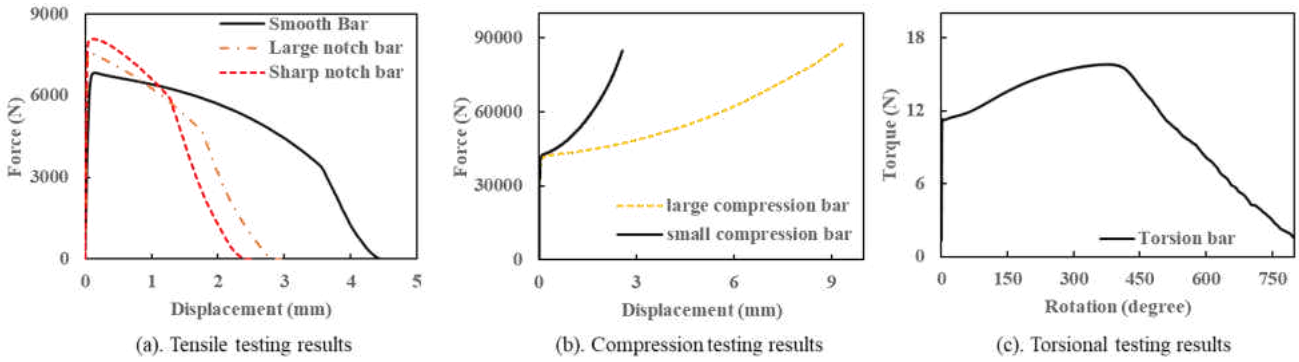

Figure 8. The force-displacement curves for different specimens. (a). shows the results for all the tensile specimens; (b). shows the results for both compression specimens; (c). shows the result of the torsional specimen test.

Table 2. Gauge lengths of different specimens. Torsion specimen is not analyzed by DIC software.

Specimen type	Smooth bar	Large notch bar	Sharp notch bar	Large compression bar	Small compression bar
Gauge length	20 mm	13.1 mm	7.7 mm	21.93 mm	8.47 mm

3.2 Plasticity Model and Fracture Criterion

The primary purpose of this work is to investigate the plasticity and fracture behaviors' dependencies on stress triaxiality and the Lode angle for OFHC copper. If the material is assumed to be isotropic, the three stress invariants can be defined as

$$p = -\sigma_m = -\frac{1}{3}(\sigma_1 + \sigma_2 + \sigma_3) \tag{3}$$

$$q = \bar{\sigma} = \sqrt{\frac{3}{2}[\boldsymbol{S}]:[\boldsymbol{S}]} = \sqrt{\frac{1}{2}[(\sigma_1 - \sigma_2)^2 + (\sigma_2 - \sigma_3)^2 + (\sigma_3 - \sigma_1)^2]} \tag{4}$$

$$r = \left[\frac{27}{2}\det([\boldsymbol{S}])\right]^{\frac{1}{3}} = \left[\frac{27}{2}(\sigma_1 - \sigma_m)(\sigma_2 - \sigma_m)(\sigma_3 - \sigma_m)\right]^{\frac{1}{3}} \tag{5}$$

where $[\boldsymbol{S}]$ is deviatoric stress tensor and $[\boldsymbol{S}] = [\boldsymbol{\sigma}] + p[\boldsymbol{I}]$. $[\boldsymbol{I}]$ is the identity tensor. σ_1, σ_2, σ_3 are the three principal stresses, and $\sigma_1 \geq \sigma_2 \geq \sigma_3$. Stress triaxiality is a dimensionless term that is related to hydrostatic pressure and defined in Eq. (6).

$$\eta = \frac{-p}{q} = \frac{\sigma_1 + \sigma_2 + \sigma_3}{3\bar{\sigma}} = \frac{\sigma_m}{\bar{\sigma}} \tag{6}$$

The Lode angle is defined as the angle between the stress tensor that goes through the deviatoric plane and the axis of the principal stresses. Lode angle can be related to the third deviatoric stress invariant ξ after it is normalized:

$$\xi = \left(\frac{r}{q}\right)^3 = \cos(3\theta) \tag{7}$$

The geometrical representation of the Lode angle is shown in Figure 9. Because the range of Lode angle θ is $\left[0, \frac{\pi}{3}\right]$, the scope of ξ is $[-1, 1]$. Moreover, the Lode angle can also be normalized as

$$\bar{\theta} = 1 - \frac{6\theta}{\pi} = 1 - \frac{2}{\pi}\arccos(\xi) \tag{8}$$

And the parameter $\bar{\theta}$ is called the Lode angle parameter (Bai & Wierzbicki, 2008).

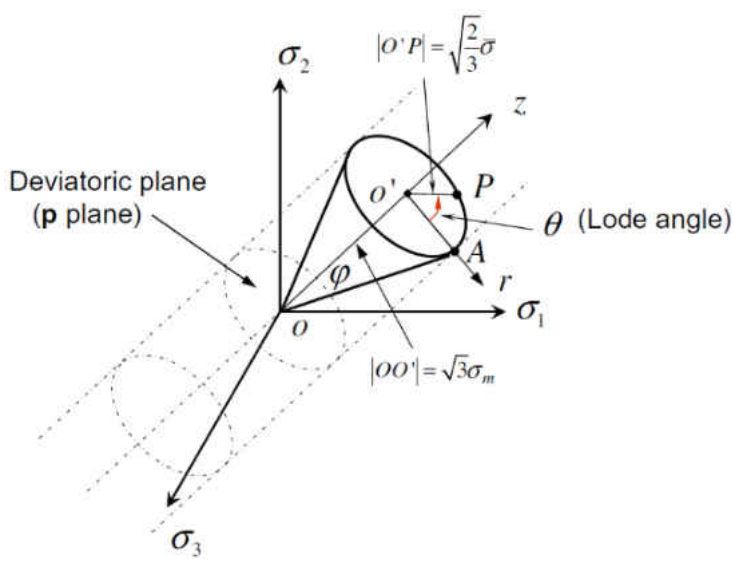

Figure 9. Schematic representation of three types of coordinate systems in the space of principal stresses (Bai & Wierzbicki, 2008)

With the above two parameters $(\eta, \bar{\theta})$ defined, all the loading conditions can be represented and characterized. Table 3 shows a list of values of stress triaxiality and Lode angle parameters for different types of specimens.

Table 3. Stress triaxialities and Lode angle parameters for different types of specimens. R is the radius of a notch, a is the radius of a notch for a round bar, and t is the thickness of the groove for a grooved plate (Bai & Wierzbicki, 2008).

Specimen type	Analytical solution of stress triaxiality η	The Lode angle parameter $\bar{\theta}$
Smooth round bar, tension	$\frac{1}{3}$	1
Notched round bar, tension	$\frac{1}{3}+\sqrt{2}\ln\left(1+\frac{a}{2R}\right)$	1
Plastic plane strain, tension	$\frac{\sqrt{3}}{3}$	0
Flat grooved plates, tension	$\frac{\sqrt{3}}{3}\left[1+2\ln\left(1+\frac{t}{4R}\right)\right]$	0
Torsion or shear	0	0
Cylinders, compression	$-\frac{1}{3}$	-1
Equi-biaxial plane stress tension	$\frac{2}{3}$	-1
Equi-biaxial plane stress compression	$-\frac{2}{3}$	-1
Plastic plane strain, compression	$-\frac{\sqrt{3}}{3}$	0

Bai and Wierzbicki (Bai & Wierzbicki, 2008) proposed a plasticity model that takes the influence of stress triaxiality and Lode angle into consideration, and this model is employed for the plasticity study of copper. The potential function is listed in Eq. (9) and the plastic behavior regarding stress triaxiality, Lode angle dependency, and plastic strain is presented in Eq. (10).

$$f = \sqrt{\frac{3}{2}[\boldsymbol{S}]:[\boldsymbol{S}]} - \sigma(\bar{\varepsilon}_{pl}, \eta, \theta) = 0 \tag{9}$$

$$\sigma(\bar{\varepsilon}_{pl}, \eta, \theta) = \sigma_o(\bar{\varepsilon}_{pl})[1 - c_\eta(\tilde{\eta} - \eta_0)]\left[c_\theta^s + (c_\theta^{ax} - c_\theta^s)\left(\frac{m+1}{m}\right)\left(\gamma - \frac{\gamma^{m+1}}{m+1}\right)\right] \tag{10}$$

The first term $\sigma_o(\bar{\varepsilon}_{pl})$ in Eq. (10) is the isotropic strain hardening function. There are different popular functions to describe the work hardening phenomenon. Swift hardening law, Voce hardening law, and mixed Swift-Voce hardening law are often used for metallic materials. Based on experimental data, mixed Swift-Voce hardening law is employed here for copper and it has such form:

$$\sigma_o(\bar{\varepsilon}_{pl}) = \alpha[A(\varepsilon_0 + \bar{\varepsilon}_{pl})^n] + (1-\alpha)[k_0 + Q(1 - e^{-\beta\bar{\varepsilon}_{pl}})] \tag{11}$$

where A is the stress amplifier, n is called strain hardening exponent, and ε_0 is the strain shift parameter, α is the weighting factor, and similarly k_0, Q and β are parameters of Voce law. These parameters can be identified from the experimental data by trial and error method.

The second term $[1 - c_\eta(\tilde{\eta} - \eta_0)]$ in Eq. (10) represents the influence of hydrostatic pressure on the yield of materials. c_η is a material parameter that needs to be calibrated. η_0 is the reference value of stress triaxiality of the calibration test for the strain hardening function. For example, if the uniaxial tension test is used to calibrate the three parameters of swift hardening function (11), refer to Table 3, then $\eta_0 = \frac{1}{3}$. This is also the case in our work. Moreover, it should be noted that the stress triaxiality term (η) in the original PPL model has been modified to the modified stress triaxiality (η̃) which is defined in Eq. (12). As stated by Ghazali et al. (Ghazali, Algarni, Bai, &

Choi, 2020), the original PPL model might result in a double root solution in the regions of very high-stress triaxiality conditions.

$$\tilde{\eta} = \frac{\sigma_m}{\sigma_o} \tag{12}$$

where $\sigma_o = \bar{\sigma}(\bar{\varepsilon}_{pl})$ is the yield stress at the reference loading of η_0.

The third term in Eq. (10) is related to the Lode angle. Note that a correction term, $\frac{m+1}{m}$, is added to make the formula more stable in different conditions (Algarni et al., 2015). The definition of γ is shown in Eq. (15). Parameter γ stands for the difference between Tresca and von Mises in the deviatoric stress plane and the range of γ is $[0,\ 1]$. The value of c_θ^{ax} depends on the instantaneous value of Lode angle parameter and the relationship is shown in Eq. (16). The parameter c_θ^s is not necessary to be a constant when the shape of the yield surface evolves (Algarni et al., 2015). It shows that the value of c_θ^s changes for pure copper as the plastic deformation increases under certain conditions. As shown by Algarni et al. (Algarni et al., 2015), the value of c_θ^s does not change at $|\bar{\theta}| = 1$. However, c_θ^s is a function of Lode angle parameter and equivalent plastic strain when $|\bar{\theta}| = 0$. Following Algarni et al. method (Algarni et al., 2015), the formulation is presented in Eq. (13) and Eq. (14). The parameter c_θ^s is a function of Lode angle parameter and equivalent plastic strain. To make the yield locus smooth, a sigmoidal shaped model is used for $f(\bar{\theta})$ function which is controlled by B_3 and B_4 and an example is presented in Figure 10.

$$c_\theta^s(\bar{\varepsilon}_{pl}, \bar{\theta}) = B_0 + (B_1 - B_0)\left(e^{-B_2\bar{\varepsilon}_{pl}}\right)f(\bar{\theta}) \tag{13}$$

$$f(\bar{\theta}) = \left(1 - |\bar{\theta}|^{B_3}\right)^{B_4} \tag{14}$$

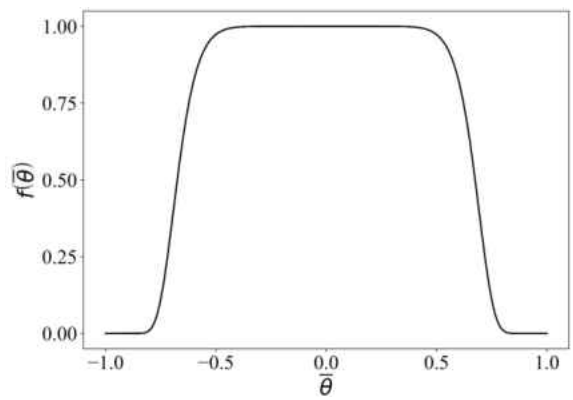

Figure 10. An example of the $f(\bar{\theta})$ function of parameter c_θ^s which is Lode angle parameter ($\bar{\theta}$) dependent on the material plasticity

There are another three material constants in Eq. (10) which are c_θ^c, c_θ^t and m and their values need calibration. The values of c_θ^s, c_θ^c, c_θ^t are relative and at least one of them is one. This is contingent on what kind of calibration test is used to calibrate the first term $\sigma(\bar{\varepsilon}_{pl})$. In this work, the value of c_θ^t is set to be 1 because smooth round tensile bar is taken as the reference of the material parameter calibration. The tension-compression asymmetry behavior is thus controlled by the Lode angle asymmetric parameter c_θ^{ax} which is shown in Eq. (16).

$$\gamma = \frac{\sqrt{3}}{2-\sqrt{3}}\left[\sec\left(\theta - \frac{\pi}{6}\right) - 1\right] \tag{15}$$

$$c_\theta^{ax} = \begin{cases} c_\theta^t & if\ \bar{\theta} \geq 0 \\ c_\theta^c & if\ \bar{\theta} < 0 \end{cases} \tag{16}$$

The modified Mohr-Coulomb fracture criterion is employed to predict the crack initiation and crack propagation under different loading conditions for copper. The fracture locus of the MMC model is shown in Eq. (17).

$$\bar{\varepsilon}_f(\eta,\bar{\theta}) = \left\{\frac{A}{c_2}\left[\tilde{c}_\theta^s + \frac{\sqrt{3}}{2-\sqrt{3}}(\tilde{c}_\theta^{ax} - \tilde{c}_\theta^s)\left(\sec\left(\frac{\bar{\theta}\pi}{6}\right) - 1\right)\right]\left[\sqrt{\frac{1+c_1^2}{3}}\cos\left(\frac{\bar{\theta}\pi}{6}\right) + c_1\left(\eta + \frac{1}{3}\sin\left(\frac{\bar{\theta}\pi}{6}\right)\right)\right]\right\}^{-\frac{1}{n}} \tag{17}$$

There are six parameters in Eq. (17), A, n, $\tilde{c}_\theta^s$, $\tilde{c}_\theta^{ax}$, c_1 and c_2. The parameters A and N can be taken from strain hardening function. In this study, they are taken the same values as that from the PPL model for the sake of simplicity. The value of $\tilde{c}_\theta^{ax}$ depends on the value of the Lode angle parameter (Eq. (18)): if the Lode angle parameter is greater than 0, $\tilde{c}_\theta^{ax} = 1$, otherwise $\tilde{c}_\theta^{ax} = \tilde{c}_\theta^c$. The four parameters $\tilde{c}_\theta^s$, $\tilde{c}_\theta^c$, c_1 and c_2, need to be calibrated from experimental data.

$$\tilde{c}_\theta^{ax} = \begin{cases} 1 & if\ \bar{\theta} \geq 0 \\ \tilde{c}_\theta^c & if\ \bar{\theta} < 0 \end{cases} \tag{18}$$

The fracture initiation and propagation are simulated by element deletion in this study and element deletion is control by the damage accumulation. Damage accumulation is a function of the equivalent plastic strain and is also related to stress triaxiality and the Lode angle parameter. The relationship is shown in Eq. (19), and when the damage accumulation is 1, the element is deleted.

$$D(\bar{\varepsilon}_{pl}) = \int_0^{\bar{\varepsilon}_{pl}} \frac{d\bar{\varepsilon}_{pl}}{\bar{\varepsilon}_f(\eta,\bar{\theta})} \tag{19}$$

3.3 Calibration of Material Models

Abaqus/Explicit is employed for the numerical simulation and the proposed PPL model and MMC fracture model are both implemented as Abaqus material subroutine (VUMAT). Smooth round bar test data is used first as a reference test to calibrate some essential parameters of the PPL plasticity

model and MMC fracture model. The force data is from the MTS test system and the displacement data is retrieved from DIC software. The engineering stress-strain curves can then be generated with the measured dimensions of the specimens. And the true stress-strain curves can be converted from engineering stress-strain curves with Eq. (20) and Eq. (21). The seven parameters from the strain hardening function (see Eq. (11)) are fitted with the true stress-strain data of uniaxial tension tests. Both Voce hardening law and swift hardening law are fitted to the experimental data. In this part, two different functions of hydrostatic pressure are presented and discussed.

3.3.1 Linear Function of Hydrostatic Pressure Effect

In this section, the parameter c_η is a constant. After it is calibrated by tensile tests, the normalized pressure effect on yield function is extrapolated for other loading conditions (Drucker & Prager, 1952; Spitzig & Richmond, 1984). After necking, the hardening curve is extrapolated by the combined swift-Voce hardening function by a weighting factor α, and the values are presented in Table 4. Since the retrieved true stress-strain data after specimen necking is not valid, only the data before necking is used for curve fitting. Through trial and error manner, the parameters are calibrated until there is a great match between the experimental data and the corresponding numerical simulations of the reference test. Then the parameters will be used for subsequent numerical simulations of all the samples.

$$\sigma_t = \sigma_e(1 + \varepsilon_e) \tag{20}$$

$$\varepsilon_t = ln(1 + \varepsilon_e) \tag{21}$$

Table 4. Calibrated material elastic-plastic properties for the finite element simulations.

Young's modulus, $E\ (GPa)$	Poisson ratio, ν	A	n	ε_0	α	k_0	Q	β
120000	0.36	386.5	0.365	0.773	0.1	353	247.7	0.719

Based on this, the other five parameters of the PPL model will be calibrated through finite element simulations, and the calibrated data are shown in Table 5. Regarding the parameters for the MMC model, the parameters A and n are taken from the calibrated power hardening function. The other four parameters of the MMC model can be initially estimated from the experimental data. Because there are errors in experiments and measurements, the initial estimation can provide a relatively good result, but it might not be very accurate. Then finite element simulations are used for further calibration. Please refer to Table 6 for the calibrated values of the parameters.

Table 5. Calibrated material plasticity parameters for PPL model

c_η	η_0	c_θ^t	c_θ^c	m	B_0	B_1	B_2	B_3	B_4
0.145	0.333	1.0	0.83	4.0	0.815	0.96	2.0	5.0	48.0

Table 6. Calibrated material fracture parameters for the MMC model

c_1	c_2	$\tilde{c}_\theta^s$	$\tilde{c}_\theta^c$
4.71	2492.3	1.035	1.0

All the finite element models are developed in Abaqus. To improve the computational speed and considering the symmetric conditions, smooth round tensile bars, large tensile bars, and sharp tensile bars are modeled with 4-node axisymmetric elements (CAX4R). Large compression bars, small compression bars, and torsion bars are modeled with 8-node solid elements (C3D8R).

To verify the finite element mesh convergency, mesh size dependence studies were carried out. For each specimen type, Different mesh sizes (0.125mm, 0.25mm) are selected and compared for tension FE simulations (uniaxial tension and notch tensions). Figure 11 provides the results of uniaxial tension simulations with different mesh sizes. The mesh size of 0.25 mm provides enough calculation accuracy and it is used for all the tension simulations. Similarly, different mesh sizes (0.25mm, 0.5mm, and 0.75mm) are checked for compression FE simulations (small compression cylinder and large compression cylinder). Figure 12 shows the small compression cylinder simulation results as an example. The mesh size of 0.5 mm offers good convergence and this mesh size is employed for both the compression simulations.

Regarding the torsion simulation, mesh sizes of 0.06mm and 0.1 mm are compared which are presented in Figure 13. When the plastic deformation is very large ($rotation \geq 300^o$), the two torque-rotation curves deviate from each other a little. This is partly caused by the nature that, unlike tensile and compression phenomena, shear is a much more localized phenomenon, which means that mesh size can greatly influence the shear simulation results. However, to keep the computational time of shear simulation at an acceptable level, extremely fined mesh is not investigated in this research. The mesh size for torsion simulation is 0.1 mm. Figure 14 presents the different finite element models of different types of specimens investigated in this study.

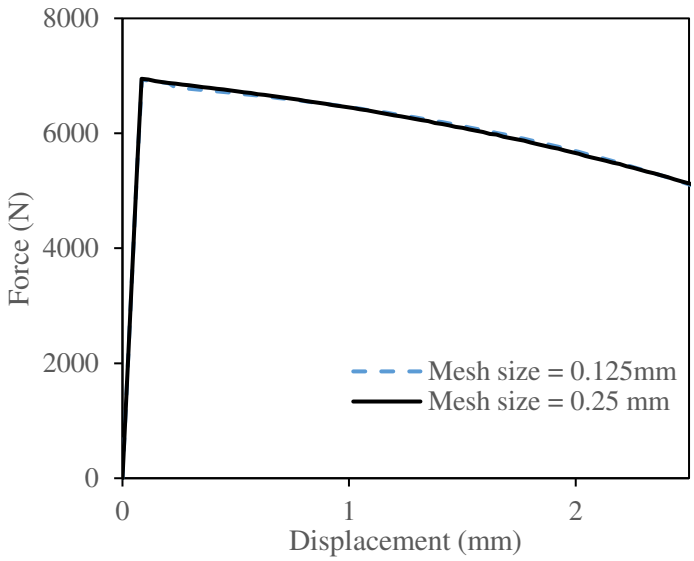

Figure 11. Finite element mesh convergency study of uniaxial tension simulation. The results show that the mesh size of 0.25 mm is fine enough.

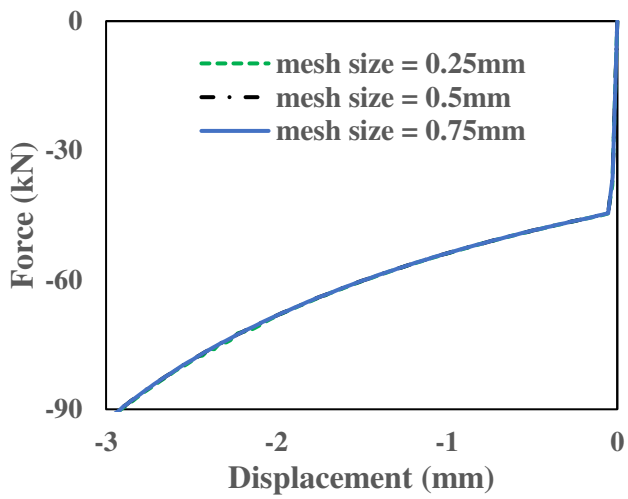

Figure 12. Finite element mesh convergence study for small compression cylinder. The results show that the mesh size of 0.5 mm is fine enough.

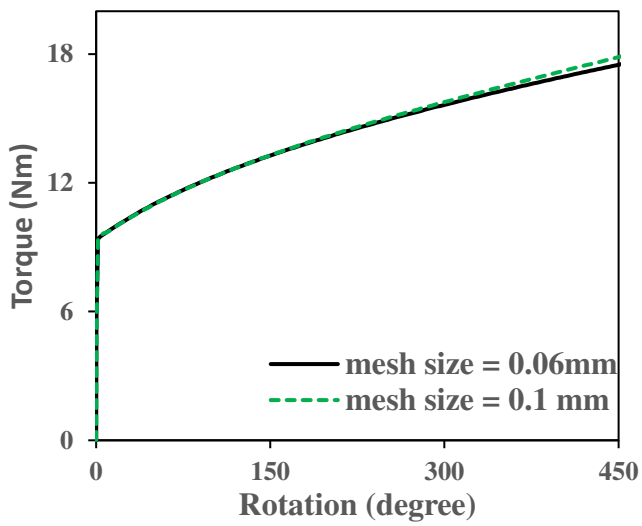

Figure 13. Finite element mesh convergence study for torsion simulation. The results show that the mesh size of 0.1 mm can provide a convergent result when the plastic deformation is not too large ($rotation \leq 300^o$). When the plastic deformation is very large, the results are not exactly the same. For instance, there is a 1.9% difference of the resultant torque for the two mesh sizes when the rotation= 450°. Shear deformation is essentially a localized phenomenon, and this means that mesh size would have an important influence on the simulations. To keep the computational time at a reasonable level, a mesh size of 0.1 mm is used.

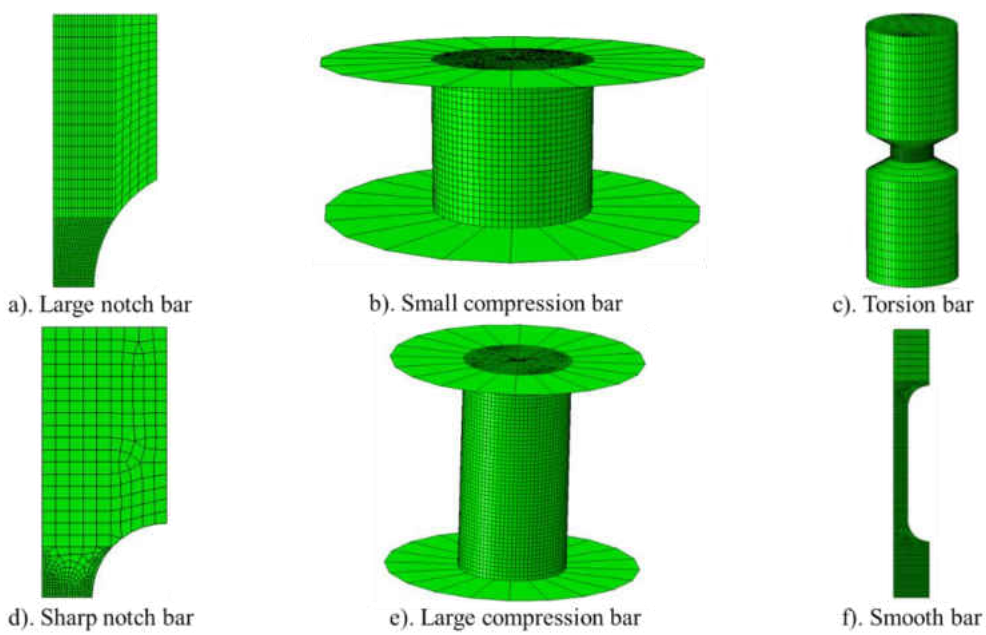

Figure 14. Finite element meshes of different types of specimens.

The displacement data in simulations are extracted from the same locations as that where the DIC software is used to extract experimental displacement data. The force data in simulations are gathered from the top surface of each model. The comparisons between experiments and

simulations are provided from Figure 15 to Figure 20. Good fits between experiments and simulations for tensile tests and compression tests are achieved. In each of the above figures, the equivalent plastic strain contour plot is presented for the finite element simulation. And in the VUMAT subroutine of ABAQUS\Explicit, the equivalent plastic strain is stored as solution dependent variable SDV1 and it's defined in Eq. (22).

$$\bar{\varepsilon}_{pl} = \bar{\varepsilon}_{pl0} + \int_0^t \dot{\bar{\varepsilon}}_{pl} dt \tag{22}$$

where $\bar{\varepsilon}_{pl0}$ is the initial equivalent plastic strain, $\dot{\bar{\varepsilon}}_{pl}$ is calculated via the von Mises plasticity model $\dot{\bar{\varepsilon}}_{pl} = \sqrt{\frac{2}{3}\dot{\boldsymbol{\varepsilon}}_{pl} : \dot{\boldsymbol{\varepsilon}}_{pl}}$.

The friction coefficient between compression samples and the compression platform of the testing machine is unknown, and the friction coefficient is iteratively adjusted within the FE simulations so that the final deformed geometries fit with the corresponding testing results. The friction coefficient used in the compression simulations is 0.1.

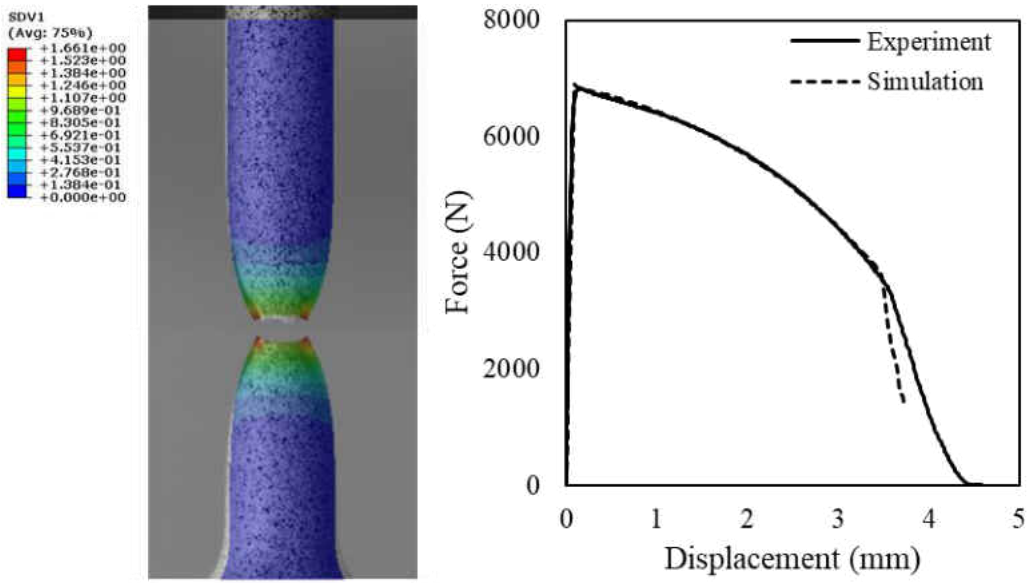

Figure 15. Comparison between experiment and simulation for smooth round tension bar.

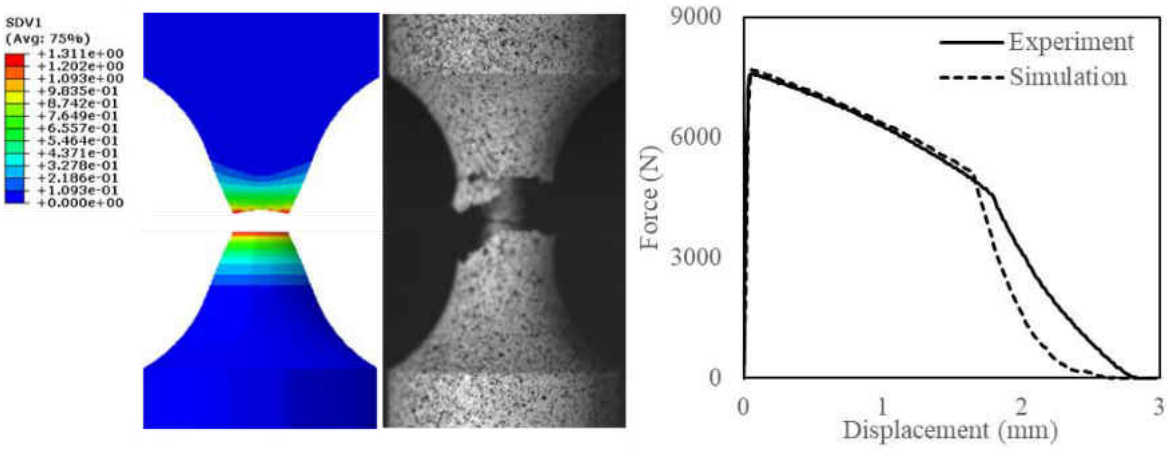

Figure 16. Comparison between experiment and simulation for large notch tensile bar.

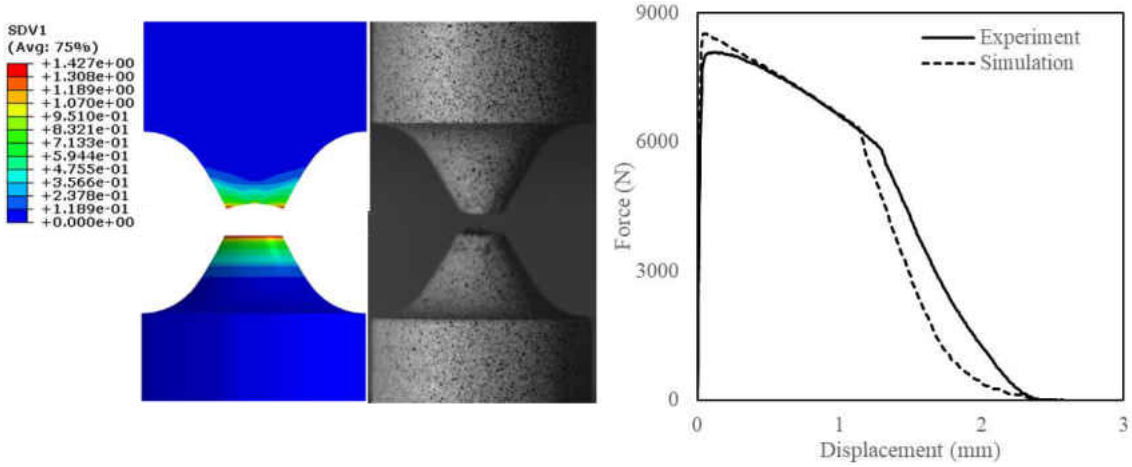

Figure 17. Comparison between experiment and simulation for sharp notch tensile bar.

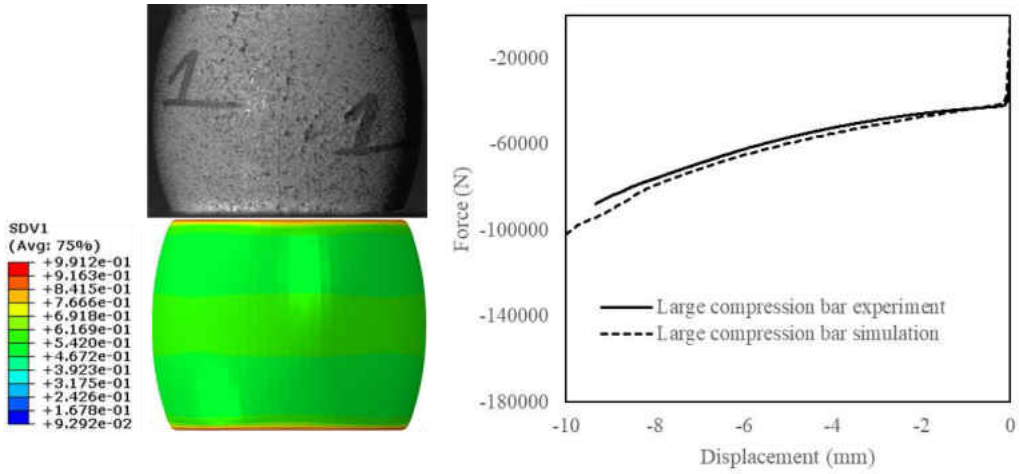

Figure 18. Comparison between experiment and simulation for large compression bar.

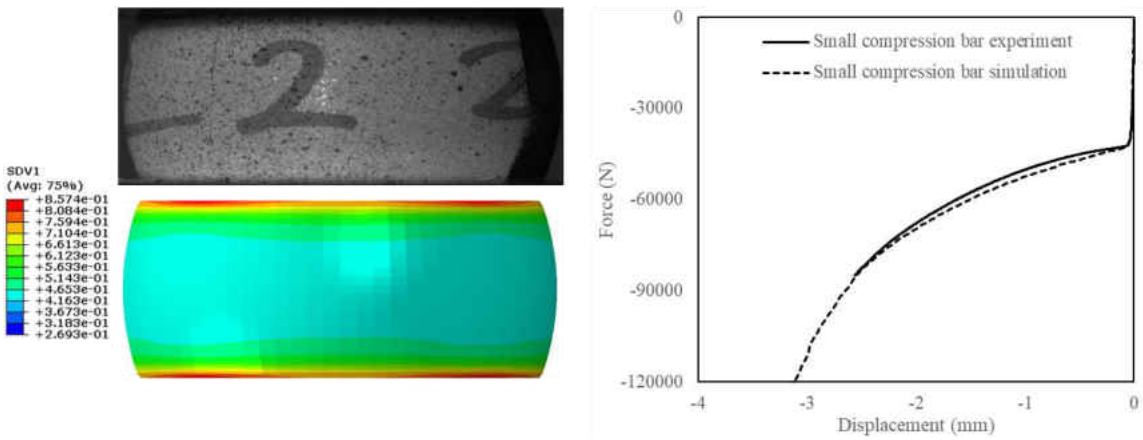

Figure 19. Comparison between experiment and simulation for small compression bar.

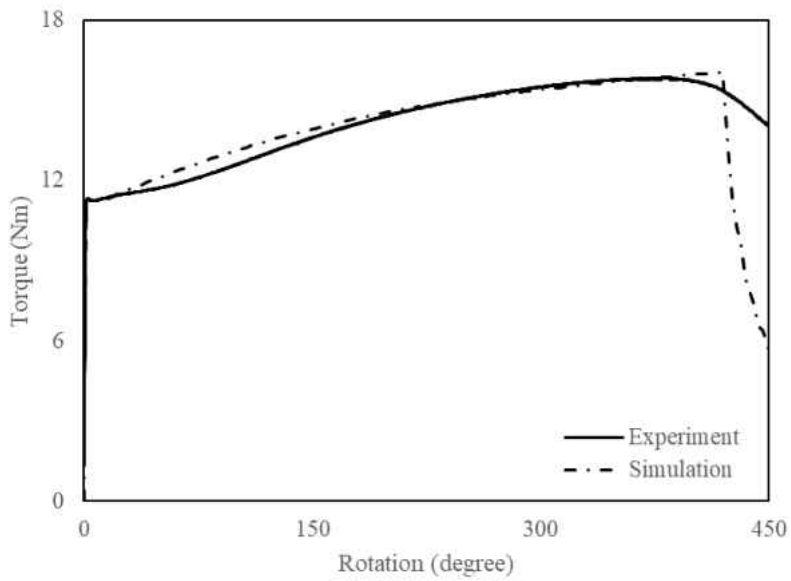

Figure 20. Comparison between experiment and simulation for torsion bar test.

As the specimen deformation gets larger, the stress triaxiality and Lode angle parameter change with the increase of equivalent plastic strain. The evolution of these two stress state variables alongside the equivalent plastic strain in the necking center is shown in Figure 21 and Figure 22 for the tensile specimens. It can be seen that the stress triaxiality of the two notched specimens has a sharp increase in the beginning period of plastic deformation, then the value evolves gradually.

However, the stress triaxiality of the smooth bar increases gradually with the increase of equivalent plastic strain. On the contrary, the Lode angle parameter for all three specimens shows a small deviation from the theoretical value.

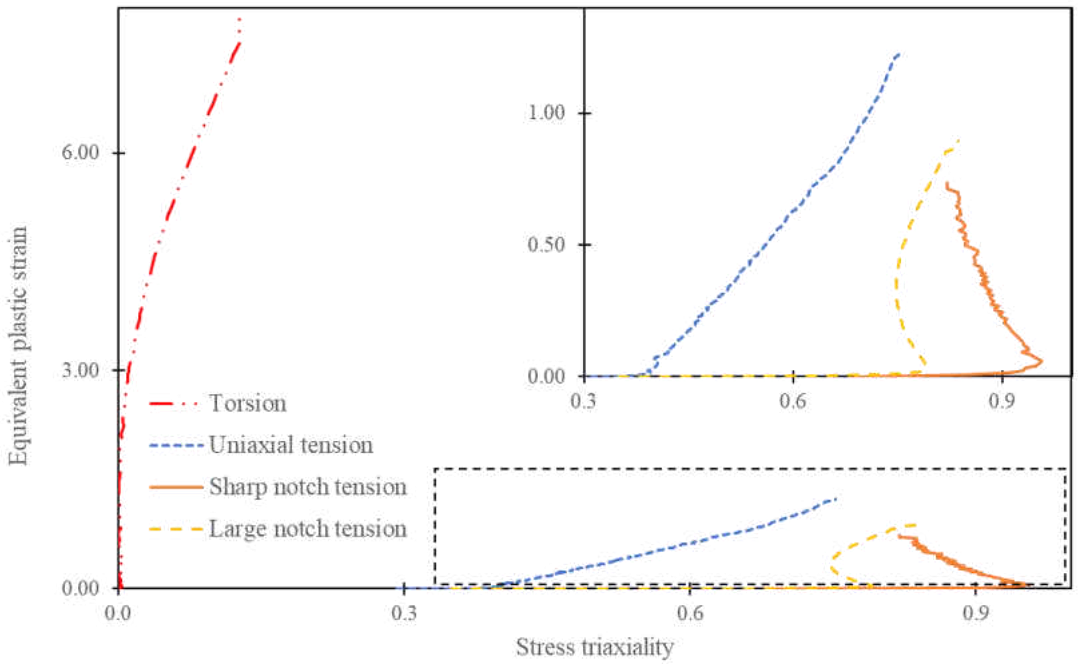

Figure 21. Numerical stress triaxiality vs. equivalent plastic strain in the necking center of each tensile specimen, and numerical stress triaxiality vs. equivalent plastic strain in the edge of torsion specimen.

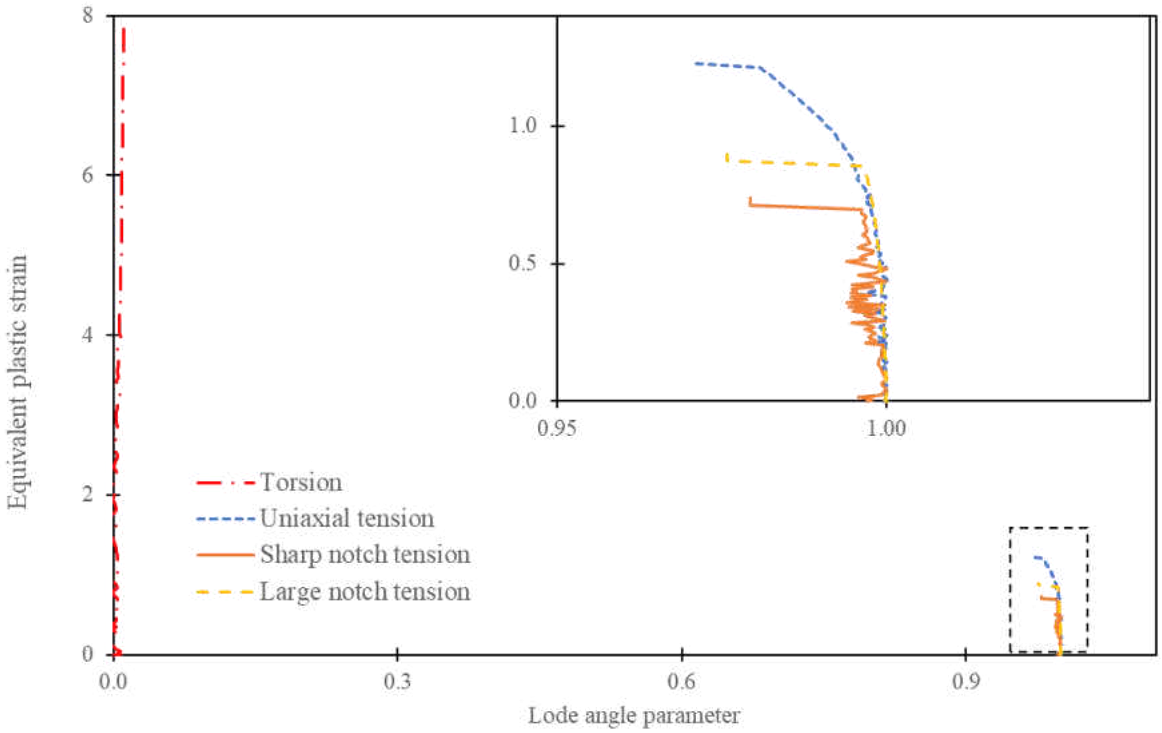

Figure 22. Numerical results of the Lode angle parameter vs. equivalent plastic strain in the necking center of each tensile specimen, and numerical stress triaxiality vs. equivalent plastic strain in the edge of torsion specimen.

The calibrated MMC fracture model is presented in Figure 23 along with theoretical values and simulation results. For the torsion specimen, the data are extracted from the circumferential element which first reached the element deletion criterion. As one can see, the theoretical values of tensile fracture strains are a little lower than those from the MMC fracture criterion. This is partly caused by the OFHC copper fracture mode. The fracture initiation point of OFHC copper is the necking center, and the necking edge is the last point to total fracture. Usually, the fracture strains of the necking center and necking edge are very close. But the ductility of OFHC copper is so good which makes the difference between these two fracture strains larger. When comparing the simulation fracture strain and experimental fracture strain, the simulation fracture strain is usually extracted from the necking center element (in this work, it's Figure 23) instead of the necking edge element. On the other hand, the experimental fracture strain is obtained by measuring

the fracture surface area which means that this calculated fracture strain is the average strain across the fracture surface.

Another reason is that the stress states will change during the experiment. For example, the theoretical value of stress triaxiality is 0.333 and the theoretical value of the Lode angle parameter is 1 for round bar tension. But as the specimen deformation gets larger, the actual values of the stress states are no longer the same as the theoretical values. So when we make a comparison between theoretical values and the MMC fracture criterion, instead of using the theoretical values, we need to use the actual values. However, it is almost impossible and extremely difficult to get the accurate values of the stresses, and finite element simulation provides an alternative way to achieve this.

The last possible reason is that the error from measuring fracture surface area. Since copper is very ductile, it takes some time from fracture initiation to full fracture and the specimen deforms a lot during this process. Moreover, the fracture surface is no longer circular. When one measures the fracture surface area, it is usually assumed that the fracture surface is circular. It is also very subjective to decide the full fracture point.

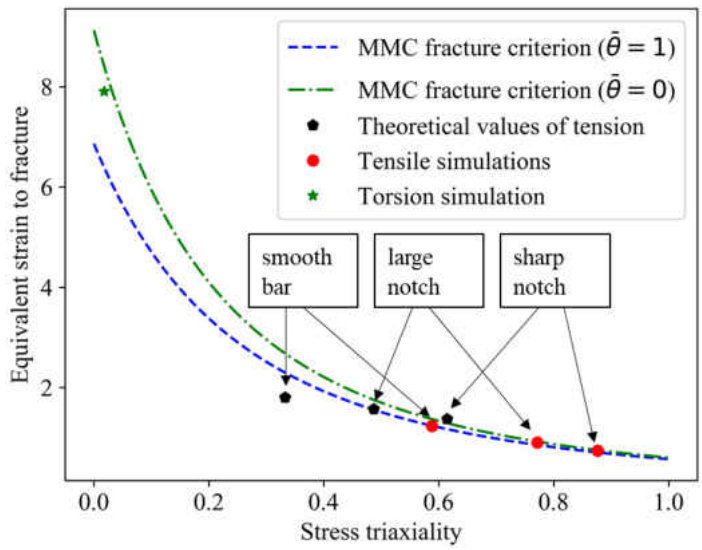

Figure 23. Comparison among calibrated MMC ductile fracture locus, theoretical values, and simulation results. Note that the used stress triaxiality values for the theoretical values of tension are assumed to be constant.

Contrary to the necking center element, the necking edge element provides another extreme example to compare with measured fracture strain. In order to correctly compare experimental data and MMC fracture criterion, the average stress triaxiality and average Lode angle parameter are used which are assumed to be the experimental stress triaxiality and Lode angle parameter. Therefore, these two values are used to calculate the fracture strains based on the MMC fracture criterion. The definitions of average stress triaxiality and average Lode angle parameter are shown in Eq. (23).

$$\eta_{avg} = \frac{1}{\bar{\varepsilon}_f}\int_0^{\bar{\varepsilon}_f} \eta(\bar{\varepsilon}_{pl})d\bar{\varepsilon}_{pl}\,, \bar{\theta}_{avg} = \frac{1}{\bar{\varepsilon}_f}\int_0^{\bar{\varepsilon}_f} \bar{\theta}(\bar{\varepsilon}_{pl})d\bar{\varepsilon}_{pl} \tag{23}$$

Figure 24 shows the history of stress triaxiality and the Lode angle parameter of the necking edge element for each tensile specimen. Comparing Figure 21, Figure 22, and Figure 24, it can be seen that both the stress triaxiality history and Lode angle parameter history follow a different pattern. Table 7 presents the comparison among experimental fracture strains, fracture strains from finite

element simulation, and MMC fracture criterion. Note that the finite element simulation fracture strains are from the necking edge element. The results show a good agreement among different methods.

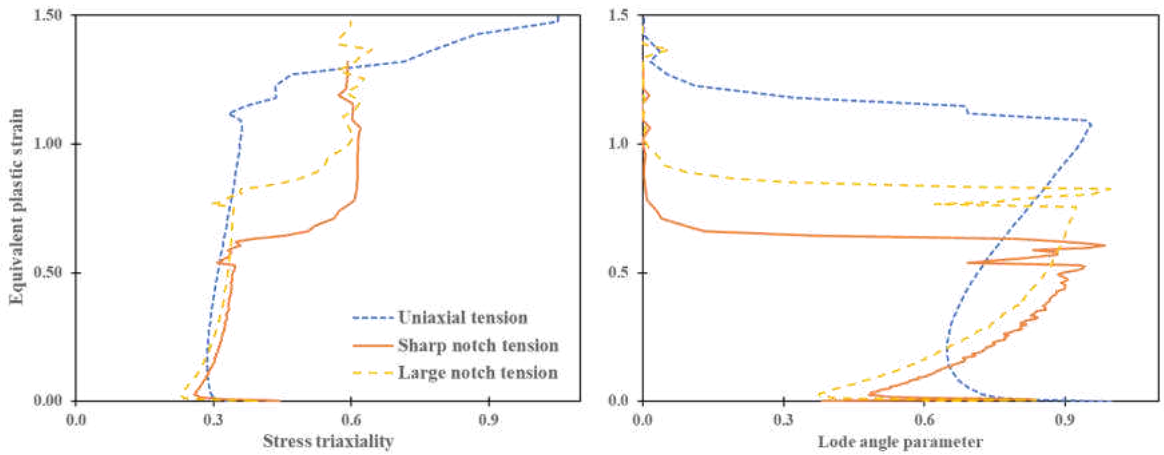

Figure 24. stress triaxiality and Lode angle parameter history of three tensile specimens from the necking edge element.

Table 7. The comparison among experimental fracture strains, MMC fracture criterion, and finite element simulations. The simulation data are extracted from the specimen necking edge point. Based on averages of the stress triaxiality history and Lode angle parameter history, the MMC fracture strains are calculated and compared with experimental data.

	Simulation			Fracture strain from experiment	Fracture strain from MMC
	Average stress triaxiality (η_{avg})	Average Lode angle parameter ($\bar{\theta}_{avg}$)	Fracture strain		
Smooth bar	0.4193	0.594	1.513	1.658	1.51
Large notch bar	0.431	0.437	1.48	1.520	1.349
Sharp notch bar	0.462	0.380	1.324	1.335	1.216

The compression specimens are not compressed to fracture due to the good ductility of copper and the uniform deformation nature of the compression test. The fully calibrated fracture locus of OFHC copper is shown in Figure 25. Note that it only shows the cases when then stress triaxiality is larger than 0 because when the stress triaxiality is below 0, the fracture strain increases

drastically and the material will not fracture under normal conditions. Bao and Wierzbicki (Bao & Wierzbicki, 2004) and Bai and Wierzbicki (Bai & Wierzbicki, 2015) show that a cutoff region exists for ductile metallic materials. When the stress triaxiality is below a certain value, the specimen won't fracture. As a very ductile material, there is also the fracture cutoff region for OFHC copper. The results show that the OFHC copper specimens won't break under compression-dominated loadings. The tension-dominated loadings have the lowest strain to fracture values compared to other loading conditions, though the strain to fracture values are still very high when compared to other common metallic materials. The modified Mohr-Coulomb fracture model can accurately describe this behavior. Moreover, we can also conclude that even when the stress triaxiality is not very small, but if the Lode angle parameter is below -0.5, the fracture strain can still be very high.

The corresponding yield locus under plane stress loading condition is plotted in Figure 26 and the yield locus in the deviatoric stress plane is shown in Figure 27. They show that the yield surface is kind of concave when the plastic strain is small. This is partly caused by the c_θ^s being a function of Lode angle parameter. In the current modeling method, c_θ^s gets smaller as the plastic strain becomes larger when Lode angle parameter is close to 0. So the yield surface becomes less concave at large plastic strain. The reason that c_θ^c and c_θ^s are relatively small is caused by the relatively large value of c_η. Currently, a linear relationship between hydrostatic pressure effect and material hardening is assumed. The parameter of hydrostatic pressure is calibrated based on three tensile tests (one smooth bar and two notch bars), then the correction parts from hydrostatic pressure for shear test and compression tests are obtained via extrapolation. However, the linear relationship

assumption may not be the case. In the next part, a new set of study is carried out and $c_\eta\left(\eta < \frac{1}{3}\right) = c_\eta(\eta = \frac{1}{3})$ is assumed.

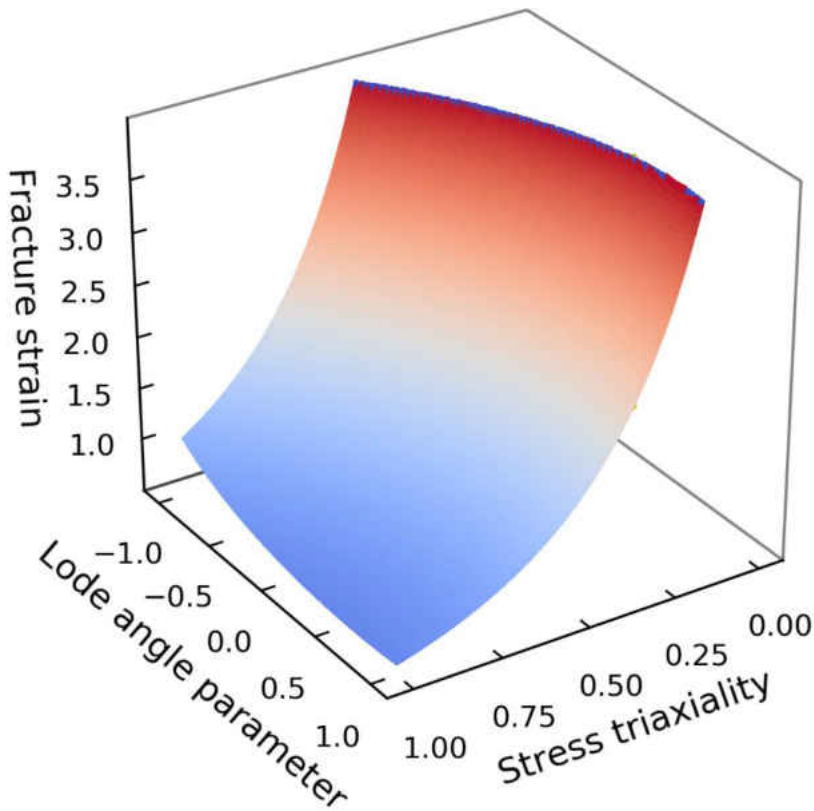

Figure 25. Calibrated MMC 3D fracture locus corresponding to monotonic testing results of OFHC copper.

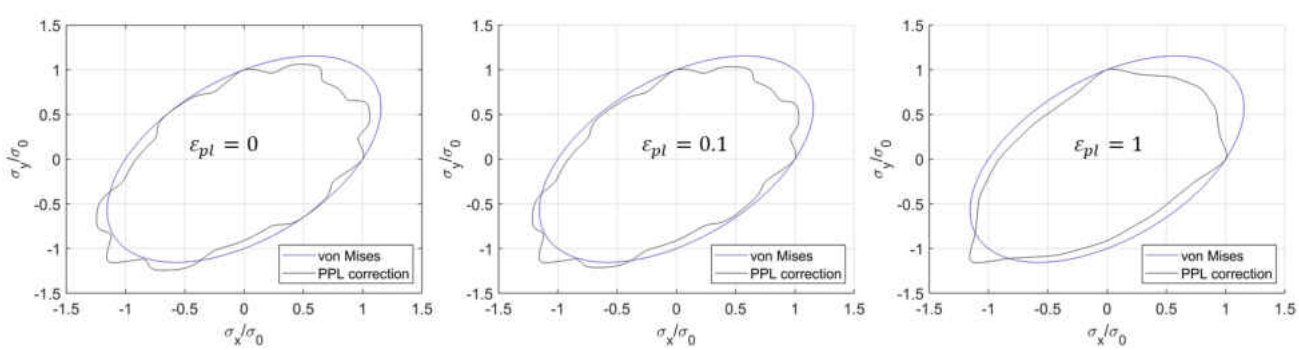

Figure 26. Evolution of yield locus with PPL plasticity model correction under plane stress loading condition.

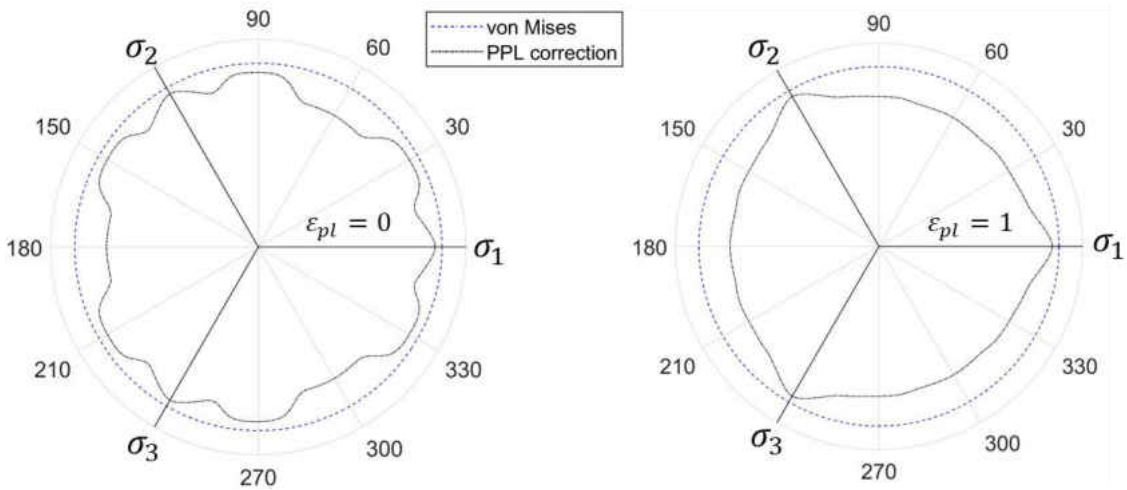

Figure 27. The initial yield surface in the deviatoric stress plane

3.3.2 Piecewise Function of Hydrostatic Pressure Effect

The influence of normalized pressure on the yield function is not necessarily a linear function though a linear function can give a simple and straight relationship. In this part, a piecewise function of the hydrostatic pressure effect is assumed and is shown in Eq. (24). In this case, the uniaxial tension test is used as the reference test, so the triaxiality of 1/3 is employed as the endpoint of two subdomains. The value of 0.145 is still calibrated by uniaxial tension test and notch tension tests.

$$c_\eta = \begin{cases} 0.145 & if\ \eta \geq \frac{1}{3} \\ 0 & if\ \eta < \frac{1}{3} \end{cases} \tag{24}$$

It should be noted that in theory, the yield locus should be smooth without any sharp point. But in this case, the process is simplified since explicit code is used here. The calibration process is the same as shown in the previous section. To simplify the calibration process, instead of assuming

the parameter c_θ^s as a function of plastic strain and Lode angle parameter, c_θ^s is viewed as a constant in this section. The calibrated plasticity model parameters and fracture model parameters are presented in Table 8 and Table 9, respectively. The comparison between experimental data and simulations is shown in Figure 28 for the torsion sample and two compression samples. It shows that a decent correlation has been achieved between experiments and simulations. With the setting of c_η being 0 when the stress triaxiality is below 1/3, the values of c_θ^c and c_θ^s have been improved, and the convexity situation has been greatly improved.

Table 8. Calibrated material plasticity parameters for PPL model with piecewise function of hydrostatic pressure effect

c_η	η_0	c_θ^t	c_θ^c	m	B_0	B_1	B_2	B_3	B_4
Refer to Eq. (24)	0.333	1.0	0.94	4.0	0.94	0.94	0	0	0

Table 9. Calibrated material fracture parameters for the MMC model with piecewise function of hydrostatic pressure effect

c_1	c_2	$\tilde{c}_\theta^s$	$\tilde{c}_\theta^c$
4.71	2492.3	0.93	1.0

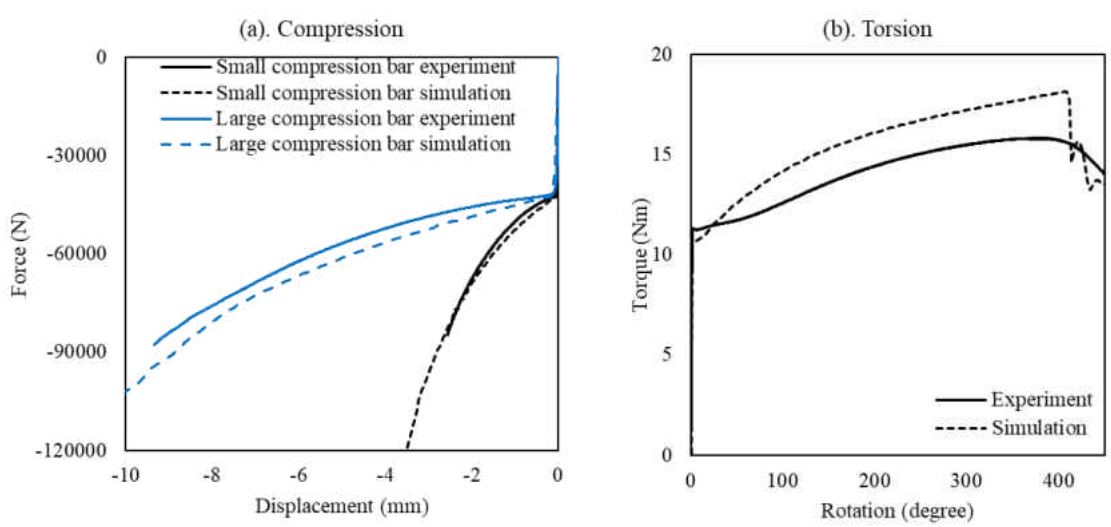

Figure 28. Comparison between experiment and simulation for (a). compression bars and (b). torsion bar.

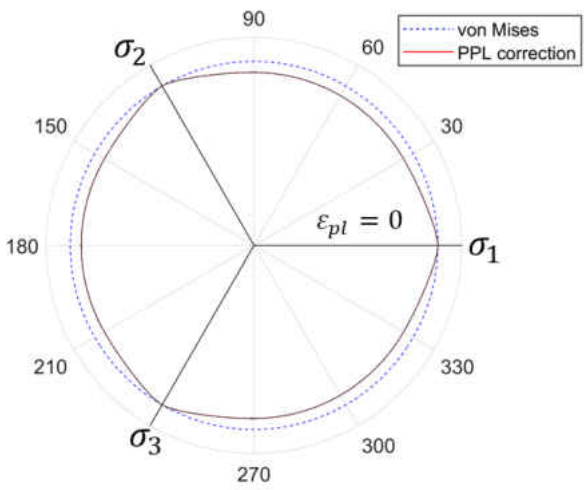

Figure 29. The initial yield surface in the deviatoric stress plane with the calibrated PPL plasticity model parameters

3.4 Summary

In this work, experimental and numerical simulation results are presented for OFHC copper. Six types of specimens (smooth round tensile bar, large notch bar, sharp notch bar, large compression bar, short compression bar, and torsion bar) that cover different loading conditions are designed and tested in quasi-static loading under room temperature. It is shown that OFHC copper has stress-state dependent plasticity and fracture behaviors. The main conclusions include:

- The plasticity of OFHC copper has stress-state dependent property and considering the influence of different stress states will provide more accuracy on the description of material plasticity behavior. The PPL model will help achieve this goal.
- The stress state has a great effect on the ductility of OFHC copper and the MMC model can predict its fracture initiation and propagation. The fracture cutoff region exists for OFHC copper fracture.

- Both the experiments and simulations demonstrate that different loading conditions present different plasticity and fracture characteristics and this displays the importance of thorough calibrations of the material models under a wide range of stress states.
- When comparing the fracture strains of experiments and simulations, special attention should be paid to ductile materials like copper. The stress state characteristics change a lot from the necking center to the necking edge. The necking center element might not be representative to be used for comparison with measured experimental fracture strain.
- Moreover, the experimental results present that OFHC copper shows very slight strain hardening and that the applied force drops for tensile specimens once the specimen goes into plastic deformation. This phenomenon makes OFHC copper very limited on pure mechanical based applications. However, because of the exceptional thermal conductivity and electrical conductivity of copper and excellent mechanical properties of inclusions like carbon nanotubes and graphene nanoplatelets, copper-based composites would improve the strength of copper and the composites would have great strength as well as great electrical conductivity and thermal conductivity. On the other side, the ductility of copper-based composites would inevitably decrease due to the addition of inclusions. How a small number of inclusions like carbon nanotubes or graphene nanoplatelets would change the mechanical properties like strength and ductility of copper will be presented in the future study considering the influence of stress states based on the current results.

CHAPTER 4 STRENGTHENING MECHANISM OF NICKEL COATED AL/CNT COMPOSITES

This chapter investigates a new group of aluminum matrix CNT reinforced nano-composites. Different from the direct mixing of CNTs with metal matrix (for example, Al, Cu, etc.) which usually comes across difficulties of CNTs clustering or agglomeration (A. Esawi & Morsi, 2007), this new group of nano-composite is reinforced by CNTs pre-coated with a nickel layer, where the CNTs are distributed uniformly. Over 200 RVE finite element models containing aluminum matrix, nickel coating, and CNTs are created to investigate the strengthening mechanisms of Al/NiCNT nano-composites. An interfacial zone is added to the RVE model for the consideration of the plastic hardened zone and Orowan effect. Extensive numerical simulations are carried out to find out the effects of different model parameters. Analytical solutions are also provided to predict and understand the stress-strain behaviors of these nano-composites fabricated with different weight fractions of NiCNTs.

4.1 Experimental Results

For the current study, MWCNTs were purchased from Cheap Tubes Inc. with purity greater than 95% (CheapTubes). CNTs that were used had a diameter between 8-15 nm with an axial length between 10–50 μm. Al powder was purchased from Alfa Aesar with a mesh size of -325 and purity of 99.8%. CNTs were first ultrasonically dispersed in an aqueous solution of HNO_3 (70%) at 80 ℃ for 2 hours for purification to remove all the impurities (Billah & Chen, 2017; Peng, Hu, & Wang, 2007). HNO_3 treatment also alters surface properties for better dispersion in the electrolyte which is essential for the high-density activation sites formation in the subsequent reactions (B. Zhao, Yadian, Li, Liu, & Zhang, 2009). This process has great importance to improve the adherence of metallic particles to CNT surfaces. CNTs were then rinsed with deionized (DI) water. Each time,

rinsing was continued until the solution was neutral. The functionalized nanotubes were then coated with Ni in a two-step electroless nickel deposition process. At first, CNTs were ultrasonically dispersed in the electroless plating solution (Table 10) under ultra-violate (UV) exposure for 20 minutes, and then $NaBH_4$ solution was added to form the NiO clusters as the catalytic sites to activate the CNTs [24]. Following washing CNTs with DI water, the activated CNTs were dispersed again into the plating solution at 50 ℃ for 20 minutes. Ammonia solution was used to adjusted pH to 8.5. Finally, the Ni-coated CNTs were cleaned with DI water, filtered off, and dried. Figure 30 (a) shows an example of Ni-coated CNTs.

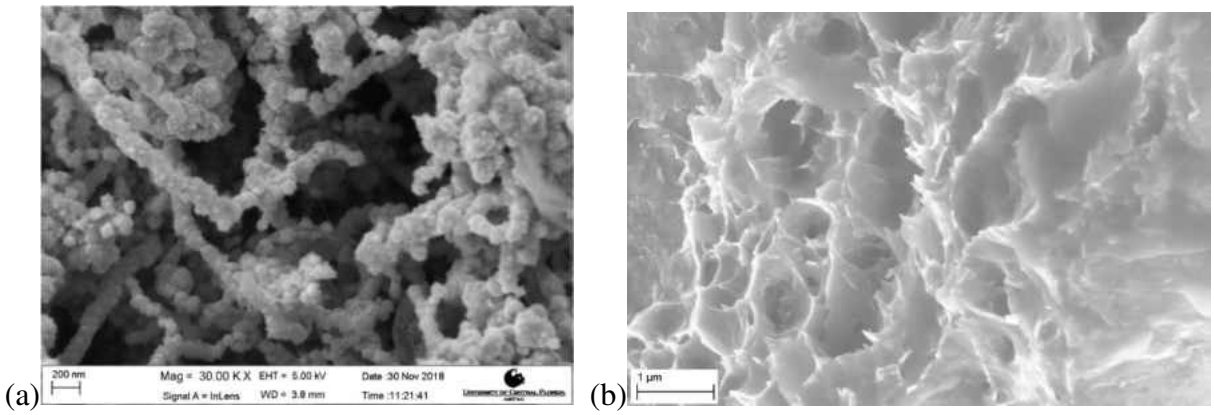

Figure 30. (a). Ni-coated CNTs where CNTs are fully encapsulated. (b). An example of the fracture surface of Al/NiCNTs nano-composites showing no interface debonding during loading.

Ni-coated CNTs were then ultra-sonicated for 2 hours in ethyl alcohol to avoid agglomeration. Later after adding Al powders, the mix was further ultra-sonicated for 2 hours. Then the mixture was dried and pressed into a pellet of 13mm diameter under a unidirectional pressure of 400 MPa. All the pellets were sintered in the pure nitrogen atmosphere. Hot Isostatic Pressing (HIP) was used for further consolidation at 550 ℃ for 90 minutes at 200 MPa pressure.

The effects of Ni-coated CNTs' addition on tensile strength were investigated using a Mechanical Testing and Simulation (MTS) Tytron 250 tensile test machine in the lab. Rectangular tensile

specimens were prepared according to ASTM E8/E8M–09. One example fracture surface of Al/NiCNT nano-composites is provided in Figure 30 (b). Note that the interface between CNTs and metals was well bonded without debonding.

Table 10 Ni Plating Bath Composition

$Chemicals$	$Concentration\ (g/L)$
$NiSO_4 \cdot 6H_2O$	8
NaH_2PO_2	35
$C_6H_5Na_3O_7$	18
$NH_3\ solution$	$For\ pH\ adjustment$

Different weight fractions of CNTs are used to investigate the strengthening effect. Typical results of calibrated engineering stress-strain curves for pure aluminum and two Al/NiCNT nano-composites (0.5% wt. and 1% wt. of NiCNTs) are shown in Figure 31. The weight ratio of Ni and CNTs is 81.5:18.5 for all NiCNTs used in this work. One can see that a small amount of CNTs significantly increase the nano-composites' strength by 100%. The material ductility is decreased accordingly as a side effect.

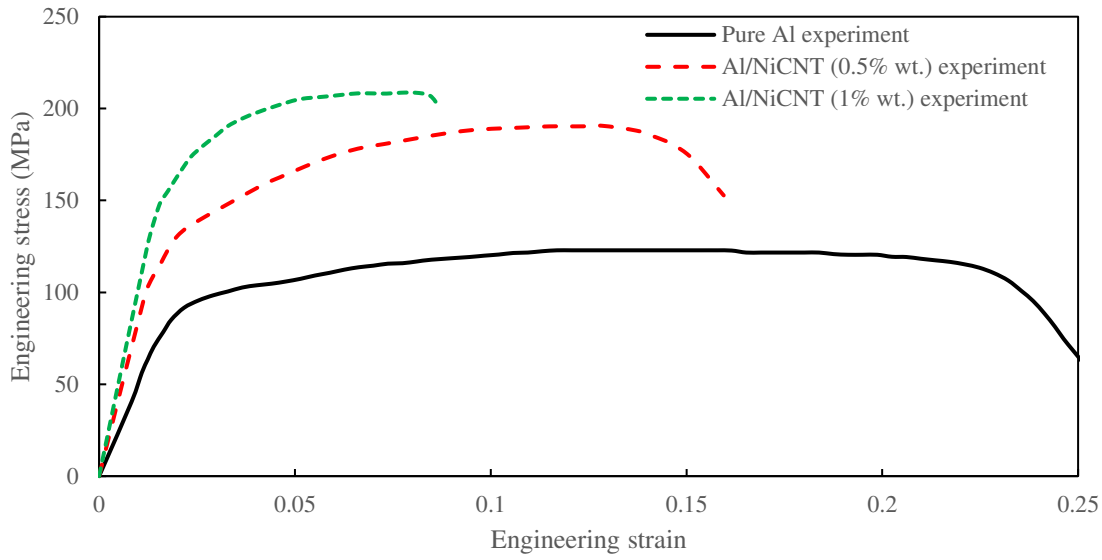

Figure 31. Calibrated engineering stress-strain curves of both pure aluminum and Al/NiCNTs with different weight fractions of NiCNTs

4.2 Finite Element Simulation using RVE

4.2.1 Model Setup

To understand the strengthening effects of CNTs on aluminum matrix material, a finite element model using Abaqus is built, which is composed of four parts. See Figure 32. The inner part is CNTs; the part near CNTs represents nickel coating; the outside part stands for pure aluminum; the part between nickel and pure aluminum is the interface of hardened aluminum which can be caused by Orowan effect and/or the thermal expansion mismatch which originates from the manufacturing process. Axisymmetric elements (CAX4R in Abaqus) are used along the y-axis, so it is simplified to a 2D finite element problem in Abaqus/Standard. A symmetric boundary condition is applied along the x-axis, and this further increases the computation efficiency. As pointed by Long et al. (Long et al., 2015), the boundary condition along the right edge can effectively influence the prediction of the CNT strengthening mechanism, where linear constraint

equations are necessary along the right edge of the model to keep the right edge vertically aligned during deformation.

There are some key model geometry parameters to be studied. The radii of CNTs, nickel, hardened zone and pure aluminum are represented by R_{CNT}, R_{Ni}, R_H, and R_{Al}, and the heights of these four parts are denoted by H_{CNT}, H_{Ni}, H_H, and H_{Al}, respectively. By adjusting these parameters, different aspect ratios, different volume fractions of CNTs, and different volume fractions of the hardened zone will be collocated for a round of comprehensive parametric studies. Moreover, since the CNTs are well dispersed in aluminum and the nickel coating tremendously improved the interfacial bonding, interfacial debonding is not considered in this study.

The commercial software package of Abaqus (Systèmes, 2012) is used for the finite element analysis. A Python script is written for the parametric study, the flowchart of which is shown in Figure 33. Firstly, Python is utilized to create FE model meshes, assign material properties and boundary conditions. This information is then saved into an Abaqus input file. Secondly, the input file will be submitted to the Abaqus solver, and the simulation will start. When the simulation is done, an ODB file (Abaqus' output result) will be generated. Finally, Python will read the Abaqus result file, and extract force and displacement data, so the simulated stress-strain relationship can be acquired. When a round of process is finished, a new process resumes with a new set of parameters.

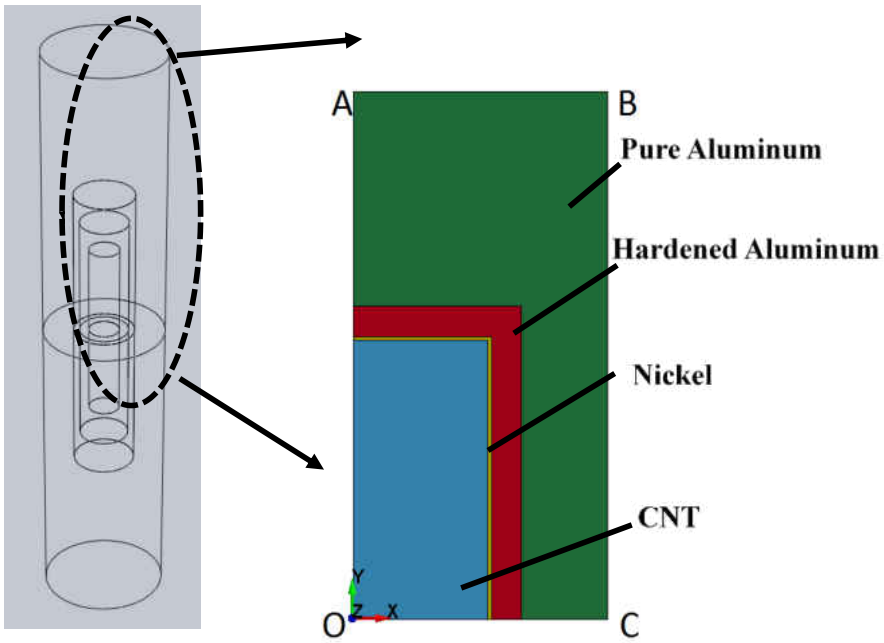

Figure 32. A sketch of RVE model for Al/NiCNT nano-composites

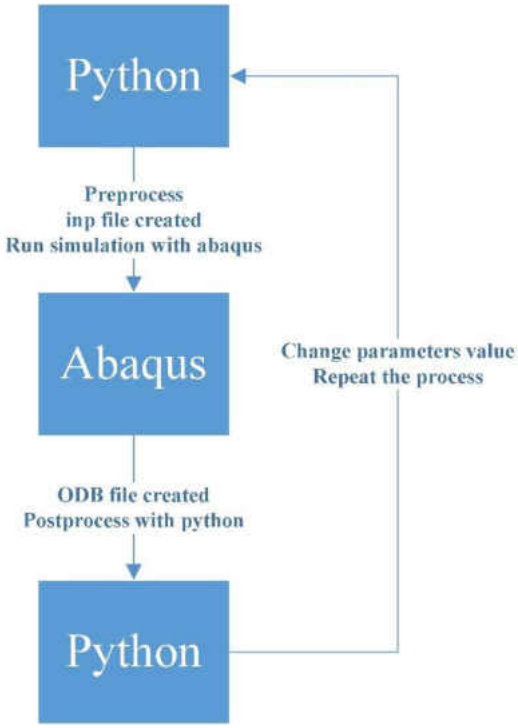

Figure 33. A simulation flow chart for parametric studies

4.2.2 Mechanical Properties of Aluminum Matrix

Serving as a controlled baseline, Billah (Billah, 2017) fabricated the pure aluminum tensile sample with the same procedure of manufacturing Al/NiCNT nano-composites presented in this paper. Similarly, the MTS Tytron 250 tensile test machine was used for the tensile test, and the resultant load and displacement responses were measured. Then an engineering stress-strain curve was obtained from the force-displacement curve for the pure aluminum tensile test, which is shown in Figure 34. The true stress-strain curve before necking is obtained from the engineering stress-strain curve via these two equations.

$$\sigma = \sigma_e(1 + \varepsilon_e) \tag{25}$$

$$\varepsilon = ln(1 + \varepsilon_e) \tag{26}$$

Here, σ and ε are the true stress and the true strain, and σ_e and ε_e represent the engineering stress and the engineering strain, respectively. In our FE simulations, the values of Young's modulus, Poison's ratio, and density are taken from the open resource (Han & Fina, 2011), which are listed in Table 11.

Table 11 Mechanical properties of pure aluminum matrix used in FE simulations

Density, $\boldsymbol{\rho}$	Poison's ratio, $\boldsymbol{v}$	Young's modulus, $\boldsymbol{E}$	Initial yield stress, $\boldsymbol{\sigma_0}$
$\mathbf{2700}\,\boldsymbol{kg/m^3}$	$\mathbf{0.33}$	$\mathbf{69}\boldsymbol{GPa}$	$\mathbf{72}\boldsymbol{MPa}$

The stress-strain curve after necking can be described by the Swift hardening law function which is shown in Eq. (27).

$$\sigma = A(\epsilon_0 + \epsilon_p)^n \tag{27}$$

Here, A is the stress amplitude, ϵ_0 is the strain shift parameter, ϵ_p is the equivalent plastic strain, and n is called strain hardening exponent.

By a trial-and-error procedure (Bai & Wierzbicki, 2008), all the values of these parameters can be determined. $A = 204$, $n = 0.17689$, and $\epsilon_0 = 0.00285$ for this material. So the true plastic strain-stress data of pure aluminum is obtained for simulation.

With these given mechanical properties, one can get the plastic strain-stress relationship from uniaxial tension simulation, which is displayed in Figure 34. It shows that the simulation data fits the experimental data very well, and further studies can be performed for nano-composites.

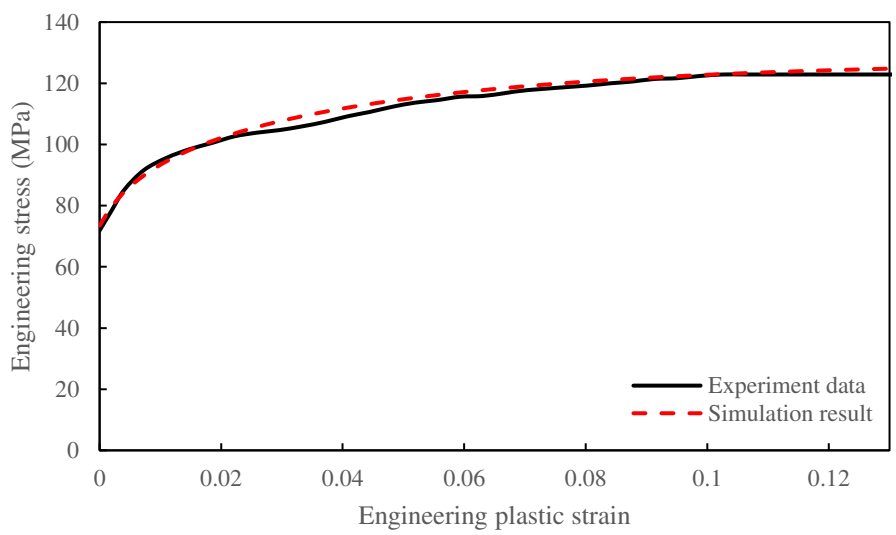

Figure 34. Comparison of engineering plastic strain- stress curves between experiment and simulation for pure aluminum matrix. A good correlation is achieved.

4.2.3 Mechanical Properties of CNTs and Nickel Coating

Regarding the mechanical properties of CNTs, Long et al.(Long et al., 2015) discussed the different influences of the pure elastic material model and elastic-plastic material model on composites strengthening effect, and it was found that the stress inside the CNTs could exceed the

elastic limit. Therefore, an elastic-plastic material model is selected for CNTs for the consideration of simulation accuracy. The stress-strain relationships (including initial yield stress and Young's modulus) of CNTs are also taken from the work of Long et al.(Long et al., 2015), which is illustrated in Figure 35.

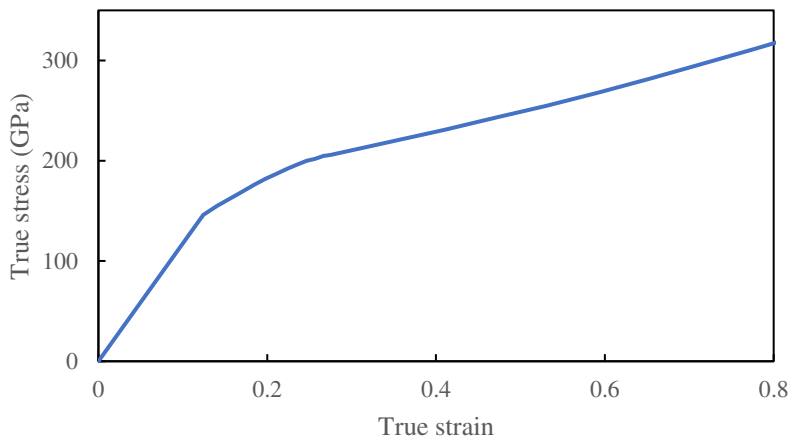

Figure 35. True stress-strain curve of CNT used in finite element simulations. Data adapted from Ref. (Long et al., 2015)

The volume fraction of CNTs is a key factor in the finite element analysis and analytical solutions. The weight fraction of CNTs is what we directly measured during experiments, and transformation from weight fraction to volume fraction is necessary using the information of CNT density. It is noted that different resources reported different densities of carbon nanotubes. Yang et al. (D. J. Yang et al., 2002) used a value of $1.34\ g/cm^3$ for the density of multiwalled carbon nanotubes. Gong et al.(Gong et al., 2004) fabricated aligned CNT/carbon composite by chemical vapor deposition of carbon on CNTs preform and sintered at about $1500°C$. The original density of aligned carbon nanotubes Gong et al.(Gong et al., 2004) used was $0.1\ g/cm^3$, and after densification process, the density of aligned CNT/carbon composites was $0.8\ g/cm^3$. Wang et al.(D. Wang, Song, Liu, Wu, & Fan, 2008) manufactured aligned CNTs thick buckypapers by special 'domino' pushing, and the density of the buckypapers by aligned CNTs is $0.62\ g/cm^3$,

while the density of the buckypapers by randomly oriented CNTs is $0.54\ g/cm^3$. Moreover, the original density of MWCNT array was about $0.032\ g/cm^3$. The CNTs that we used were from Ref. (CheapTubes), and it displayed that the bulk density of CNTs was $0.15\ g/cm^3$. The stress strain relationship (including yield stress and Young's modulus) of pure nickel is shown in Figure 36 according to Ref. (Ayer et al., 2014). A summary of other mechanical properties of CNTs and nickel used in FE simulations are displayed in Table 12.

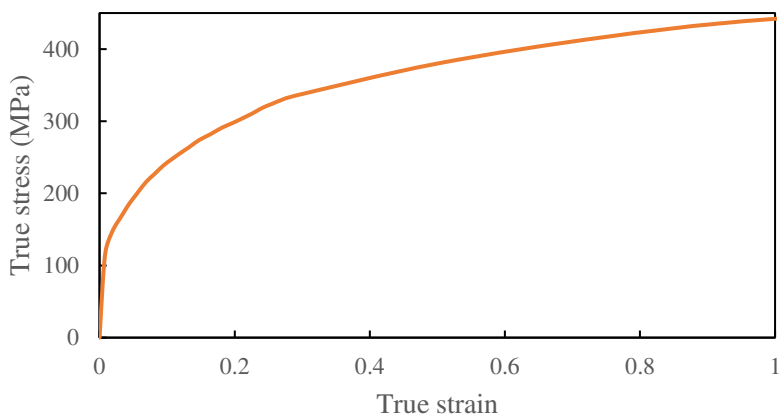

Figure 36. Stress-strain relationship of pure nickel used in simulations. Data adapted from Ref. (Ayer et al., 2014)

Table 12. Mechanical properties of CNTs and nickel used in FE simulations, Data adapted from Refs. (Ayer et al., 2014; CheapTubes; Long et al., 2015)

Materials	Density, ρ	Young's modulus, E	Initial yield stress, σ_0
CNTs	$150\ kg/m^3$	$1175GPa$	$163.3GPa$
Nickel	$8908\ kg/m^3$	$200GPa$	$120.6MPa$

4.3 Simulation Results and Parametric Studies

In this section, finite element simulation results of the RVE models will be presented and discussed. Since some model parameters cannot be directly measured, parametric studies were conducted to help understand the effects of these parameters, which include CNTs overall aspect

ratio and the size and level of hardened zones due to the Orowan effect and thermal expansion mismatch.

For all the models used in the parametric study, the RVE model's radius which is 10 nm is kept as a constant. In this way, the finite element model mesh size is the same in all the models used in the parametric study. Firstly, mesh dependency study is carried out for different minimum mesh sizes including 0.025nm, 0.056nm. it should be noted that the minimum meshes are all located in the interface area which usually has larger deformation. As shown in Figure 37, the minimum mesh size of 0.056nm presents a good convergence and this fine mesh size is used for all the models thereafter.

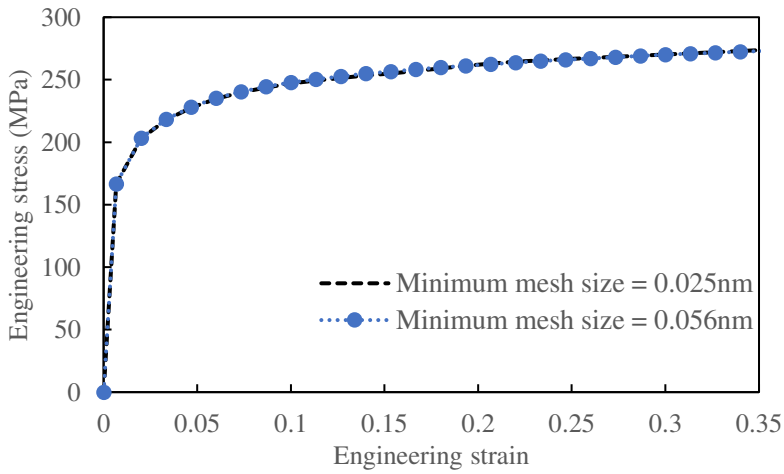

Figure 37. Convergence study of mesh size in FE simulations which shows that a minimum mesh size of 0.056nm is fine enough.

4.3.1 Effects of CNTs Aspect Ratio, Hardened Zone Volume Fraction, and Residual Plastic Strain

Experiments are performed with different weight fractions of NiCNTs which varies from 0.5% to 1%. In this part, we take the example of Al/NiCNTs with 1 wt. % of NiCNTs, and explore the effects of CNTs aspect ratio, hardened zone volume fraction, and hardened (or called residual) strain.

CNTs have extremely high aspect ratios which can vary from 1000 to even 100000 (Y. Wang, Wu, & Wei, 2003). It is also due to the high aspect ratio that there exists waviness in CNTs, which will change the equivalent aspect ratios of CNTs in RVE models. The CNTs are usually randomly oriented during manufacturing, thus the equivalent aspect ratio would be much lower than the actual aspect ratio. To find out the effect of aspect ratio on the strengthening mechanism of Al/NiCNT nano-composites, a series of parametric studies are carried out. The values selected for aspect ratios are 10, 15, 20, 30, 40, 50, 60, 70, 80 and 100.

Due to the thermal expansion mismatch and Orowan strengthening effect, there is a transitional area between NiCNTs and aluminum matrix, which plays a significant role in composites for the strengthening. However, the volume fraction and hardened area are difficult to measure directly in the experiments, so a set of parametric studies are investigated. It is assumed that the hardened aluminum follows the stress-strain curve of pure aluminum, and the level (or extent) of the hardened zone is described by the corresponding plastic strain of pure aluminum (Long et al., 2015). An example contour plot of the FE simulation result is displayed in Figure 38. It shows that the region of high strain concentration is mainly located at the interface between CNTs' tip and the matrix of the composites. Fracture initiation occurs usually from these sites.

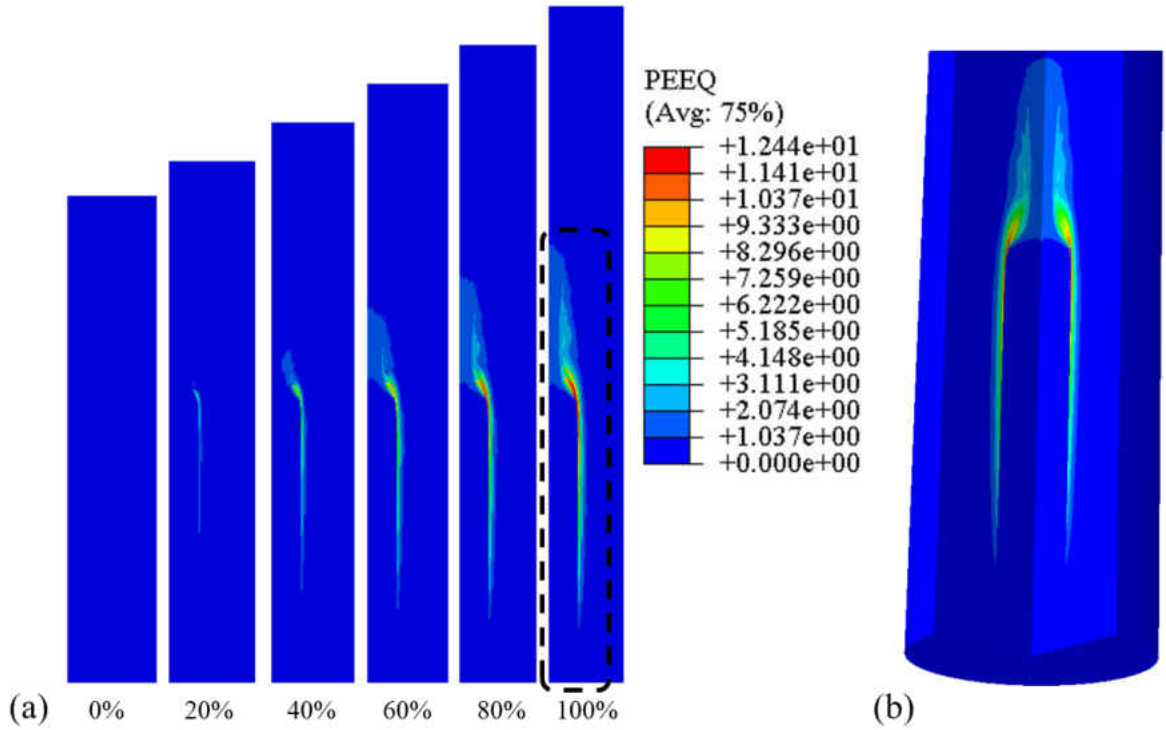

Figure 38. (a). An example result of the RVE model (axisymmetric elements) which shows the contour plot of effective plastic strain distribution at different overall tensile strains. The plastic strain which concentrates at the interface zone is an important factor of the material strengthening and fracture initiation. (b). The zoomed plastic strain contour plot at the last loading step in 3D space.

There are some key parameters describing the RVE model, which are listed in Table 13. The relationship between volume fractions (of both Ni and CNTs, f_{Ni} and f_{CNT}) and weight fraction (of Ni-coated CNTs, w) can be expressed as Eq. (28) and Eq. (29).

Table 13 Some key parameters used in RVE models

f_{CNT}	Volume fraction of CNTs
f_{Ni}	Volume fraction of nickel
ρ_{CNT}	Density of CNTs
ρ_{Ni}	Density of nickel
ρ_{Al}	Density of aluminum
w	Weight fraction of NiCNTs

$$f_{Ni} = \frac{\frac{0.815w}{\rho_{Ni}}}{\frac{0.815w}{\rho_{Ni}} + \frac{0.185w}{\rho_{CNT}} + \frac{(1-w)}{\rho_{Al}}} \tag{28}$$

$$f_{\mathrm{CNT}} = \frac{\frac{0.185w}{\rho_{CNT}}}{\frac{0.815w}{\rho_{Ni}} + \frac{0.185w}{\rho_{CNT}} + \frac{(1-w)}{\rho_{Al}}} \tag{29}$$

The values for hardened zone volume fraction are selected as 0.05, 0.1, 0.15, 0.2, 0.25, and the values of hardened plastic strain used are 0, 0.1, 0.2, 0.3, 0.4, 0.6, and 0.8. The combinations of different parameters require a total number of 10*5*7=350 FE simulations. The results of predicted initial yield stress with hardened strain and hardened zone volume fraction as variables are shown in Figure 39. The results of predicted initial yield stress with hardened strain and CNTs aspect ratio as variables are shown in Figure 40. It's shown that more hardened strain results in higher initial yield stress of nano-composites, a larger hardened volume fraction leads to higher yield stress, and a greater aspect ratio gives higher initial yield stress. Moreover, the strengthening effect of NiCNTs follows the pattern of diminishing returns as aspect ratio and residual strain get larger. There are more strengthening effects from NiCNTs as the hardened volume fraction increases.

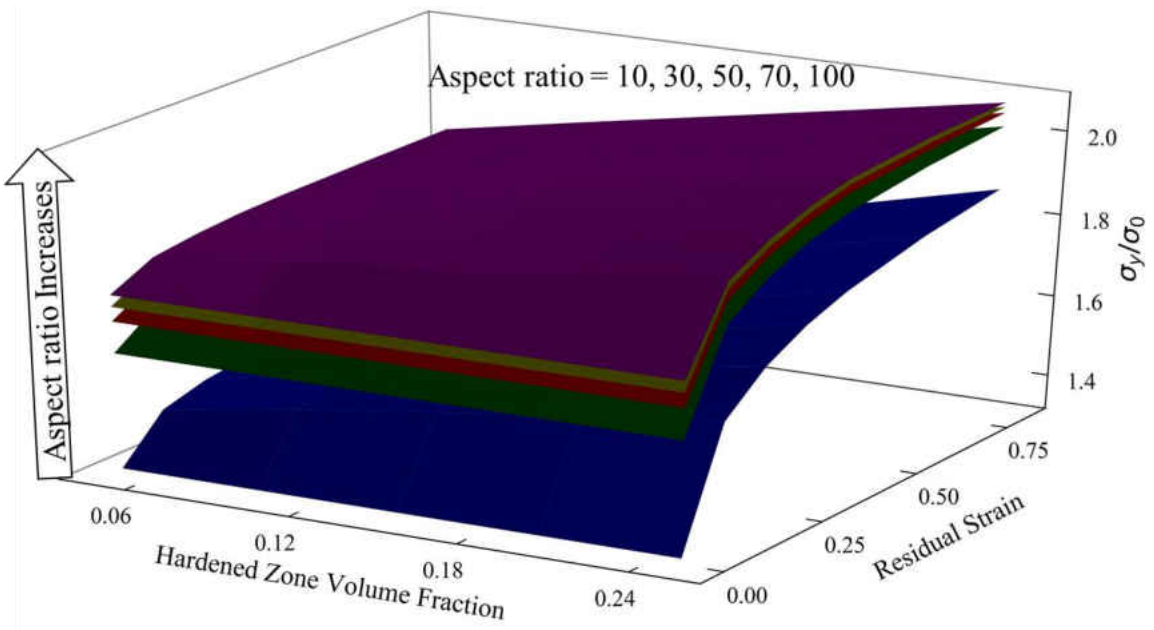

Figure 39. Simulation results of the initial yield stress of Al/NiCNTs for different aspect ratios, different volume fraction of hardened zone, and different hardened/residual plastic strain of interfacial aluminum. The z-axis is the initial yield stress of nano-composites (σ_y) normalized by the initial yield stress of pure aluminum ($\sigma_0 = 72$MPa).

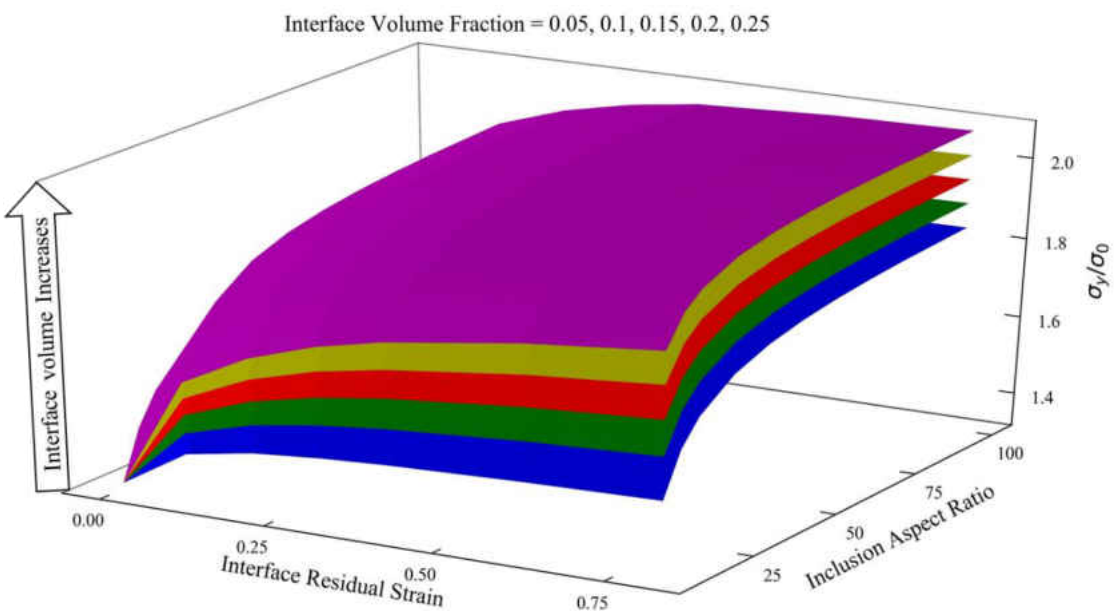

Figure 40. Simulation results of initial yield stresses of Al/NiCNTs under different aspect ratios and different hardened/residual plastic strain of interfacial aluminum. The z-axis is the initial yield stress of nano-composites (σ_y) normalized by the initial yield stress of pure aluminum ($\sigma_0 = 72$MPa).

4.3.2 Correlations between FE Simulations and Experimental Results

With different parameters of NiCNTs aspect ratio, hardened zone volume fraction and hardened plastic strain, the stress-strain curves from different tensile loading simulations of the whole model are different. Part of the engineering stress-strain curves of different models (i.e., different weight fractions of NiCNTs, different aspect ratio of NiCNTs) which are close to those in experimental data (0.5% wt. and 1.0% wt. NiCNT composites) shown in Figure 41.

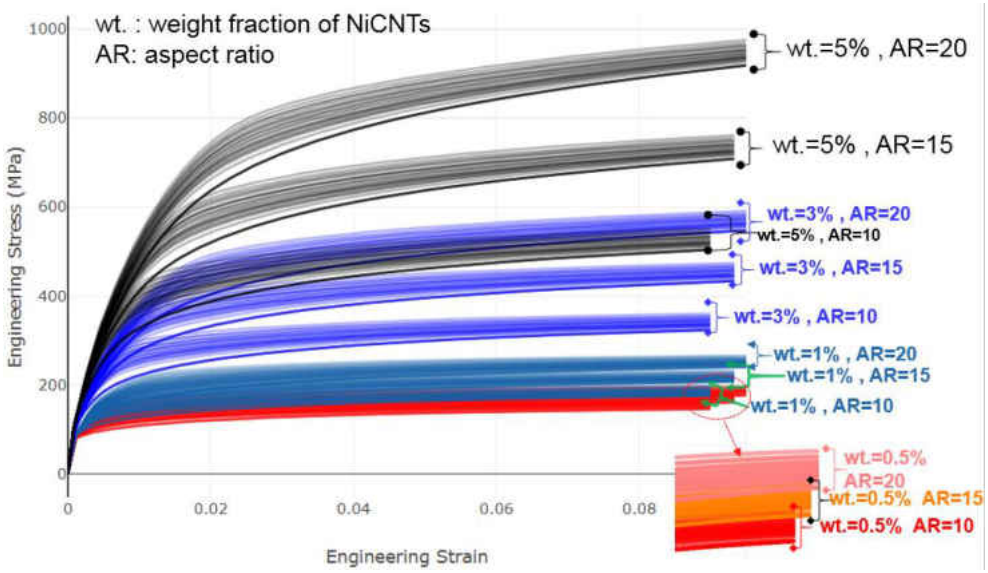

Figure 41. Engineering stress-strain curves from FE simulations, which are close to the range of experiment data (0.5% wt. and 1.0% wt. NiCNT aluminum composites).

A set of parameters giving the best curves fitting can be found using the least squares method for different experimental engineering stress-strain curves with different weight fractions of NiCNTs. They are summarized in

Table 14. The comparisons between RVE predictions and test results are plotted in Figure 42, where the simulation data are plotted with dotted lines and test data use solid curves. One can see that a very good correlation is achieved for two cases in terms of predicting the strengthening of NiCNTs to the aluminum matrix.

Table 14 The optimized best combinations of model parameters that well fit experimental data with different weight fractions of NiCNTs

Aspect ratio	Volume fraction of hardened zone	Harden strain
15	0.15	0.3

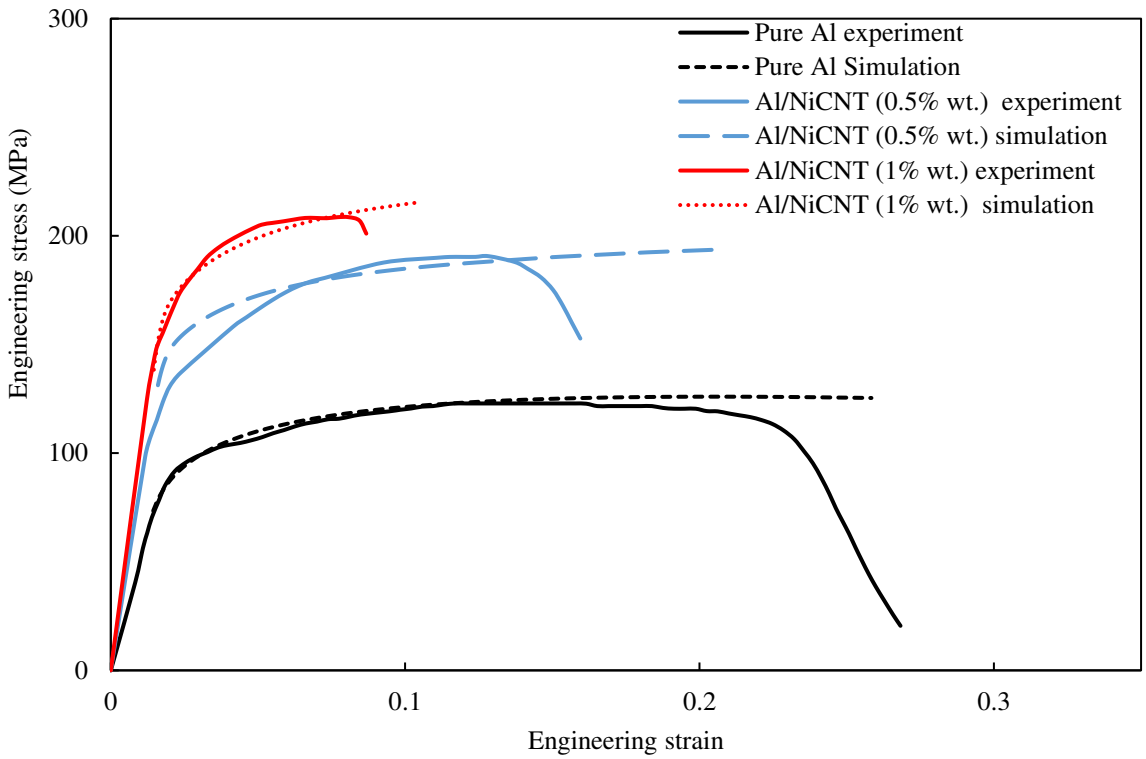

Figure 42. Comparisons between test results and FE simulations. A very good correlation is achieved.

4.4 Analytical Solutions of Strengthening Effects

George et al. (George et al., 2005) proposed that three strengthening mechanisms are very important for the strengthening of CNT/aluminum composites: thermal expansion mismatch, Orowan looping effect, and load bearing effect. Zhang et al. (Z. Zhang & Chen, 2008) found that Orowan looping played a key role in particulate-reinforced metal matrix nano-composites and that the influence of the Orowan strengthening mechanism increases as the size of nanoparticles drops. The diameters of CNTs used in this study are very small ranging from $8nm$ to $15nm$, so the

Orowan looping would be of great importance to the strengthening of Al/NiCNTs. Due to the content of nickel is extremely low, the strengthening effect of nickel is neglected in this study.

The following Eq. (30) is assumed to integrate different mechanisms for the prediction of the theoretical yield stress of composites:

$$\sigma_{yc} = \sigma_{ym}(1 + f_{load})(1 + f_{Orowan})(1 + f_{thermal}) \tag{30}$$

Here, σ_{yc} is the yield stress of Al/NiCNT composites, σ_{ym} is the yield stress of pure aluminum matrix, f_{load} is an improvement factor which contributes from the load bearing effect, f_{Orowan} is an improvement factor associated with the Orowan looping effect, and $f_{thermal}$ is an improvement factor related to the thermal expansion mismatch effect.

The influencing factor of f_{load} can be simplified as follows (Z. Zhang & Chen, 2006):

$$f_{load} = 0.5 f_v, \tag{31}$$

where f_v is the volume fraction of the inclusions (i.e. CNTs here).

The amount of strengthening effect from Orowan looping is shown below according to Ref. (Long et al., 2015):

$$f_{Orowan} = \frac{a_1 G_m b}{\sigma_{ym}} \sqrt{\frac{2 f_v}{\pi d^2}} ln\left(\frac{d}{2b}\right) \tag{32}$$

Here, G_m is the shear modulus of the matrix material, and $G_m = 26GPa$ for aluminum; b stands for Burgers vector, and $b = 0.286nm$ for aluminum; d is the diameter of CNTs, and d varies from $8nm$ to $15nm$ for CNTs used in this study.

The $f_{thermal}$ takes the form of Eq. (33) based on Ref. (Q. Li, Viereckl, Rottmair, & Singer, 2009),

$$f_{thermal} = \frac{a_2 1.25 G_m b}{\sigma_{ym}} \sqrt{\frac{4 f_v (CTE_A - CTE_C)(T_1 - T_2)}{b(1 - f_v)d}}, \tag{33}$$

where CTE_A is the thermal expansion coefficient of aluminum, and $CTE_A = 23.1 \times 10^{-6}(\frac{1}{K})$. CTE_C is the thermal expansion coefficient of CNTs, and $CTE_C = -5.6 \times 10^{-6}(\frac{1}{K})$. T_1 is the maximum operating temperature during the material fabrication process, and $T_1 = 550°C$ which is the composites' consolidation temperature. T_2 is the minimum operating temperature (room temperature), and $T_2 = 22°C$ in the present study.

Combining all three factors, the final equation for material strengthening becomes

$$\sigma_{yc} = \sigma_{ym}(\bar{\varepsilon}_{pl})(1 + 0.5 f_v)\left(1 + \frac{a_1 G_m b}{\sigma_{ym}(\bar{\varepsilon}_{pl})}\sqrt{\frac{2 f_v}{\pi d^2}}\, ln\left(\frac{d}{2b}\right)\right)\left(1 + \frac{a_2 1.25 G_m b}{\sigma_{ym}(\bar{\varepsilon}_{pl})}\sqrt{\frac{4 f_v (CTE_A - CTE_C)(T_1 - T_2)}{b(1 - f_v)d}}\right) \tag{34}$$

Here, $\sigma_{ym}(\bar{\varepsilon}_{pl})$ is the corresponding yield stress of matrix material under different plastic strain. The symbols a_1 and a_2 are free parameters that need to be calibrated, which represent the Orowan looping effect and thermal expansion mismatch effects, respectively.

The purpose of nickel addition is to improve the dispersion of CNTs in the aluminum matrix and to improve the interface between CNTs and metals. The volume fraction of the nickel is very limited. Thus, the influence of nickel on the strengthening is negligible and it is omitted in this analytical analysis.

Two sets of test data are needed to be calibrated for the strengthening equation, which are the yield stress-strain curves of Al/NiCNTs with the weight fraction of NiCNTs of 0.5% and 1.0%. The best set of parameters that fit the experimental data are selected based on the minimum error criterion as the objective function:

$$error = \sqrt{\sum(\sigma_i^{test} - \sigma_i^{analytical})^2}, \quad where\ i = 0.5\%, 1\% \tag{35}$$

A Python script is written to find the minimum error value, and a set of parameters are finally discovered: $a_1 = 0.110$, $a_2 = 0.0758$ .The comparison between analytical solutions and experimental data are plotted in Figure 43. A very good correlation is achieved for the analytical solution. It should be noted that the stress values of the analytical solution are higher than that from the experimental results right before the places where the specimens were fractured. This is mainly caused by the fact that the analytical solution doesn't consider the influence of specimen fracture. In the future, specimen fracture will be considered.

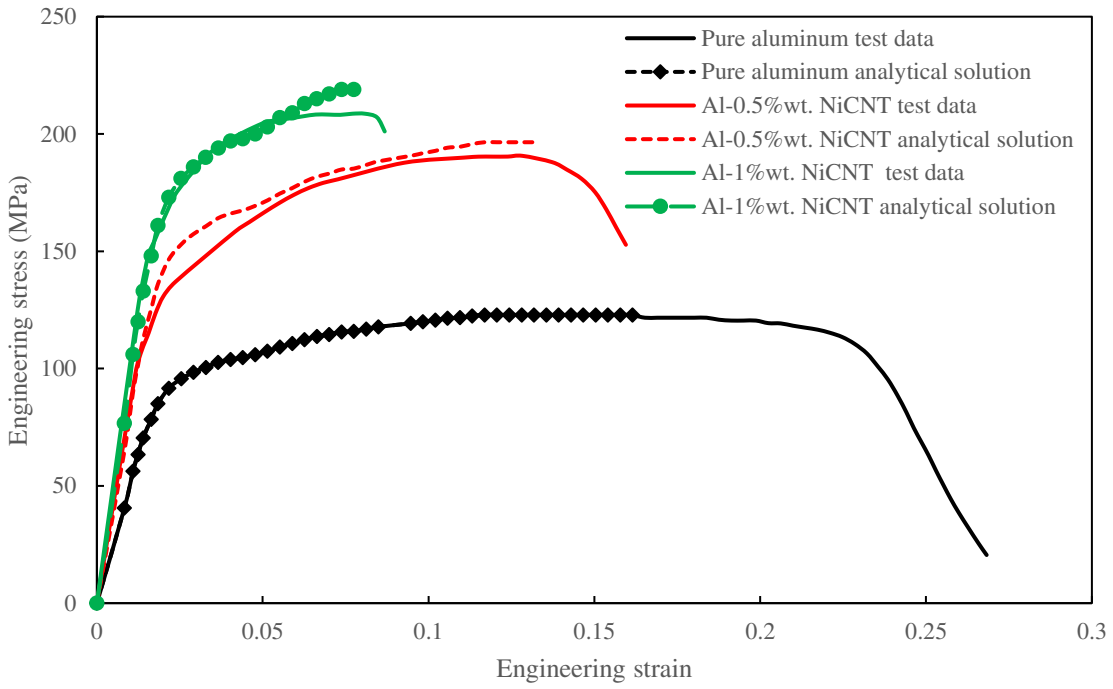

Figure 43. Comparisons between experiments and analytical solutions. A very good correlation was achieved.

Based on the results from the analytical solution, the different effects of each strengthening factors on different CNT reinforced aluminum composites are summarized in Figure 44. The figure shows that the weighting factors of different strengthening factors change with the change of CNT volume fractions. Moreover, the Orowan strengthening effect always plays the most important role in the strengthening of this type of composites, and its weighting factor increases with a larger weight fraction of NiCNTs. At last, Figure 45 presents the effect of CNT diameter on the strengthening of CNT reinforced composites. The smaller diameter of CNTs always leads to the greater strength of corresponding composites.

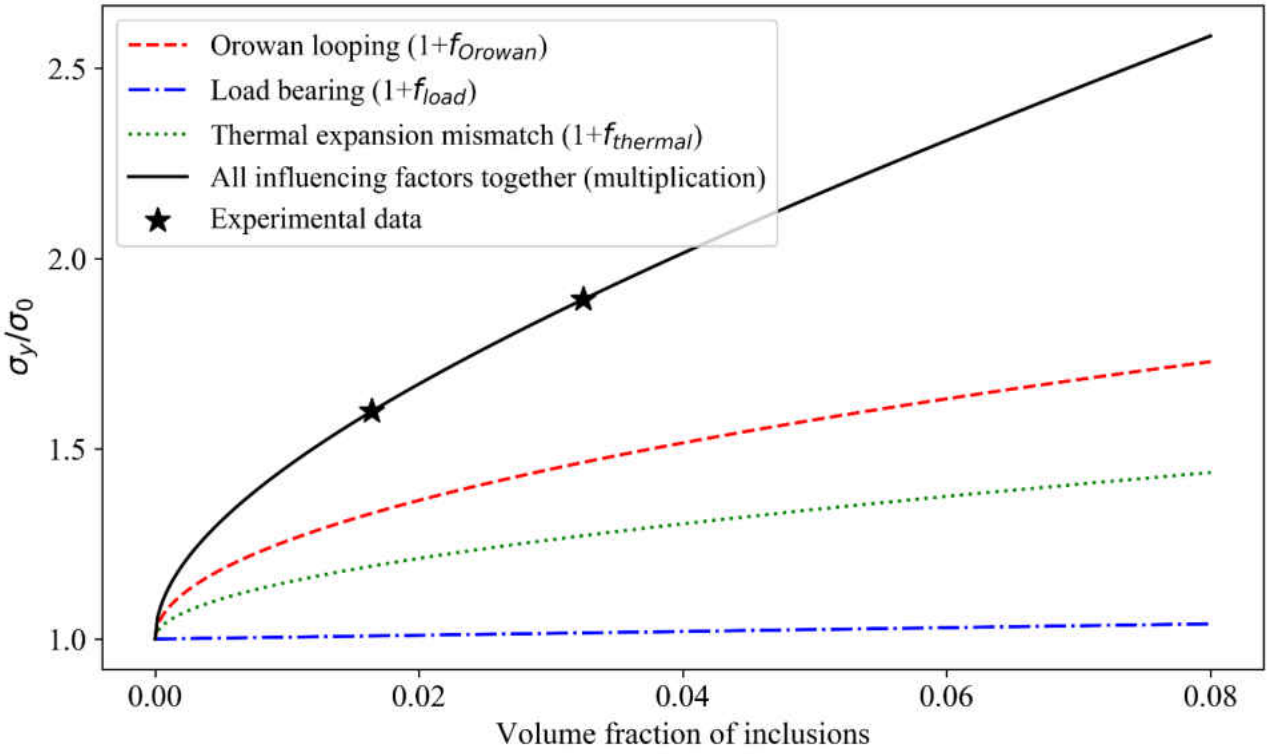

Figure 44. The effect of different influencing factors on CNT reinforced aluminum matrix based on Eq. (34). Orowan looping is the most important among the three strengthening factors.

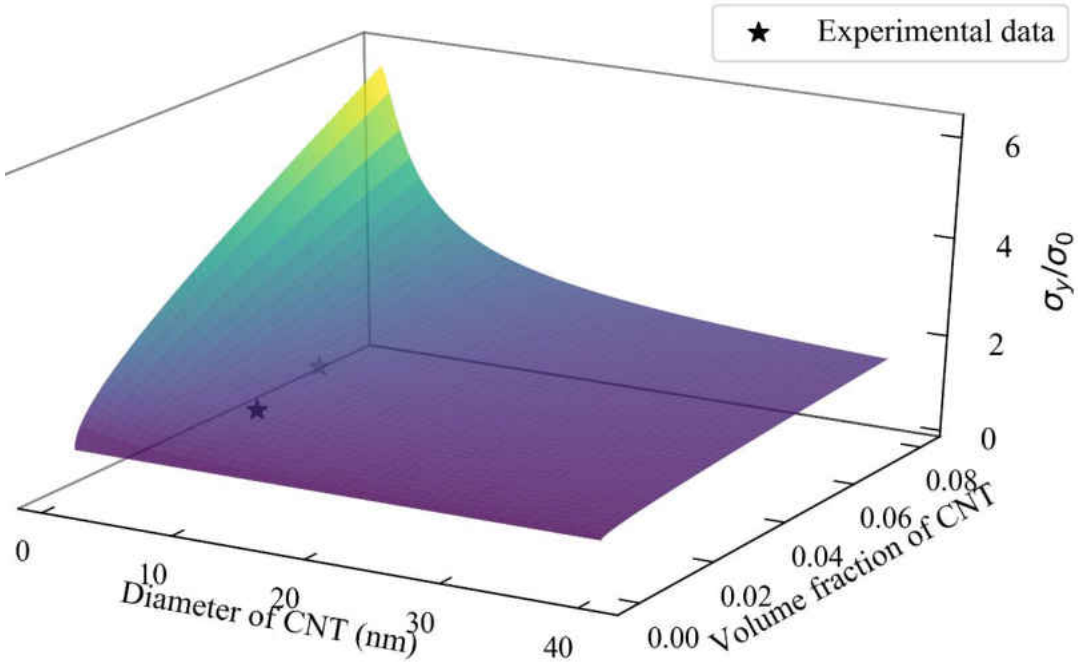

Figure 45. Influence of CNT diameter on the strengthening effect of aluminum composites based on the analytical solution. It shows that smaller diameter can greatly enhance the strength of CNT reinforced aluminum composites

CHAPTER 5 DIGITAL WORKFLOW OF 3D RVE MODEL

The aim of this chapter is to develop a digital workflow which is built in Abaqus to automatically generate 3D models of composites with cylindrical inclusions, where the inclusions can be randomly generated in the 3D space. The innovation of this work is that this tool firstly takes the influence of the interface between the matrix and inclusions into consideration. Secondly, the anisotropic properties of inclusions are also considered which can provide more accurate predictions for the effective material properties of composites.

5.1 Methodology

This section introduces the methodology and procedures to create the RVE models. The key step here is to introduce inclusions into the matrix while making sure that no intersections happen among inclusions. Another important feature is to set up local coordinate systems for inclusions. The basic workflow for creating the composite model is shown in Figure 46. Once a volume fraction and dimensions of inclusions are selected, the dimensions of the matrix are designated, and the thickness of the interface (for mechanical analysis) can be assigned. The total number of inclusions will be calculated based on these data. Then the inclusions will be generated one by one.

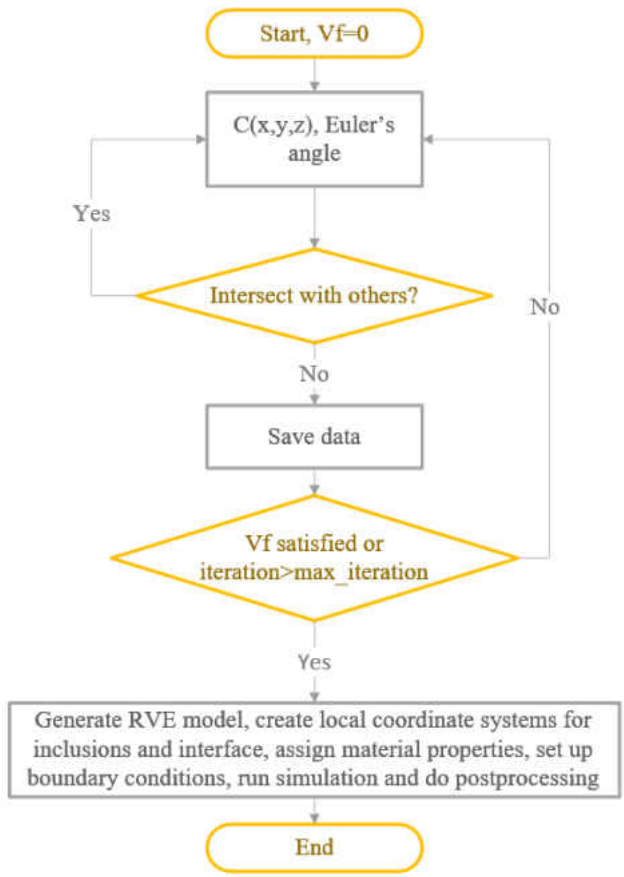

Figure 46. 3D RVE modeling procedures. V_f represents the designated volume fraction of inclusions; C(x,y,z) is the randomly generated inclusion location in the 3D space.

Random sequential adsorption (RSA) algorithm has been widely used in the literature (Evans, 1993; Sreedhar Kari, Berger, Rodriguez-Ramos, & Gabbert, 2007; Melro, Camanho, & Pinho, 2008), and it is employed to introduce new inclusions into the matrix, and separating axis theorem is used for interference checking among inclusions which follows Dan's work (Sunday). The distance between two geometries is defined as the minimum distance of any two points on these two geometries. For two geometries G_1 and G_2, the distance of these two sets can be calculated as:

$$d(G_1, G_2) = min(d(P, Q)), \qquad P \in G_1, Q \in G_2 \tag{36}$$

where P is any point in geometry G_1, Q is any point in geometry G_2.

Only cylindrical inclusion is considered in this study, and cylindrical geometry can be represented by the axis of the geometry and its radius. Specifically, the distance of two cylindrical geometries can be calculated by calculating the distance of the two corresponding axes:

$$d(G_1, G_2) = d(L_1, L_2) - R_1 - R_2 \tag{37}$$

where L_1 is the axis of cylindrical geometry G_1, R_1 is the radius of cylindrical geometry G_1, L_2 is the axis of cylindrical geometry G_2, R_2 is the radius of cylindrical geometry G_2, $d(L_1, L_2)$ is the distance of two axes (L_1 & L_2).

Assume P_0 and P_1 are the two endpoints of axis L_1, Q_0 and Q_1 are the two endpoints of axis L_2. The two segments are represented as:

$$L_1: P(s) = P_0 + s(P_1 - P_0) = P_0 + s\boldsymbol{u}, \quad where\ 0 \le s \le 1 \tag{38}$$

$$L_2: Q(t) = Q_0 + t(Q_1 - Q_0) = Q_0 + t\boldsymbol{v}, \quad where\ 0 \le t \le 1 \tag{39}$$

Assume $\boldsymbol{w}(s,t) = P(s) - Q(t)$ is a vector between any two points on the two segments, and finding the minimum value of $\boldsymbol{w}(s,t)$ can lead to the minimum distance between the two segments. So finding the minimum value of $\boldsymbol{w}(s,t)$ for all s and t is our objective. Let $P_C = P(s_C)$ and $Q_C = Q(t_C)$ be two the unique points where the two segments would be the closest, thus $\boldsymbol{w}(s_C, t_C)$ would be the minimum for all $\boldsymbol{w}(s,t)$. If the two segments do not intersect with each other, the segment $P_C Q_C$ is perpendicular to both segments, and this leads to equations:

$$\boldsymbol{u} \cdot \boldsymbol{w}_C = 0 \tag{40}$$

$$\boldsymbol{v} \cdot \boldsymbol{w}_C = 0 \tag{41}$$

These two equations can be solved by substituting all the values of $\boldsymbol{u}, \boldsymbol{v}, \boldsymbol{w}_C$, and let $a = \boldsymbol{u} \cdot \boldsymbol{u}$, $b = \boldsymbol{u} \cdot \boldsymbol{v}$, $c = \boldsymbol{v} \cdot \boldsymbol{v}$, $d = \boldsymbol{u} \cdot (P_0 - Q_0)$, and $e = \boldsymbol{v} \cdot (P_0 - Q_0)$. We get the values for s_C, t_C:

$$s_C = \frac{be - cd}{ac - d^2} \; and \; t_C = \frac{ae - bd}{ac - d^2} \tag{42}$$

If $ac - d^2 = 0$, the two segments are parallel and the distance between the two segments is constant. If two segments are parallel, we can fix the value of one parameter, and the distance can be solved.

Note that the objective of the minimum value of $\boldsymbol{w}$ is the same as the minimum value of $|\boldsymbol{w}|^2 = \boldsymbol{w} \cdot \boldsymbol{w} = (P_0 - Q_0 + s\boldsymbol{u} - t\boldsymbol{v}) \cdot (P_0 - Q_0 + s\boldsymbol{u} - t\boldsymbol{v})$ which is a quadratic function of s and t, and $|\boldsymbol{w}|^2$ has the minimum value at $C = (s_C, t_C)$. This means that the value of $|\boldsymbol{w}|^2$ would increase starting from $C = (s_C, t_C)$.

As stated above, $0 \leq s \leq 1$ and $0 \leq t \leq 1$ are necessary for the two segments. So if any of the values of s_C and t_C lies outside of the range, the new minimum value of $\boldsymbol{w}(s, t)$ has to be determined.

There are several conditions that need to be considered. If $s < 0$, the minimum value of $|\boldsymbol{w}|^2$ would occur at $s = 0$. Under this circumstance, $|\boldsymbol{w}|^2 = (P_0 - Q_0 - t\boldsymbol{v}) \cdot (P_0 - Q_0 - t\boldsymbol{v})$. The minimum value can be obtained by taking the derivative with t:

$$0 = \frac{d}{dt}|\boldsymbol{w}|^2 = -2\boldsymbol{v} \cdot (P_0 - Q_0 - t\boldsymbol{v}). \tag{43}$$

And this can give the minimum value at $(0, t_0)$ where $t_0 = \frac{\boldsymbol{v} \cdot w_0}{\boldsymbol{v} \cdot \boldsymbol{v}}$.

Minimum distances between two segments from other special conditions can also be solved by this method. Let segment L_1 be the centerline of cylinder CYL_1, and r_1 be the radius of cylinder CYL_1. Let segment L_2 be the centerline of cylinder CYL_2, and r_2 be the radius of cylinder CYL_2. If the minimum distance between the two segments is greater than $(r_1 + r_2)$, there is not interference between two cylinders.

The key steps of the modeling procedure are summarized below. First, a cuboid is generated based on the dimensions of the matrix. Then a set of coordinates (u_1, u_2, u_3) and a set of Euler angles (α, β, γ) are randomly generated within Python for the newly proposed inclusion. In the beginning, the elementary inclusion is always assumed to be located at the origin of the global coordinate system with the height (axis) direction aligned in the z-axis (which means the inclusion local coordinate system coincides with the global coordinate system). The definitions of coordinates and angles are listed below.

- u_1 is in the range of matrix width (x-axis)
- u_2 is in the range of matrix thickness (y-axis)
- u_3 is in the range of matrix height (z-axis)
- α is the rotation angle of the inclusion by local coordinate system x-axis in the counterclockwise direction, and its range is in $[0, 2\pi)$.
- β is the rotation angle of the inclusion by local coordinate system y-axis in the counterclockwise direction, and its range is in $[0, \pi)$.
- γ is the rotation angle of the inclusion by local coordinate system z-axis in the counterclockwise direction, and its range is in $[0, 2\pi)$.

If a newly proposed inclusion is not totally inside the matrix, the outside part of the proposed inclusion will be copied to the opposite surface. Before moving the inclusions to designated locations, the interference check will be carried out for all these parts which originate from one inclusion. For example, as shown in Figure 47, cylinder A is positioned inside the matrix, then cylinder B_1 is randomly generated which has no interference with cylinder A. Moreover, part of cylinder B_1 is outside the matrix, so a copy of cylinder B_1 is created and named as cylinder B_2. Then cylinder B_2 is moved to the left by the distance of matrix width, and the outside parts of these cylinders are then trimmed. If there is any intersection, the creation of the newly proposed inclusion(s) will be aborted; if there is not any intersection, the information of new inclusion(s) like dimensions (radius, height), coordinates (u_1, u_2, u_3) and Euler angles (α, β, γ) will be saved.

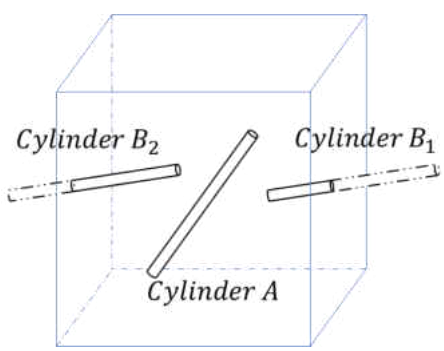

Figure 47. A diagrammatic sketch to show the arrangement of inclusions intersecting with RVE boundary planes.

The process of creating inclusions will continue until the designed volume fraction of inclusions is met. After that, the geometries of all the inclusions are built based on their dimensions and spatial information. The geometries of all the interfaces will also be created in the same way given the inclusions' dimensions, spatial information, and interfaces' thickness. After these operations, the inclusions and interfaces will be in the designated positions in the 3D space.

Currently, the matrix is still an intact cuboid. Once geometries of the inclusions and interfaces are ready, the cuboid will be cut by all the inclusions and interfaces by Boolean operation 'NOT', which is provided by Abaqus/CAE.

After that, the cut cuboid will be assigned as the material properties of the matrix, the geometries of inclusions will be assigned as the material properties of inclusions and the geometries of interfaces will be assigned as the material properties of interfaces. Anisotropic properties definition (including orthotropy and transversely isotropy) for inclusions are available if anisotropic properties are provided before starting this plug-in.

One of the most frequently used material property definitions for cylindrical inclusions like carbon nanotubes or carbon fibers is transversely isotropic property. When inclusions are assigned transversely isotropic properties: the property along the cylinder height (axis) direction is different from that along the cylinder radial directions. An example is shown in Figure 48. Figure 48(a) displays an RVE model with local coordinate systems, where a local coordinate system is set up for each inclusion, which is based on each inclusion's locations and Euler angles. For each local coordinate system, the z-axis represents the axis direction of each inclusion.

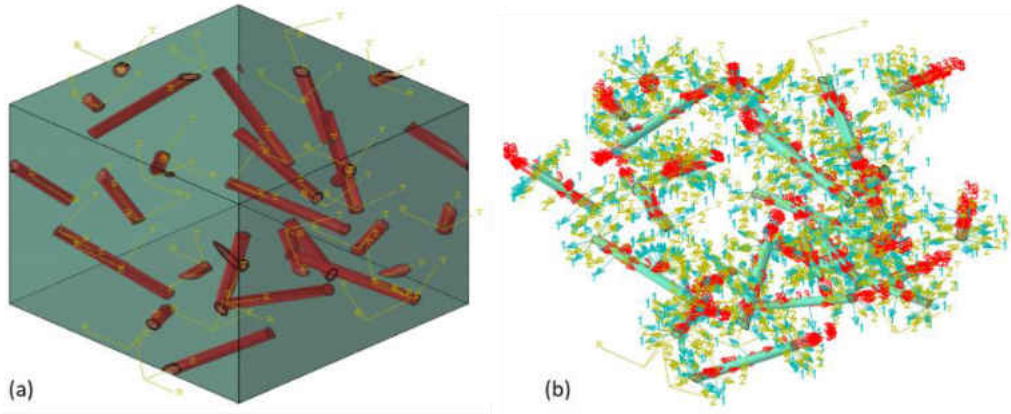

Figure 48. An example of the RVE model with transversely isotropic properties of inclusions. (a) represents an RVE model with local coordinate systems that are created for inclusions; (b) shows the orientations of material properties of inclusions.

At this point, two different modeling options are available for the matrix-inclusion interface. One is contact pair, and the other one is node sharing. If a thermal analysis with interfacial thermal resistance is going to be carried out, contact pairs will be generated for matrix and interfaces, and for interfaces and inclusions. The sharing node method is deployed for other cases, for example, mechanical analysis, and thermal analysis without considering interfacial thermal resistance. For such cases, another Boolean operation 'AND' is going to be carried out for all of the inclusions, interfaces, and the matrix, but the faces between matrix and interfaces and between interfaces and inclusions will be kept. All of those parts would form a new part with different material properties. An RVE model example is displayed in Figure 49. After this procedure, the model is ready for meshing, defining boundary conditions, and applying loading conditions.

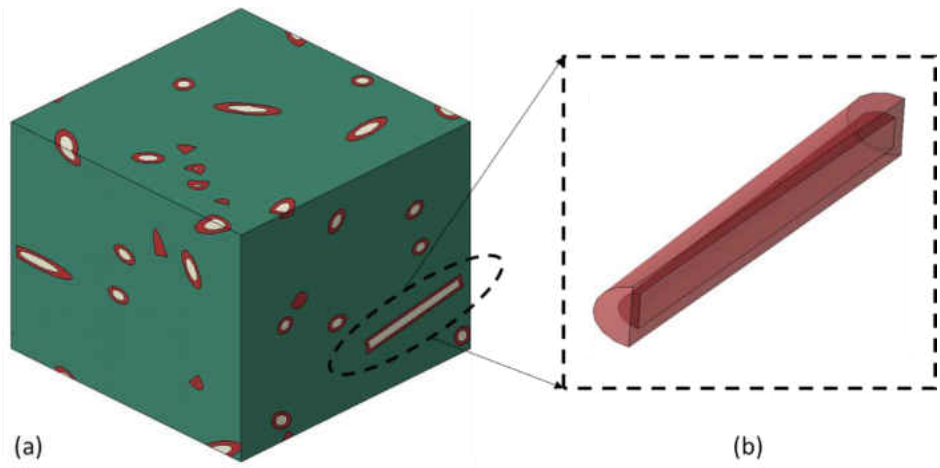

Figure 49. (a) An RVE model with different material properties which are represented by different colors. Shared faces are formed between the matrix and all interfaces and between all interfaces and all inclusions to generate shared nodes in the meshing period. (b) A zoom-in view between an inclusion and an interface.

Hill (Hill, 1963) defined the RVE as a sample that contains a large number of inclusions that the apparent overall properties of the composites are independent of the boundary conditions. Kinds of literature have shown that, though the apparent results fluctuate from one boundary to another, the apparent results would converge with the increase of the inclusion quantity (El Moumen, Kanit, Imad, & El Minor, 2015; Kanit, Forest, Galliet, Mounoury, & Jeulin, 2003; Saoudi et al., 2020). Cho et al. (Cho, Lee, & Park, 2015) also showed that with the increase of RVE size, the effect of the boundary conditions become negligible. Kassem (Kassem, 2009) presented that for cylindrical inclusion reinforced composites, the results from homogenous boundary condition and Mori-Tanaka analytical method give very similar results when the volume fraction of inclusions is below 10%. Moreover, the homogenous boundary condition provides better computational efficiency in simulation than other types of boundary conditions. The periodic boundary condition requires a large number of constraints for the periodicity setting. The 3D finite element simulation with large number of elements makes the computational efficiency difference bigger. It should also be noted that for the composites with randomly oriented cylindrical inclusions in the 3D space, like carbon nanotube reinforced composites, the volume fraction of inclusions is usually below 10%.

Considering this situation and for the balance of both accuracy and computational efficiency, a homogenous boundary condition is chosen in this work. An example of homogenous boundary conditions and loadings setting for RVE can be found in Long's method (Long et al., 2015). For instance, Figure 50 shows a simplified model. Surface L, which is at x=0 and whose normal direction is along the x-axis, is constrained by x-symmetric, and surface Bk, which is at y=0 and whose normal direction is along the y-axis, is constrained by y-symmetric. Similarly, surface Bm is constrained by z-symmetric. For two side surfaces (R & F), the element nodes, which are on the same surface, are set to have the same displacement on the normal direction of each corresponding surface. All the nodes in surface T have the same displacement along z axis which is the prescribed external loading. These surfaces' constrain boundary settings can be achieved by the linear constraint equations within Abaqus.

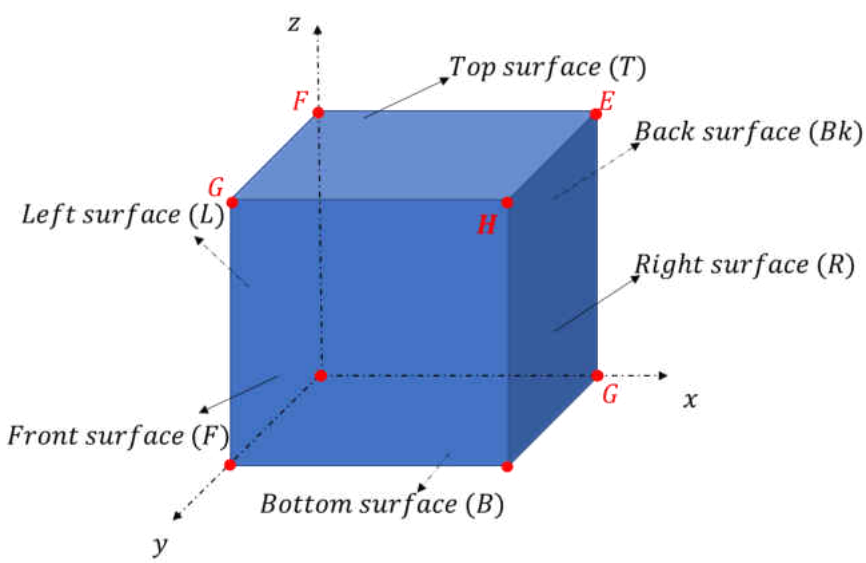

Figure 50. A diagrammatic sketch of the RVE model for the demonstration of boundary conditions. The bottom, left, and back surfaces are assumed to be symmetric. The finite element nodes on the other three surfaces (Front F, Right R, and Top T) are constrained to have the same displacement along the normal directions of the corresponding surface.

When a thermal analysis is carried out, prescribed constant temperature is assigned to the top and bottom surfaces (T and B) of the composite, while the other four side surfaces (L, R, F, Bk) can be assumed to be adiabatic.

5.2 Toolbox Interface

5.2.1 Preprocessing Phase for Model Setup

Python language is used by Abaqus as the Abaqus scripting interface, and it is a very flexible language and easy to learn (Systèmes, 2008). Python scripting in Abaqus can replace tedious actions that are performed within the graphical user interface of Abaqus/CAE. The whole simulation process for this RVE toolbox can be accomplished by Python in Abaqus, and just several mouse clicking operations are enough for the modeling procedures. There are mainly two sections in this plug-in: the mechanical analysis part which is shown in Figure 51 and the heat transfer analysis part which is shown in Figure 53**.** The plug-in can be accessed from Abaqus/CAE menu bar, by clicking the tab *Plug-ins*, then clicking the plug-in *3D RVE Toolbox*.

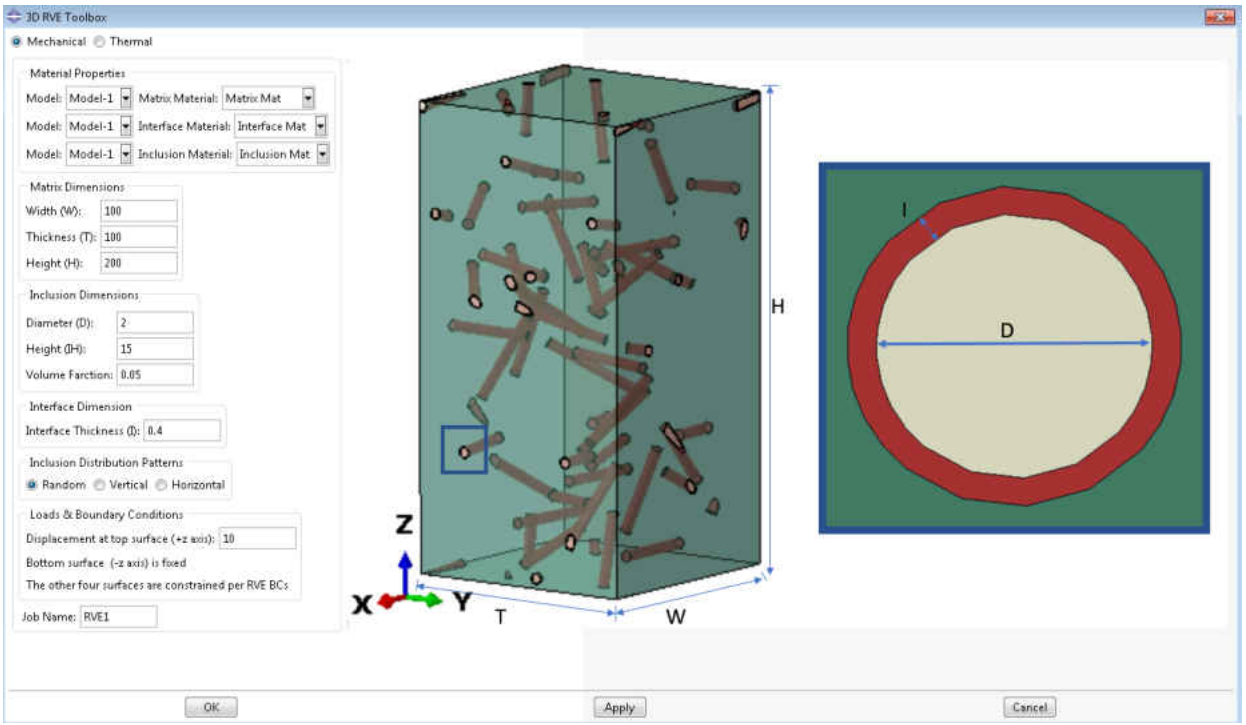

Figure 51. The interface of the *3D RVE Toolbox* plug-in for mechanical analysis. This plug-in considers the influence of interface. The interface plays an important role in metal matrix composites due to, for example, the thermal mismatch strengthening (George et al., 2005)

Within the mechanical interface, the material properties of matrix, inclusion, and interface, matrix dimensions, inclusion dimensions, and interface dimension can be assigned. Three different distribution patterns for inclusions are provided: random distribution, vertical distribution, and horizontal distribution. The detailed explanation of distribution patterns is shown later. Once the displacement and job name are assigned, the simulation will be carried out.

The inclusions are assumed to be covered by interfaces uniformly. So the interface is a hollow cylinder (or part of a hollow cylinder). Set the diameter and height of inclusion as D and H, respectively, and set the interface thickness as I, then the diameter and height of the hollow cylinder (interface) is $D + 2I$ and $H + 2I$. Moreover, though there won't be any intersections among inclusions, there can be interference among different interfaces which is a more accurate proximation to the realistic situation.

The sharing node method between interface and matrix and between interface and inclusions is employed for mechanical analysis and this can save much simulation time.

For thermal analysis, considering interfacial thermal resistance, contacts between matrix and inclusions are used. If interfacial thermal resistance is not considered, the sharing node method is employed.

It should be noted that material properties should be created before this plug-in, otherwise, the default material properties will be used for the simulation. Another option is to leave the "Job Name" from the plug-in as blank, then the model will be generated but the simulation will not start. Figure 52 shows the distribution patterns of inclusions. If inclusions' height direction is the same as the displacement direction, the inclusions are arranged by vertical alignment. If the inclusions' height direction is perpendicular to the model displacement direction, the inclusions are horizontally aligned. Otherwise, the inclusions are randomly distributed. These distribution options can help study the influence of distribution patterns on the properties of the composites.

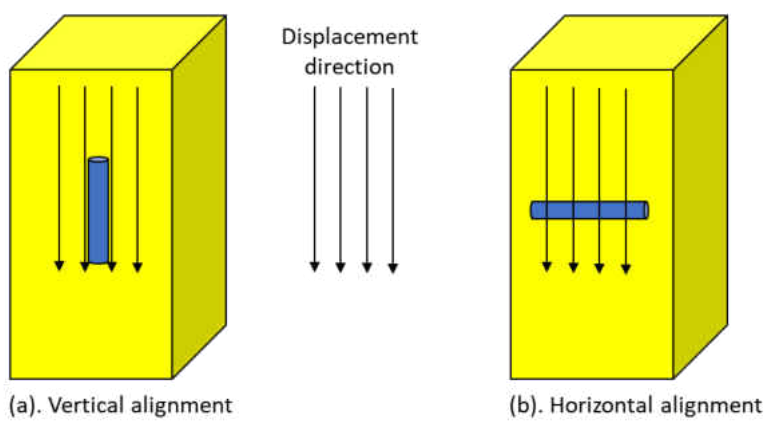

Figure 52. A diagrammatic sketch of inclusions' distribution patterns. (a) The inclusions are assumed to be vertically aligned if all the inclusions' height direction is the same as the model displacement direction. (b) the inclusions are horizontally aligned if all the inclusions' height direction is perpendicular to the displacement direction.

The thermal analysis interface basically follows the same design methodology as mechanical analysis. One key difference is that interfacial thermal resistance is implemented here for thermal analysis. General contact is employed if interfacial thermal resistance is to be studied, otherwise, the sharing node method is used among different parts (matrix, inclusions, and interface) to reduce computational time.

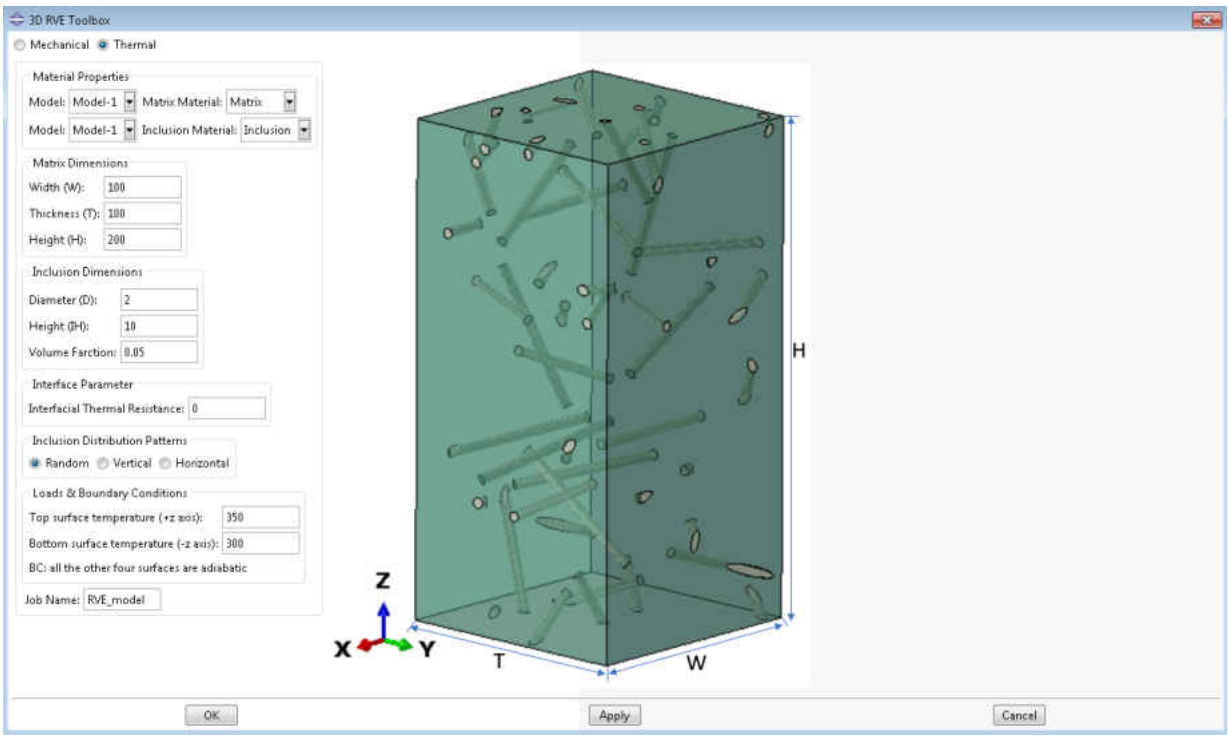

Figure 53. The interface of the 3D RVE Toolbox plug-in for heat transfer analysis. Besides random generation for the inclusions, the inclusions can also be generated via certain patterns, like all inclusions are horizontally aligned vertically aligned with the help of this plug-in.

By default, tetrahedral elements are employed for the meshing of both mechanical analysis (C3D4 element) and thermal analysis (DC3D4 element). The static solver of Abaqus is implemented for all the computational analysis.

5.2.2 Postprocessing Phase of Simulations

During the preprocessing of simulations, important data such as RVE dimensions, different surface node sets are created and stored. During the simulations, essential data like corner nodes' coordinates and nodal force on the top surface (T , Figure 50) are stored at each simulation step. If the simulation starts within the Abaqus plug-in, the postprocessing would be started automatically.

For mechanical analysis, the reaction force along the z-axis can be calculated by summarizing all the nodal forces F at the top surface (refer to Figure 50). The top surface area (S) can be calculated via the nodal location of point E and point G. And the true stress along the z-axis can be calculated as:

$$\sigma_z = \frac{F_z}{S_z} \tag{44}$$

Similarly, the true strain along the z-axis can be calculated by

$$\varepsilon_z = \ln\left(\frac{L_z + u_z}{L_z}\right) \tag{45}$$

where L_z is the initial height of the composites along the z-axis, and u_z is the displacement of the top surface.

Then the effective stress-strain relationship along the z-axis can be achieved by combining σ_z and ε_z. The Young's modulus in the z-direction can be determined by the initial values of σ_z and ε_z, and plastic property can also be measured after the elastic range of the composite materials. Similar data in other directions can also be achieved by the same method.

For thermal analysis of heat conduction, the effective thermal conductivity of composites is calculated by Fourier's law:

$$q = -kA\frac{\Delta T}{\Delta z} \tag{46}$$

where A is the cross-section area of the model, and the top surface (refer to Figure 50) is used here for the calculation. q is the rate of heat flow through a transverse cross-section area, and this rate of heat flow can be calculated by summing up the heat flux of all the nodes at the top surface. k is the effective thermal conductivity of the material, ΔT stands for the temperature difference between the top and bottom surfaces, and Δz is the distance between the top and bottom surfaces.

5.3 Application Examples

5.3.1 Influence of Anisotropy and Interface on Elasticity

The mechanical properties of carbon nanotube reinforced epoxy composites are studied to show the capability of this tool. Maghsoudlou et al. (Maghsoudlou, Barbaz Isfahani, Saber-Samandari, & Sadighi, 2019) showed the strengthening effect of CNTs on the epoxy matrix. According to Maghsoudlou et al., the average Young's modulus of epoxy is 2723.71 MPa, the Poisson's ratio is 0.4, and the density is $1200kg/m^3$.

The elastic property of CNT along height direction is taken as 1TPa which has been widely proved and accepted in the literature (Hernández-Pérez & Avilés, 2010; Seidel & Lagoudas, 2006; Thostenson, Ren, & Chou, 2001; Tserpes & Chanteli, 2013), and the elastic property along the radial direction and circumferential direction is 30GPa (Palaci et al., 2005).

The mechanical properties of the interface are very difficult to acquire from experiments (Zhu & Narh, 2004), so the properties like Young's modulus, Poisson's ratio, and density are predicted via Maghsoudlou's method: The Young's modulus of the interface is a variable which is influenced by property of matrix, the property of inclusions and the manufacturing process, and Young's modulus is obtained as 142.25GPa; The density and Poisson's ratio of the interface are calculated as the average of matrix and inclusions (Maghsoudlou et al., 2019; Saber - Samandari & Afaghi - Khatibi, 2007).

A study by Tserpes et al. (Tserpes & Chanteli, 2013) showed the aspect ratios of inclusions have a positive influence on the effective properties of composites. When the aspect ratio is over 20, the strengthening effect almost diminishes for different cases with different volume fractions of inclusions. On the other hand, though the aspect ratio of CNTs can be as high as several hundred (X. Li et al., 2012), the CNTs have lots of curvatures, and the effective aspect ratio is way lower than that number. So the choice of value 20 for the aspect ratio is reasonable and it is selected for the following analysis.

With 0.3 wt% CNTs, the effective Young's modulus of CNTs reinforced epoxy composites is 3125.43 MPa. The corresponding volume fraction of CNT can be calculated by the equation below given the densities of CNT and epoxy.

$$V_{inc} = \frac{\frac{m_{inc}}{\rho_{inc}}}{\frac{m_{inc}}{\rho_{inc}} + \frac{m_m}{\rho_m}} \tag{47}$$

where m_{inc} is the mass fraction of inclusion, ρ_{inc} is the density of inclusion, m_m is the mass fraction of the matrix, and ρ_m is the density of the matrix.

So for the 0.3 wt% CNTs reinforced epoxy composites, $m_{inc} = 0.003$, $m_m = 0.997$, $\rho_{inc} = 150kg/m^3$ (Song et al., 2020; D. J. Yang et al., 2002), $\rho_m = 1200kg/m^3$ the corresponding volume fraction is:

$$V_{inc} = \frac{\frac{m_{inc}}{\rho_{inc}}}{\frac{m_{inc}}{\rho_{inc}} + \frac{m_m}{\rho_m}} = \frac{\frac{0.003}{150}}{\frac{0.003}{150} + \frac{0.997}{1200}} = 2.351\% \tag{48}$$

For each result presented, five simulations are always carried out, and the calculated average value is used. The imposed boundary conditions for all the simulations in this work are listed in Table 15.

Table 15. 3D model boundary condition information

Surface	Surface index	Boundary condition
left	L	fixed at 1,5,6
bottom	B	fixed at 3,4,5
back	Bk	fixed at 2,4,6
right	R	fixed at 5,6 and global linear equation at 1
front	F	fixed at 4,6 and global linear equation at 2
top	T	velocity boundary
		note: the number in this column represent the degree of freedom

The rest of this section presents the FEA verification and result discussion. First of all, a verification study is presented to show that the FEA model can correctly reflect the material properties. The modeling and simulation processes follow the same procedures as stated in the previous section, and the only difference is that the material properties for inclusions, interface, and matrix are all the same.

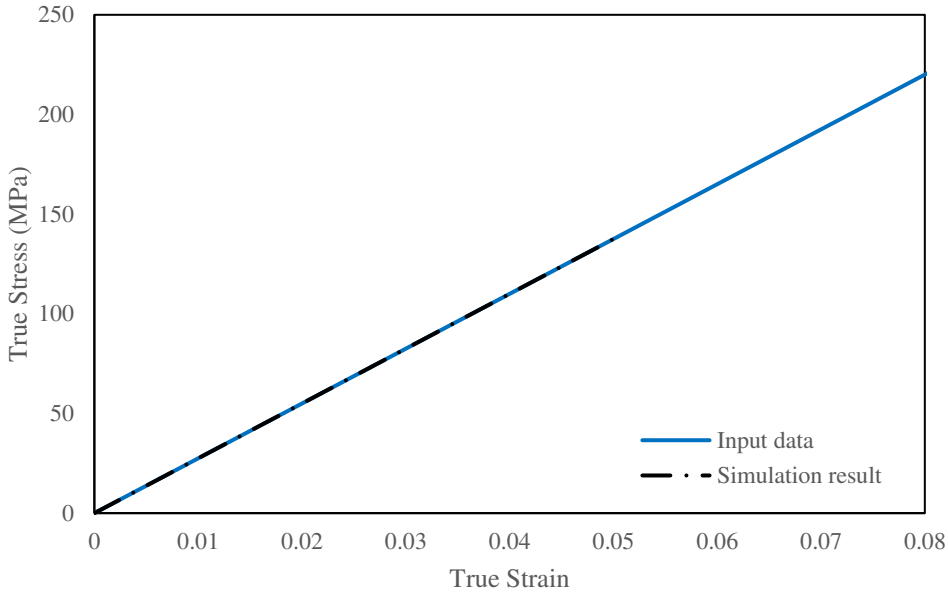

Figure 54 The comparison between FEA simulation results and input stress-strain data. It shows a perfect fit between these two sets of data which verifies the FEA model.

Figure 54 shows the strain stress data from the simulation results of the RVE model which perfectly matches the elastic modulus of the material. This proves the accuracy of this RVE modeling method and further simulations are carried out with the same procedures. Figure 55 exhibits the contour plot of local logarithmic strains of CNT reinforced epoxy composites and it shows that the large local strains all appear around the CNTs. Four different types of RVE models are generated and investigated. For the elastic modulus of CNTs, two scenarios are considered: the elastic modulus of CNTs is isotropic or anisotropic. Another influencing factor considered here is the interface: there is (or is not) interface between the inclusions and matrix. The results of different combinations for the influencing factors are shown in Table 16.

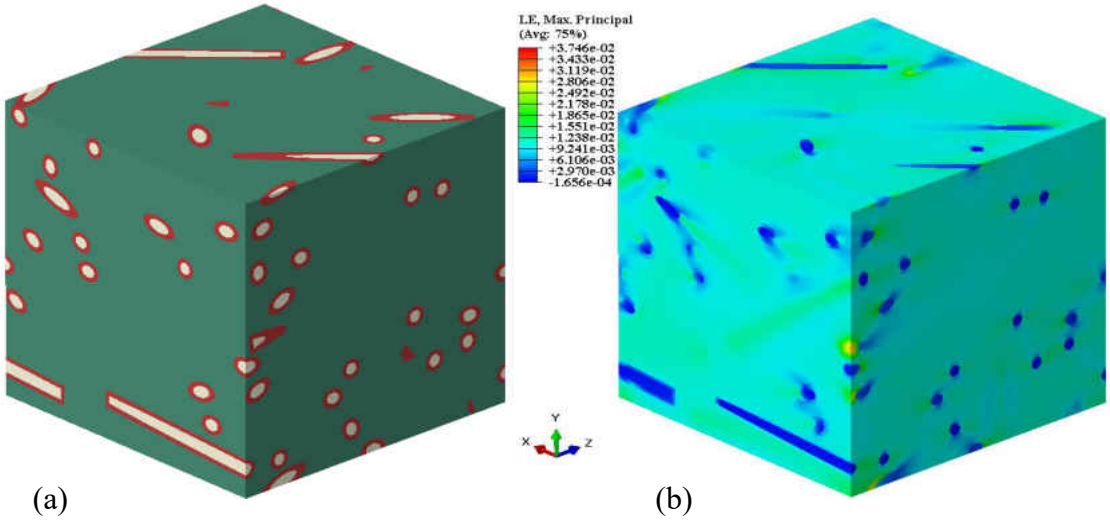

Figure 55 (a) shows a RVE model of 0.3 wt. CNT reinforced epoxy composites with interface considered and different color in the model represents different material; (b) the contour plot of maximum principal logarithmic strains corresponding to RVE model shown in the left, the model is loaded along z axis.

Table 16: The elastic modulus of composites represented by RVE with different types of CNT and interfaces. Isotropic CNT has the same elastic modulus (1 TPa) along different directions, while the elastic modulus of anisotropic CNT is different along different directions: 1 TPa along the axial direction and 30 GPa along radial and circumferential directions. The volume fraction of the interface is 6% when the interface is considered.

Model type	Elastic modulus (MPa)	Relative error (%)
Experiment	3125.43	-
Isotropic CNTs, no interface	3655.03	16.9
Anisotropic CNTs, no interface	3008.12	3.75
Isotropic CNTs + interface	3798.54	17.7
Anisotropic CNTs + interface	3065.16	1.59

As Table 16 shows, if the interface is not considered, the RVE model with isotropic CNTs inclusions gives a high percent error of 16.9%. Consideration of anisotropic CNTs would lead to a tremendous reduction of error rate which is 3.75% to predict the elastic modulus of CNT reinforced epoxy composites. Furthermore, this error rate is reduced to only 1.59% when the

influence of interface is considered, which shows a good correlation between experiment and simulation.

5.3.2 Plasticity of Metal Matrix Composites

Metal matrix composites are another type of composites that draws more and more attention around the world. In this case study, CNT reinforced aluminum (Al) composites are generated with this ***3D RVE Toolbox***. The volume fraction of CNTs is 3%, and the volume fraction of the interface is 7% if the influence of the interface is considered. The hardened strain of the interface is assumed to be 0.3. The concept of hardened strain is taken from Long et al. (Long et al., 2015). The mechanical properties of pure aluminum (Song et al., 2020) are defined in Table 17, and the swift hardening law shown below is employed to describe the plasticity of pure aluminum. The mechanical properties of CNT are defined in the above section.

$$\sigma = A\left(\varepsilon_0 + \varepsilon_p\right)^n \tag{49}$$

where ε_p is the plastic strain, σ is the corresponding stress, n, A and ε_0 are coefficients and they can be decided from experiments: n is the hardening exponent, A is the stress amplitude and ε_0 is the strain shift.

Table 17 Mechanical properties of pure aluminum used in finite element simulations.

$\boldsymbol{Density, \rho}$		$\mathbf{2700\ kg/m^3}$
$\boldsymbol{Young's\ modulus, E}$		$69\ GPa$
$\boldsymbol{Poisson\ ratio, \nu}$		0.33
Swift hardening law	A	204
	ε_0	0.00285
	n	0.1769

Figure 56 shows the comparison of different RVE model configurations. It can be easily identified that CNTs lead to much-strengthened composites compared to pure aluminum. What's more, the anisotropy of CNTs also has an important impact on the plasticity of CNT reinforced composites. For example, at the true strain of 2.95%, the corresponding true stress of pure aluminum is 110 MPa. Under the same true strain, the corresponding true stress of 3% vol. isotropic CNT reinforced aluminum composites is 146.2 MPa, but if the anisotropy of CNTs is considered, the corresponding true stress is 123.4 MPa: there is an 18.5% difference. The influence of interface on the mechanical properties of CNT reinforced composites cannot be neglected, either. For 3% vol. anisotropic CNT reinforced Al composites, the true stress is 127.2 MPa if 7% vol. of the interface is considered when the hardened strain is assumed to be 0.3: there is a 3.1% difference compared to the 123.4 MPa when the interface is not considered. This proves the importance of interface and anisotropy of inclusions on the mechanical properties of CNT reinforced composites.

Figure 57 presents the contour plot of the equivalent plastic strain of 3% vol. anisotropic CNT reinforced aluminum composites with interface considered, and it shows the local plastic strain in the cut view Figure 57 (b) for the matrix which is also part of the resource for mechanical strengthening. Figure 57 (c) presents the von Mises stress contour plot for the corresponding cut view which shows large stresses all come from inclusions.

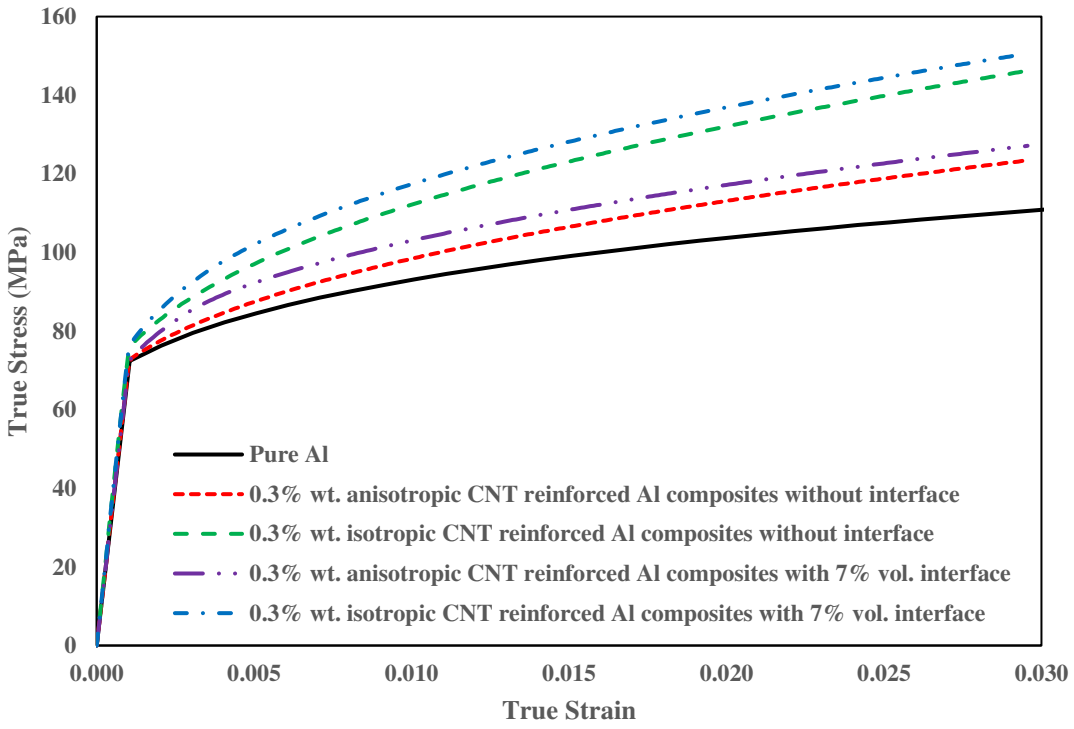

Figure 56. The different stress-strain curves under different types of CNTs and interfaces. The result shows that the CNTs can strengthen the aluminum matrix, and different configuration has a different strengthening effect. The RVE model with isotropic CNTs and interface gives the best mechanical strengthening among the four configurations.

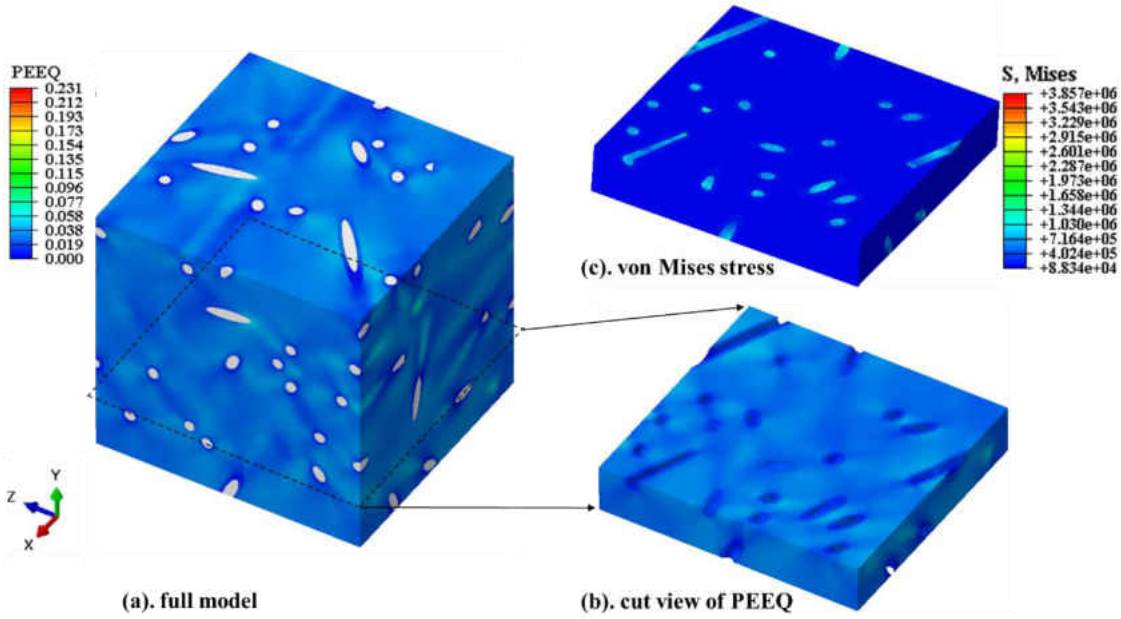

Figure 57 (a): the contour plot of accumulated equivalent plastic strain (PEEQ) of the 3D RVE model for the anisotropic CNT reinforced aluminum composites at 2.96% equivalent strain under uniaxial tension along the z-axis; (b): the cut view of the 3D model from y plane view which shows the local plastic strain of matrix and interface; (c): presents the contour plot of von Mises stresses of the corresponding cut view.

CHAPTER 6 THERMAL CONDUCTIVITY OF CU/CNT COMPOSITES

In this chapter, the main objective is to study the influences of inclusion size, volume fraction, shape, orientation, anisotropy, and volume fraction of voids (and inclusions) and the interfacial thermal resistance on the effective thermal conductivity of composites by finite element analysis. On the microscopic scale, the heat conduction of CNT reinforced composites is mainly caused by the vibrational motion of phonons. From the macroscopic perspective, there are three kinds of phonons – the phonons in the CNTs, interface, and matrix, and these different kinds of phonons lead to different macroscopic thermal properties of CNT, interface, and matrix (X. Li et al., 2012). So following Li et al. method, the macro thermal properties are used in FEA to calculate the effective thermal conductivities of CNT reinforced composites. The RVE approach is used to predict the thermal conductivity of the porous medium and composites. Random sequential adsorption algorithm (Evans, 1993) is employed to create the inclusions in the matrix. The finite element software Abaqus/Standard (Simulia, 2017) is used for the numerical simulations.

In reality, voids cannot be completely eliminated from composite materials. For example, the void content is approximately 1% for some aerospace applications, and other grades of composites can have higher void content for the consideration of performance (Boey & Lye, 1992). The existence of voids in composites could also influence the effective thermal conductivity of composites. Under this circumstance, the composites can be composed of three components: matrix, inclusions, and voids. Effective thermal conductivity can be affected by four factors: matrix, inclusions, voids, and interfacial thermal resistance. For simplicity, the void can be assumed as another type of inclusion whose thermal conductivity is nearly zero. There are two conditions according to the relationship of thermal conductivity between the matrix and inclusions.

The thermal conductivity of the matrix is greater than that of inclusion. Under this circumstance, one example is that the composites are now porous materials. The thermal conductivity of air is around $0.027\ Wm^{-1}K^{-1}$ which is negligible compared to that of matrix like aluminum. In this paper, the thermal conductivity of inclusions is assumed to be 0 (D. J. Yang et al., 2002; X. Yang et al., 2013).

The thermal conductivity of the matrix is less than that of inclusions. Under this circumstance, one example is Al/CNT composites with zero void ratio. when we investigate the effective thermal conductivity of composites under this condition, we will take CNTs as inclusions, and take aluminum as the matrix. We take the thermal conductivity of CNTs as $3000\ Wm^{-1}K^{-1}$, and the thermal conductivity of aluminum as $250\ Wm^{-1}K^{-1}$ (Bakshi, Patel, & Agarwal, 2010; Engineeringtoolbox.com, 2017; Yoshida & Morigami, 2004).

Both two conditions are to be investigated to study how different factors can influence the effective thermal conductivity of composites.

6.1 Methodology

6.1.1 Random Sequential Adsorption Procedure

Random sequential adsorption (RSA) technique has been widely used for the creation of spheres, ellipsoids, and cylinders in the study of particle reinforced composites (Duschlbauer, BÖhm, & Pettermann, 2006; S. Kari, Berger, & Gabbert, 2007; Pan, Iorga, & Pelegri, 2008; Williams & Philipse, 2003). In this work, the RSA algorithm is employed to generate the RVE model which contains inclusions. Spheres and cylinders are the inclusion geometries that will be studied in this study. During the modeling process of RSA, inclusions are randomly added to the system. If this

inclusion does not interfere with any previously added inclusions, it would remain in the rest of the process.

The main step for an RSA procedure is interference checking. For spherical inclusions, only four parameters are needed to generate a sphere in 3D space: the center point coordinates $C(x, y, z)$ and radius r of the sphere. So for any two spheres $sphere1(x_1, y_1, z_1, r_1)$ and $sphere2(x_2, y_2, z_2, r_2)$, if $\sqrt{(x_1 - x_2)^2 + (y_1 - y_2)^2 + (z_1 - z_2)^2} > (r_1 + r_2)$, there is not intersection between these two spheres.

For cylindrical inclusions, seven parameters are necessary to generate a cylinder in 3D space: the center point of cylinder $C(x, y, z)$, radius r, cylinder height h, and Euler angles ϕ and θ. The definition of aspect ratio for cylinders is the ratio of cylinder height to cylinder diameter (h/d). For detailed modeling process, please refer to 0.

6.1.2 Model Assumptions and Boundary Conditions

As stated by Li et al. (X. Li et al., 2012), the CNTs are not straight at the microscale. So even though the aspect ratio of CNTs can be as high as 700, the effective aspect ratio is not that high due to its curvature. To save computational cost and capture the most important features for the study of effective thermal conductivity of composites, three simplifications are made: a). CNTs are simplified to straight cylinders; b). the mechanical properties of matrix and inclusions are temperature independent; c). the thermal conductivity of CNTs is assumed to be isotropic.

The dimension of all the FE models used here is $100nm \times 100nm \times 200nm$ $(for\ x \times y \times z)$. An example of composites with cylindrical inclusions is shown in Figure 58. Tetrahedral solid

meshes are used for all the models. The static solver of the general-purpose finite-element code Abaqus/Standard (Simulia, 2017) is used for the computational analysis.

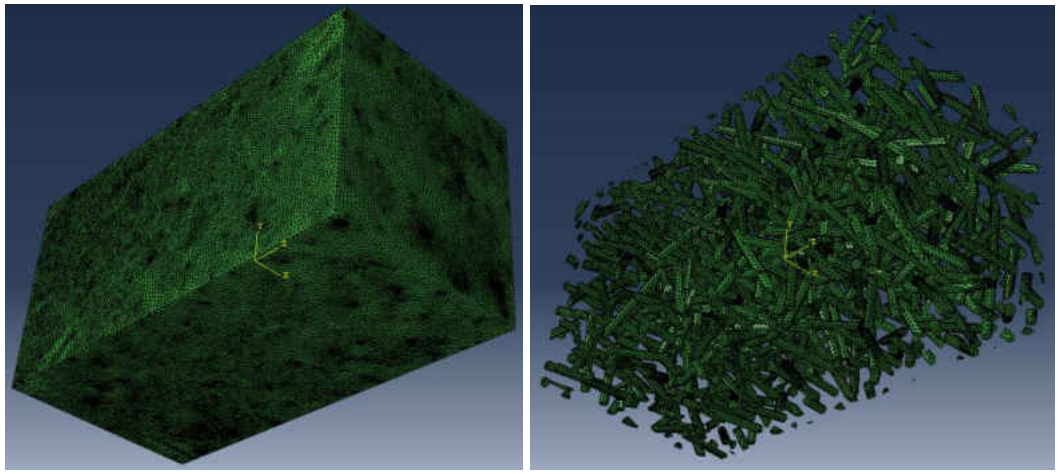

Figure 58: Finite element meshes of composites (left) and inclusions (right).

Lu et al. (Lu & Chen, 1999) pointed out that for metal foams, the heat transfer is mainly contributed from solid conduction, and the contribution of radiation and convection is negligible. In this paper, only heat conduction is considered. For thermal conductivity simulations, constant temperatures of $300K$ and $350K$ are assigned to the bottom (-z axis) and top (+z axis) surfaces of the finite element model, respectively, and the four sidewalls are set as to be adiabatic. The other four surfaces are made adiabatic so that the heat flux only flows along z the axis. The rate of heat flow can be calculated from the simulation. Then the effective thermal conductivity is achieved by Fourier's law which is shown in Eq. (46).

6.2 Results and Discussions

In this section, finite element simulations of different inclusions conditions (including geometry, volume fraction, orientation, aspect ratio) are presented and compared. Based on a validated

model, these results offer more insights about the inclusions' effects on thermal conductivity. For all the 3D simulations presented below, a mesh sensitivity study is carried out, and mesh convergence is achieved.

6.2.1 Model Validation

In order to verify that the model setups including boundary conditions are correctly applied, simple 2D simulations are carried out and compared with analytical solutions. The parallel model and series model are created, and the comparison between FEA and analytical solutions are plotted in Figure 60. Note that the thermal conductivity of inclusions (CNTs) is $3000Wm^{-1}K^{-1}$ and the thermal conductivity of the matrix is $250Wm^{-1}K^{-1}$. It shows that the FEA predictions match well with analytical models.

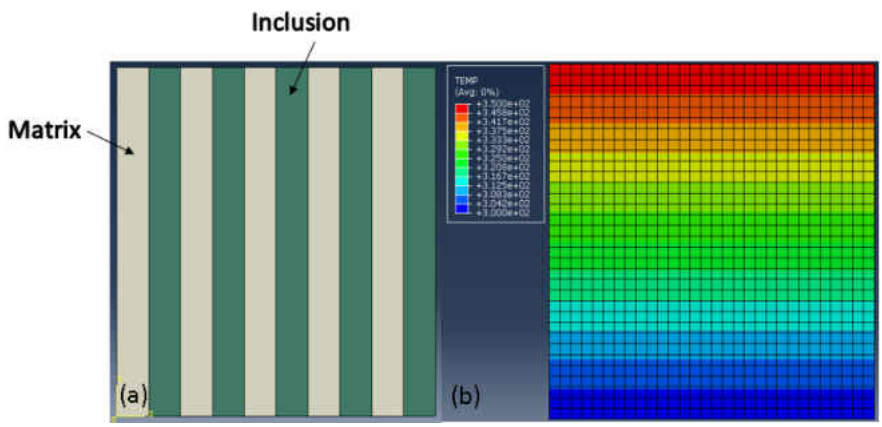

Figure 59: (a). A 2D parallel model of composites consisting of matrix and inclusions. (b). FE simulation results of temperature distribution.

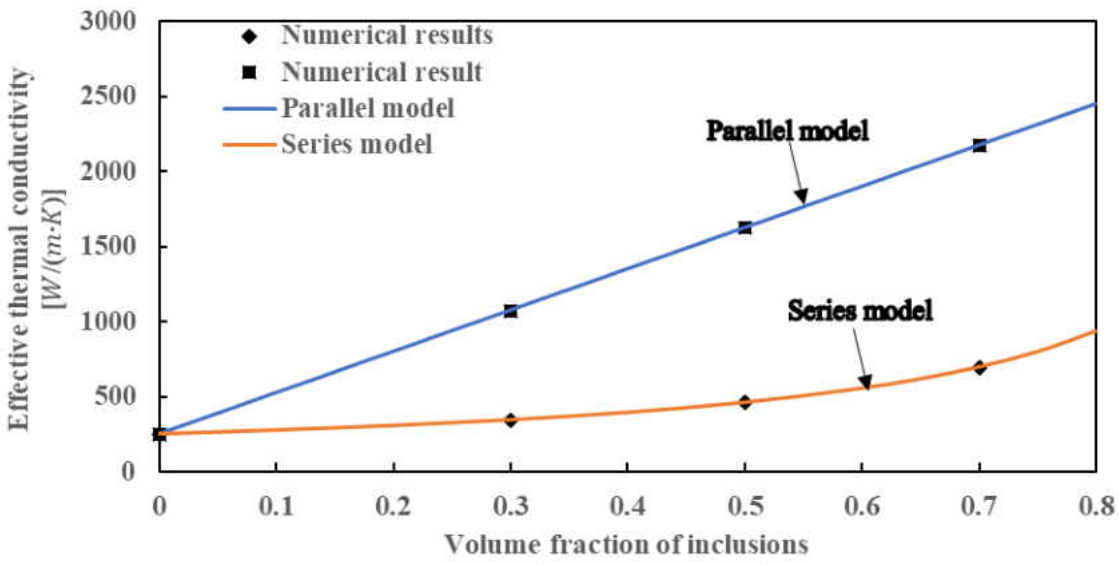

Figure 60: Comparison of theoretical solutions and numerical predictions for the parallel models and series models. An excellent correlation is achieved.

6.2.2 Influence of Porosity

To understand the effects of the pores on thermal conductivity, a round of parametric studies are conducted. The key parameters studied include pore relative size, pore orientation, and pore aspect ratio. In this study, the thermal conductivity of the matrix is $250 Wm^{-1}K^{-1}$, and the thermal conductivity of pores is $0\ Wm^{-1}K^{-1}$.

6.2.2.1 Influence of pore relative size

Spherical pores are placed to investigate the influence of pore size since the radius is the controlling variable for spheres. Thus we can set up a direct relationship between pore relative size and effective thermal conductivity of materials. Simulation results are shown in Figure 61. It is found that the volume fraction of pores increases, the effective thermal conductivity of these porous materials decreases. Keeping the same pores volume fraction, as the radius of pores increases, the

effective thermal conductivity of porous material doesn't change much. The radius of spheres has a negligible influence on the effective thermal conductivity of porous materials.

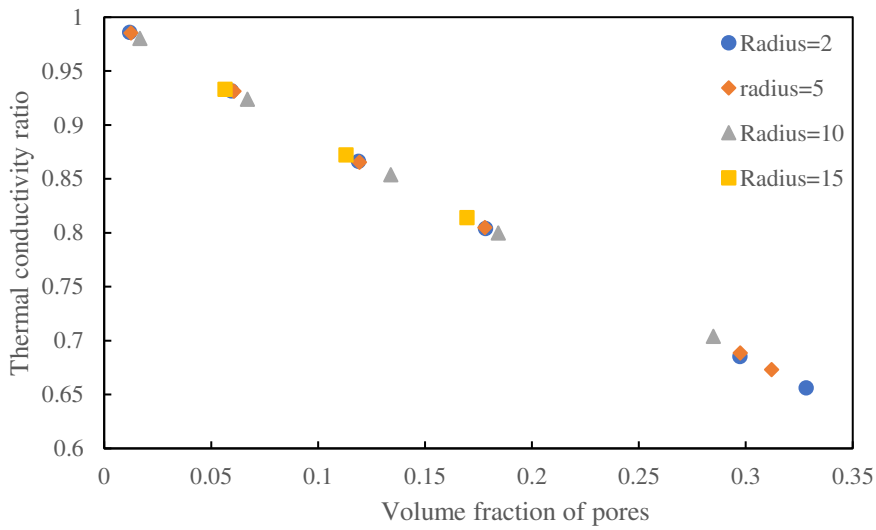

Figure 61: Influence of pore size on the effective thermal conductivity of porous materials. Keeping the same volume fraction of pores, the radius of pores has a negligible effect on effective thermal conductivity.

6.2.2.2 Influence of pore orientation

Pore orientation does not influence the effective thermal conductivity of porous materials with spherical voids, but it has an influence on that of materials with non-spherical pores. Cylindrical pores are used to investigate the void orientation effect. The voids are distributed inside the material by three types: pores allocated vertically, horizontally, and randomly, respectively. The pores' diameter is constant and equal to 2 nm, and the aspect ratio used in this study is 10. 'Vertically aligned' means that the height direction of all the pores is along the heat flow direction. 'Horizontally aligned' means that the height direction of all the pores is perpendicular to the heat flow direction. 'Randomly distributed' denotes that all the pores are positioned randomly. These three terms will be used thereafter. The simulation results are shown in Figure 62, which demonstrates that the pore orientation has an influence on the effective thermal conductivity.

Materials with vertically aligned pores have the best thermal conductivity, materials with horizontally aligned pores have the worst thermal conductivity, and the thermal conductivity of materials with randomly oriented pores is between these two aforementioned materials. A similar conclusion was found by Ordonez-Miranda et al. (Ordonez-Miranda & Alvarado-Gil, 2012) which was proven by effective medium theory.

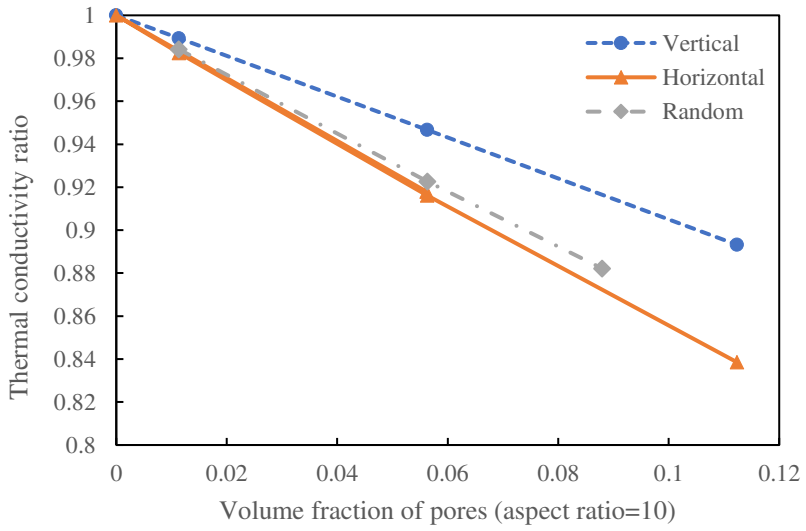

Figure 62: Influence of pore orientation on the thermal conductivity of porous materials

6.2.2.3 Influence of pore aspect ratio

The effect of pore aspect ratios on the thermal conductivity is studied for a wide range of aspect ratios between 1 and 15 and for a range of volume fraction of pores between 0 and 0.1. Straight cylinders are used as pores, and the diameter of all cylinders is set to be 2 nm. The results of FEA simulations for thermal conductivity are displayed in Figure 63 where all cylinders are vertically aligned. It's shown that thermal conductivity grows as the aspect ratio increases when the aspect ratio is less than 5. When the aspect ratio is greater than 5, the thermal conductivity of porous materials does not change much with the increase of aspect ratio. A similar result was also reported by Aydin et al. (Nabovati, Llewellin, & Sousa, 2009).

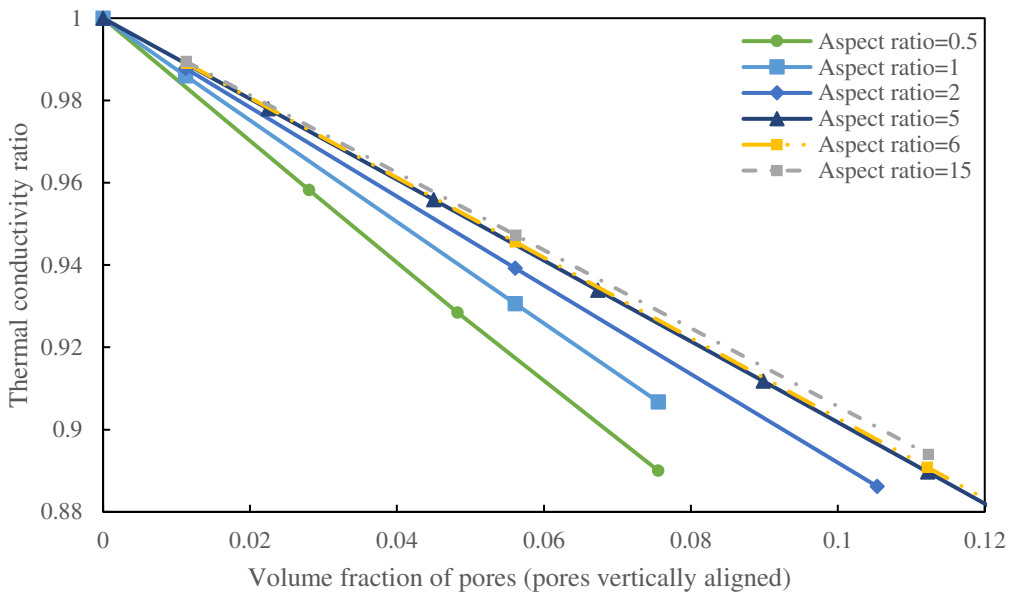

Figure 63: Influence of aspect ratios on the thermal conductivity of porous materials with pores vertically aligned.

However, if all the pores are horizontally positioned in the matrix while other parameters are kept the same, different trends of thermal conductivity for different aspect ratios appear. The smaller the aspect ratio of pores is, the greater the effective thermal conductivity of the materials is.

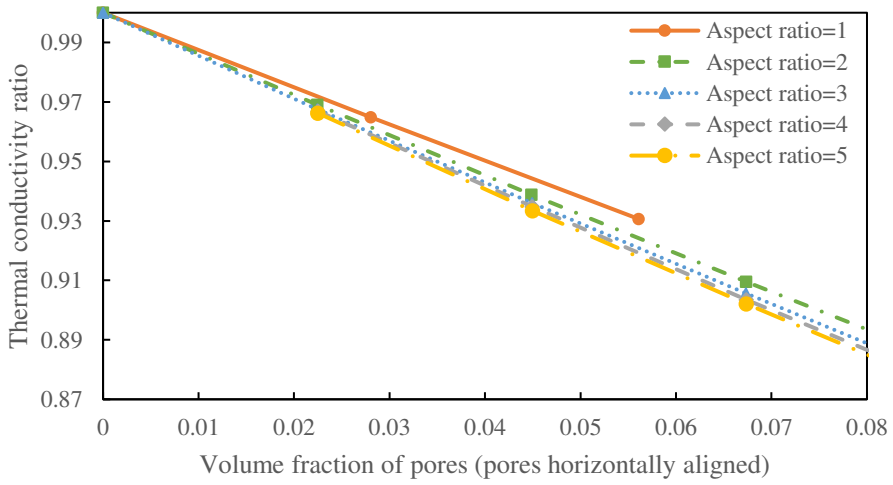

Figure 64: Influence of aspect ratios on the thermal conductivity of porous materials with pores horizontally aligned.

6.2.3 Composites with a better Thermal Conductivity of Inclusions

The similar parametric studies, like those in Section 6.2.2, are conducted for another case of composite whose inclusions have better thermal conductivity than the matrix. In this study, the thermal conductivity of the matrix takes $250Wm^{-1}K^{-1}$ (i.e. aluminum), and that of the inclusions is $3000Wm^{-1}K^{-1}$ (i.e. CNTs)

6.2.3.1 Influence of Inclusion Size

Spherical inclusions are placed to study the influence of inclusion size as the radius is the key variable for spheres to represent inclusion size. The model setup is shown in Figure 65. Figure 66 shows the relationship between inclusion size and effective thermal conductivity, and it indicates that the inclusion size has no significant influence on the effective thermal conductivity. The trend is similar to that shown in Section 6.2.2.1 for pores.

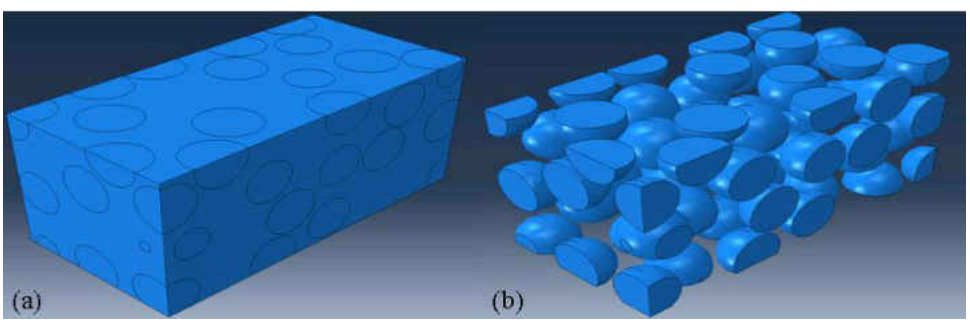

Figure 65: Composites with spherical inclusions. (a) whole composite RVE model. (b) Inclusions only.

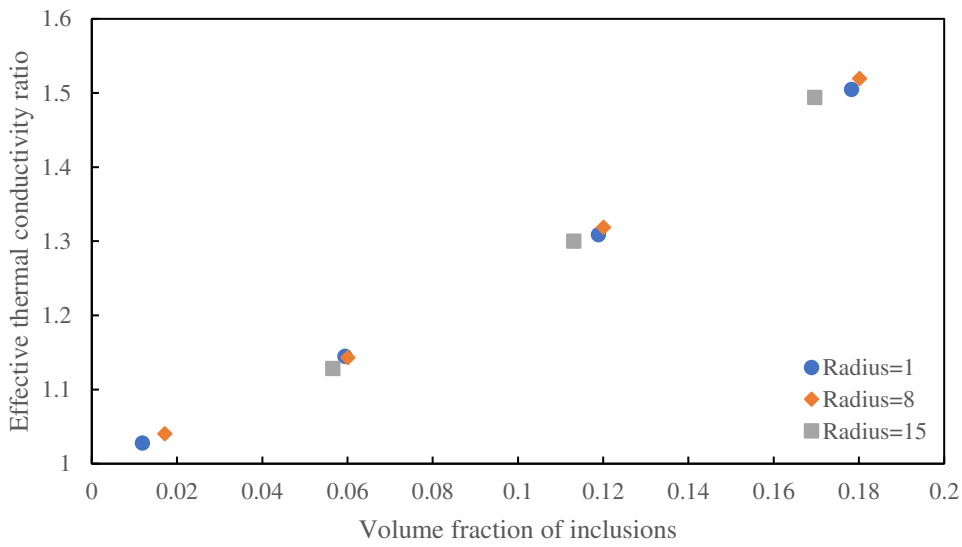

Figure 66: Influence of inclusion size on the effective thermal conductivity of composites is negligible. The volume fraction of inclusions has a significant effect instead.

6.2.3.2 Influence of Inclusion Orientation

Inclusion orientation does not have an influence on the effective thermal conductivity of composites with spherical inclusions but has an influence on that of composites with non-spherical inclusions. Cylindrical inclusions are used to investigate the inclusion orientation effect. Note that the aspect ratios are selected to be 10 for all the models in this section. Figure 68 indicates that composites with vertically aligned (along hear flow direction) inclusions have the best thermal conductivity, and composites with horizontally aligned inclusions have the worst thermal conductivity at a given volume fraction. The random one is in between. This trend is the same as that of pores.

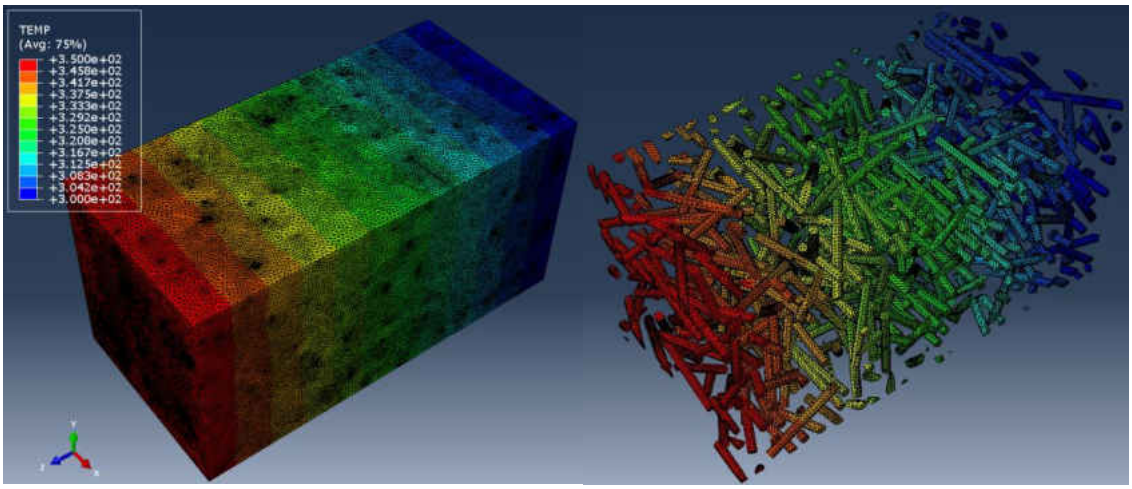

Figure 67: An RVE model of the matrix (left) and inclusions (right). The contour plot shows the temperature distribution in the FE simulation.

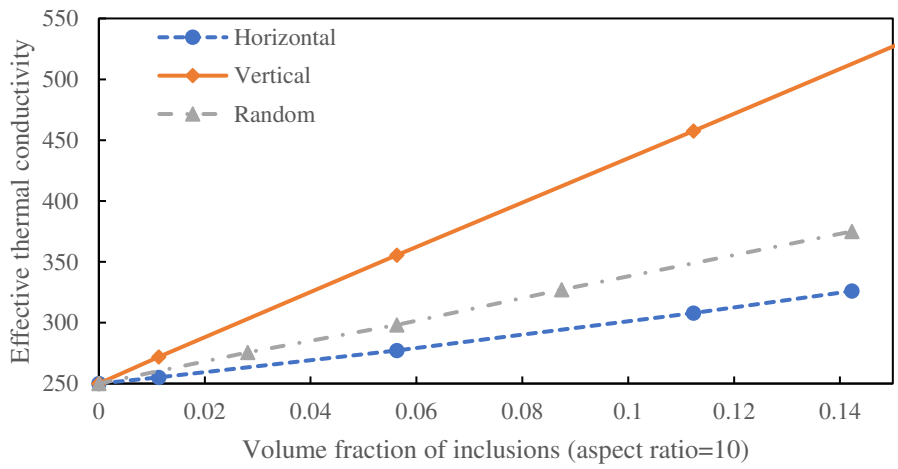

Figure 68: Influence of inclusion orientations on the effective thermal conductivity of composites.

6.2.3.3 Influence of Inclusion Aspect Ratio

In this parametric study of inclusion aspect ratio, we still take carbon nanotubes (CNTs) as inclusion which has drawn a lot of attention from different fields, and it has been proven that the aspect ratio of CNTs plays an important role in the strengthening mechanism of nanocomposites (Long et al., 2015). Figure 69 shows that the results about the aspect ratio of inclusions, which also has a positive influence on effective thermal conductivity if all inclusions are vertically aligned.

The effective thermal conductivity of composites increases with the increase of aspect ratio given the same volume fraction of inclusions.

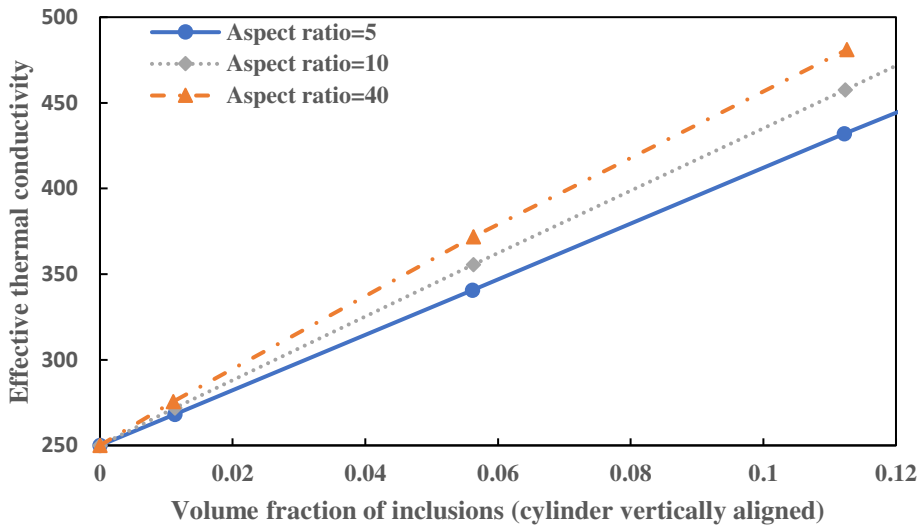

Figure 69: Influence of inclusion aspect ratios on the effective thermal conductivity of composites while inclusions are vertically aligned

However, if all the inclusions are all horizontally aligned inside the matrix (inclusion perpendicular to the heat flow direction) while keeping other parameters the same, different trends of thermal conductivity for various aspect ratios present. The smaller the aspect ratio of inclusions is, the greater the effective thermal conductivity of the composites is. The simulation results are illustrated in Figure 70, where three aspect ratios are studied, 2, 5, and 10.

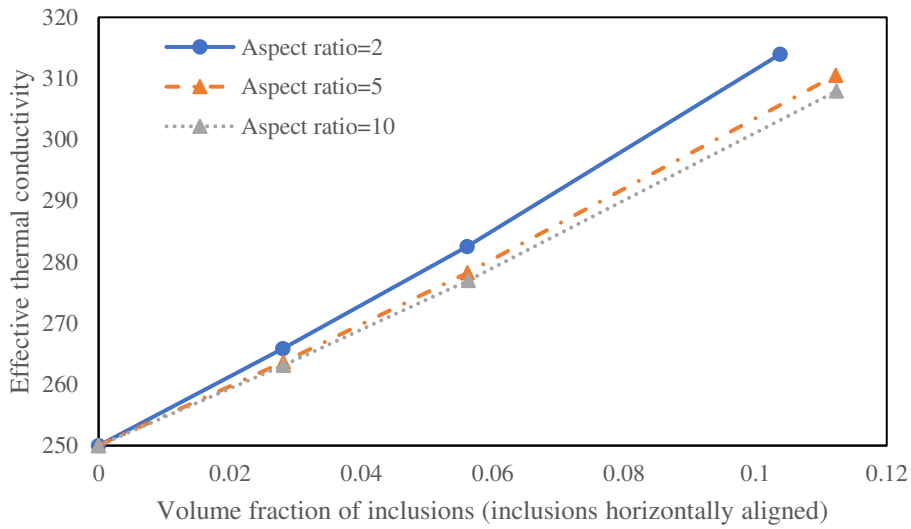

Figure 70: Influence of inclusion aspect ratios on the effective thermal conductivity of composites while inclusions are horizontally aligned

6.2.3.4 Influence of Interfacial Thermal Resistance

Interfacial thermal resistance has been proven to play a significant role in the thermal conductivity of composites (Jiajun & Xiao-Su, 2004; X. Li et al., 2012; C.-W. Nan et al., 1997). The effective thermal conductivity of composites with a wide range of interfacial thermal resistance was calculated with the proposed RVE model. In this work, interfacial thermal conductance is modeled by the *gap conductance* keyword in Abaqus. The results are shown in Figure 71. It indicates that the effective thermal conductivity of composites decreases with the increase of interfacial thermal conductivity while keeping all other parameters the same. Note that the thermal conductivity of the matrix is $250Wm^{-1}K^{-1}$, and the thermal conductivity of inclusions is $3000Wm^{-1}K^{-1}$. The effective thermal conductivity of composites with a high volume fraction of inclusions is more sensitive to interfacial thermal resistance. For example, the effective thermal conductivity of composites with 2 vol% of inclusions (aspect ratio 20) is better than that of composites with 1 vol% of inclusions (aspect ratio 20) when the interfacial thermal resistance is lower than

$5 \times 10^{-8}\ m^2K/W$. However, when the interfacial thermal resistance is greater than $5 \times 10^{-8}\ m^2K/W$, the effective thermal conductivity of composites with 2 vol% of inclusions (aspect ratio 20) is not as good as that of composites with 1 vol% of inclusions (aspect ratio 20). This could be caused by the difference of contact area between the matrix and inclusions: the higher the volume fraction of inclusions is, the greater the contact area is. From this point of view, given the same volume fraction of inclusions, the larger aspect ratio of inclusions leads to a smaller contact area, and this makes the effective thermal conductivity of composites containing inclusions with a large aspect ratio better. It should be noted that only limited cases are studied for this interesting phenomenon. More analytical studies are needed in the future.

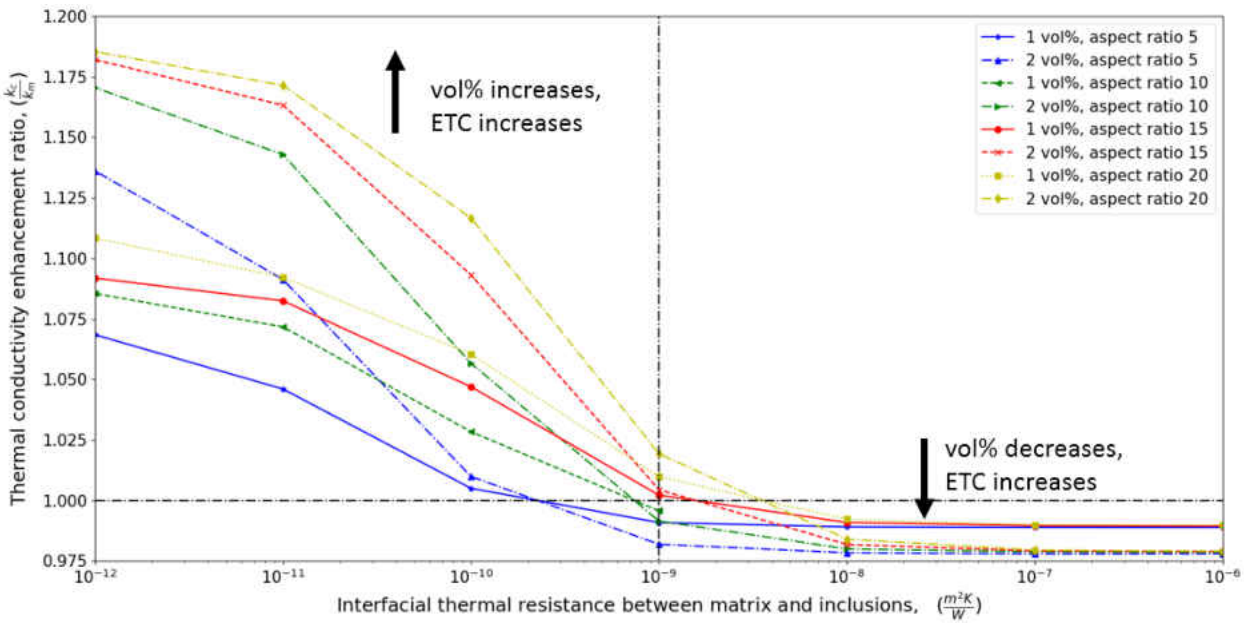

Figure 71: Influence of interfacial thermal resistance on the effective thermal conductivity of composites while inclusions are all vertically aligned. Two different trends are observed based on interfacial thermal resistance: The effective thermal conductivity (ETC) decreases with the increase of volume fraction of inclusions if interfacial thermal resistance is small; vice versa.

6.2.3.5 Influence of Anisotropic Properties of Inclusion

As stated above, the anisotropic material properties have much influence on the applications of materials. Che et al. (Che, Cagin, & Goddard III, 2000) reported that the CNT bundle has very large thermal conductivity anisotropy. The thermal conductivity along the radial direction is estimated at around 5.6 $Wm^{-1}K^{-1}$, while the thermal conductivity of CNT along the axial direction is about 3000 $Wm^{-1}K^{-1}$. To set up the model, local coordinate systems are generated for each of the inclusions. Figure 72 displays a 3D RVE model with anisotropic CNTs. The values for thermal conductivities along axial direction and radial direction are 3000 $Wm^{-1}K^{-1}$ and 5.6 $Wm^{-1}K^{-1}$, respectively. The matrix material used in the RVE model is aluminum whose thermal conductivity is 250 $Wm^{-1}K^{-1}$. Figure 73 presents the comparison of effective thermal conductivities of isotropic CNT and anisotropic CNT. It shows that when the anisotropic properties are considered, the effective thermal conductivities are way lower than that with isotropic CNT. It implies the importance of anisotropy and shows the anisotropic properties should be considered for material design and numerical studies in the future.

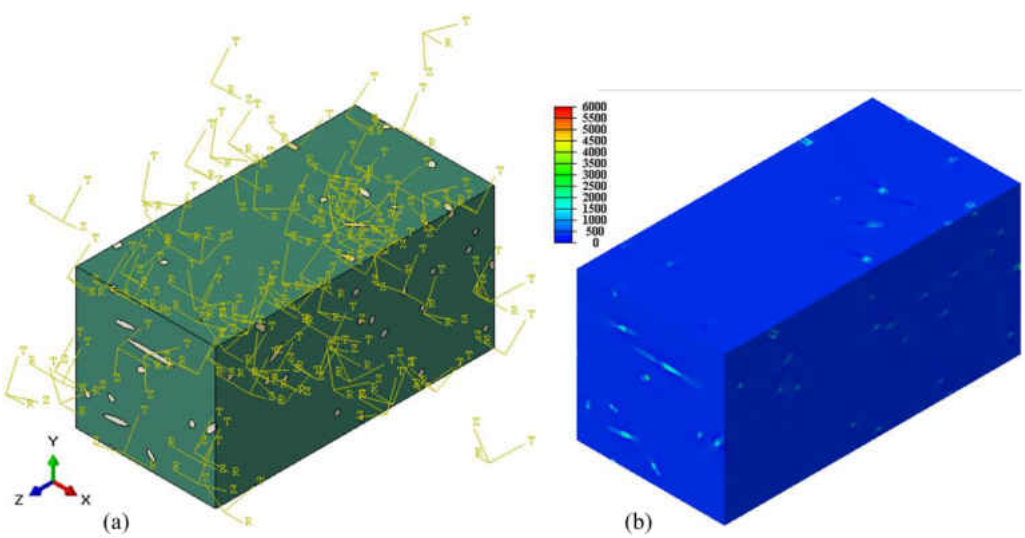

Figure 72: (a). A 3D RVE model where the inclusions have anisotropic thermal conductivity property; (b). the contour plot of the magnitude of the heat flux vector for the corresponding RVE model.

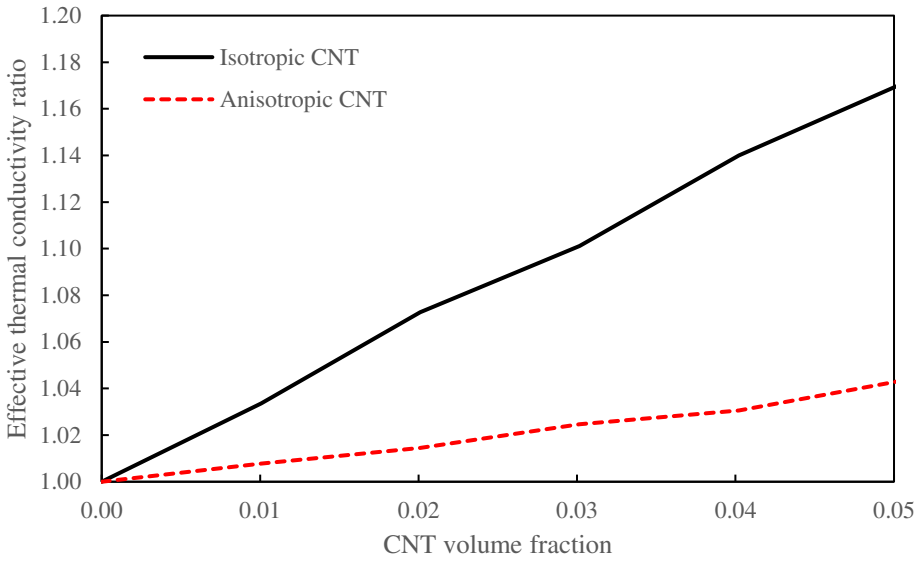

Figure 73: Influence of thermal conductivity anisotropy on the effective thermal conductivity of composites. The matrix material is aluminum with a thermal conductivity of 250 $Wm^{-1}K^{-1}$,

6.3 Summary

To explore the influencing factors of inclusions on effective thermal conductivity for composites, a customized Python script is created to automatically generate three-dimensional finite element RVE models for Abaqus software. A random sequential adsorption algorithm is used in the Python script to have the ability of randomly introducing inclusions into the matrix without any interference among the inclusions. A total of 900 simulations are carried out to study the influence of inclusion size, aspect ratio, orientation, and interfacial thermal resistance. This paper also discussed the influence of thermal conductivity anisotropy of inclusions on the effective thermal conductivity of composites by the 3D RVE method which has not been done before. Spherical inclusions are used to investigate the effect of inclusion size, and cylindrical inclusions are deployed to explore the effects of inclusion aspect ratio and orientation. The results of simulations and analytical solutions are compared, which proves the accuracy of the FEA simulation.

- The thermal conductivity of composites is almost not influenced by the relative size of inclusions under the same volume fraction of inclusions if interfacial thermal resistance is not considered.
- Among composites with vertically aligned inclusions, randomly distributed inclusions and horizontally aligned inclusions, the composites with vertically aligned inclusions have the best thermal conductivity, and the composites with horizontally aligned inclusions have the worst thermal conductivity given the same volume fraction of inclusions. The random one is in between.
- If all cylindrical inclusions are aligned along the heat flow direction (vertical case), the effective thermal conductivity of composites grows as the increase of aspect ratio of cylindrical inclusions for a given volume fraction of inclusions. Note that when the aspect ratio is greater than a certain number (i.e. 5.0), the thermal conductivity of porous materials does not change much with the increase of aspect ratio.
- If all cylindrical inclusions are aligned perpendicular to the heat flow direction (horizontal case), the effective thermal conductivity of composites decreases as the increase of aspect ratio of cylindrical inclusions given the same volume fraction of inclusions.
- The influence of aspect ratio and orientation of inclusions (including pores) becomes bigger as the increase of volume fraction of inclusions (including pores).
- The effective thermal conductivity of composites decreases as the increase of interfacial thermal resistance. The interfacial thermal resistance has a greater influence on the effective thermal conductivity as the increase of volume fraction of inclusions. The effective thermal conductivity of composites can be worse than that of the matrix if the interfacial thermal resistance is higher than a critical value

- The effective thermal conductivity of composites can be greatly affected by the large thermal conductivity anisotropy of inclusions.

In conclusion, this RVE model and simulations results provide very useful guidance for material design and material property evaluation for composites and porous materials.

CHAPTER 7 STRENGTH AND DUCTILITY TRADE-OFF OF COMPOSITES

This chapter focuses on the trade-off between nano composite materials' strength and ductility and the influence of temperature, which has seldomly been comprehensively analyzed in literature yet. In Chapter 4, we theoretically characterize the influences of load transfer, Orowan strengthening effect and thermal expansion mismatch of composites, and temperature effect on the strengthening mechanism of CNT reinforced metal matrix composites. Combining with stress based modified Mohr-Coulomb (sMMC) ductile fracture model (Bai & Wierzbicki, 2009; Qiao et al., 2016), an analytical model of ductility prediction is then derived. The strengthening model and the ductility model are fully decoupled which can make the application of each model more user-friendly. A good agreement has been achieved between the theoretical models and two sets of recent experimental data.

7.1 Theoretical Models of Strengthening Mechanism and Ductility of CNT Reinforced Metal Matrix Composites

In this section, the analytical solutions of CNT reinforced nano composites' strength and ductility will be presented. The material strength is described by the overall stress-strain curves for composites. The material ductility will be characterized by the equivalent fracture strains under different stress states, different temperatures, with different material compositions.

7.1.1 Theoretical Model of Strengthening Mechanism with Temperature Effects

Load bearing effect, Orowan looping effect, and thermal expansion mismatch are viewed as three important factors of the strengthening mechanism for CNT reinforced metal matrix composites (George et al., 2005; Long et al., 2015). Zhang and Chen (Z. Zhang & Chen, 2008) pointed out

that the Orowan looping effect plays an important role in the particulate-reinforced metal matrix composites and that the effect of Orowan strengthening effect increases as the size scale of inclusions decreases. The diameters of CNTs are always in the nanoscale, so the Orowan looping effect is not negligible.

Based on George et al. method (George et al., 2005), the strengthening effect of composites under room temperature is proposed as listed in Eq. (50).

$$\sigma_c = \sigma_m(1 + f_{load})(1 + f_{Orowan})(1 + f_{thermal}) \tag{50}$$

where σ_c is the strength of composites, σ_m is the strength of the matrix, f_{load} is the improvement factor associated with load bearing effect, f_{Orowan} is the improvement element which contributes from the Orowan looping, and $f_{thermal}$ is the improvement factor which is related to the thermal expansion mismatch effect.

The strengthening effect factor from Orowan looping mechanism has the following format (Long et al., 2015),

$$f_{Orowan} = \frac{a_1 G_m b}{\sigma_m} \sqrt{\frac{2f_v}{\pi d^2}} ln\left(\frac{d}{2b}\right) \tag{51}$$

Here, b is the Burgers vector of the matrix, G_m is the shear modulus of the matrix material, f_v is the volume fraction of inclusions, and d stands for the diameter of inclusions. a_1 is a free parameter for calibration.

The thermal expansion mismatch factor $f_{thermal}$ takes the following form (Q. Li et al., 2009),

$$f_{thermal} = \frac{a_2 1.25 G_m b}{\sigma_m} \sqrt{\frac{4 f_v (CTE_A - CTE_C)(T_1 - T_2)}{b(1 - f_v)d}}, \tag{52}$$

where T_1 is the maximum operating temperature during the material fabrication process, T_2 is the minimum operating temperature which is usually the room temperature, CTE_A is the thermal expansion coefficient of the matrix material, and CTE_C is the thermal expansion coefficient of inclusions. a_2 is a free parameter that needs to be calibrated based on experimental data.

Regarding the load transfer effect, f_{load} can be simplified to the following equation (Q. Li et al., 2009; Z. Zhang & Chen, 2006).

$$f_{load} = 0.5 f_v \tag{53}$$

Here, f_v is the volume fraction of the inclusions.

The above equations present the strengthening mechanisms of CNT reinforced composites under certain temperature (which usually is the room temperature). When the temperature increases, the matrix material will become softening. Johnson and Cook (Johnson, 1983) proposed a material plasticity model that considers the influence of temperature on material strength. This model has been widely used due to its simplicity and availability of the material database. In this work, a similar approach is adopted and the temperature-dependent material strength model for CNT reinforced composites has the following format in Eq. (54).

$$\sigma_c = \sigma_m \left(1 - \left(\frac{T - T_{room}}{T_{melt} - T_{room}}\right)^m\right)(1 + f_{load})(1 + f_{Orowan})(1 + f_{thermal}) \tag{54}$$

Here, T_{room} is the room temperature or a reference temperature, T_{melt} is the melting temperature of the matrix, and m is a parameter.

Combining all the strengthening factors and temperature into one equation, the temperature dependent material strength model becomes Eq. (55).

$$\sigma_c = \sigma_m \left(1 - \left(\frac{T - T_{room}}{T_{melt} - T_{room}}\right)^m\right)(1 + 0.5 f_v)\left(1 + \frac{a_1 G_m b}{\sigma_m}\sqrt{\frac{2 f_v}{\pi d^2}}\, ln\left(\frac{d}{2b}\right)\right)\left(1 + \frac{a_2 1.25 G_m b}{\sigma_m}\sqrt{\frac{4 f_v (CTE_A - CTE_C)(T_1 - T_2)}{b(1 - f_v) d}}\right) \tag{55}$$

There are three parameters for calibration: a_1, a_2 and m. The calibration process can be decoupled which makes it easier to calibrate. First, parameters a_1, a_2 can be calibrated with room temperature testing data. Then, the parameter m can be calibrated with elevated temperature testing data. For instance, if the yield stress is the data that you are interested in, treat the yield stress at reference (room) temperature as the reference data and normalize all the yield stresses at different temperatures and with different volume fractions of CNT. The composite material's strain hardening behavior is considered in the hardening of the matrix material, $\sigma_m(\varepsilon_{pl})$. A detailed explanation will be introduced later in the case study section.

7.1.2 An sMMC Model Based Theoretical Model for Ductility Loss of Nano Composites

For most of the materials, ductility loss is always the side effect of material strengthening. Regarding the metallic material's ductile fracture study, Bai et al. (Bai & Wierzbicki, 2008, 2009) proposed that the metal fracture is highly related to the loading conditions (or stress states). They provided a fracture model called the modified Mohr-Coulomb (MMC) fracture criterion which is an extension for the classical Mohr-Coulomb fracture model. This criterion has good accuracy to predict fracture of many metals and alloys under different loading conditions, and abundant literatures have shown the accuracy of this model on different materials (Bai & Atkins, 2012; Y. Li & Wierzbicki, 2010; Luo et al., 2012).

Three stress invariants of a general stress tensor are defined as:

$$p = -\sigma_m = -\frac{1}{3}(\sigma_1 + \sigma_2 + \sigma_3) \tag{56}$$

$$q = \bar{\sigma} = \sqrt{\frac{3}{2}[\boldsymbol{S}]:[\boldsymbol{S}]} = \sqrt{\frac{1}{2}[(\sigma_1 - \sigma_2)^2 + (\sigma_2 - \sigma_3)^2 + (\sigma_3 - \sigma_1)^2]} \tag{57}$$

$$r = \left[\frac{27}{2}\det([\boldsymbol{S}])\right]^{\frac{1}{3}} = \left[\frac{27}{2}(\sigma_1 - \sigma_m)(\sigma_2 - \sigma_m)(\sigma_3 - \sigma_m)\right]^{\frac{1}{3}} \tag{58}$$

Here, $[\boldsymbol{S}]$ is the deviatoric stress tensor which has the form of $[\boldsymbol{S}] = [\boldsymbol{\sigma}] + p[\boldsymbol{I}]$. $[\boldsymbol{I}]$ is the identity tensor. σ_1, σ_2 and σ_3 are the three principal stresses which have such relationship: $\sigma_1 \geq \sigma_2 \geq \sigma_3$. Stress triaxiality η is a dimensionless term that is related to hydrostatic pressure and its definition is presented in Eq. (59).

$$\eta = \frac{-p}{q} = \frac{\sigma_1 + \sigma_2 + \sigma_3}{3\bar{\sigma}} = \frac{\sigma_m}{\bar{\sigma}} \tag{59}$$

The Lode angle θ is an angle defined on the deviatoric plane and the axis of the principal stresses. It is related to the normalized third deviatoric stress invariant ξ,

$$\xi = \left(\frac{r}{q}\right)^3 = \cos(3\theta) \tag{60}$$

The geometrical representation of the Lode angle is presented in Figure 74 (Bai & Wierzbicki, 2008). The range of Lode angle θ is $\left[0, \frac{\pi}{3}\right]$. After normalization, Lode angle parameter $\bar{\theta}$ is introduced in Eq. (61) where the scope of Lode angle parameter is $[-1, 1]$.

$$\bar{\theta} = 1 - \frac{6\theta}{\pi} = 1 - \frac{2}{\pi}\arccos(\xi) \tag{61}$$

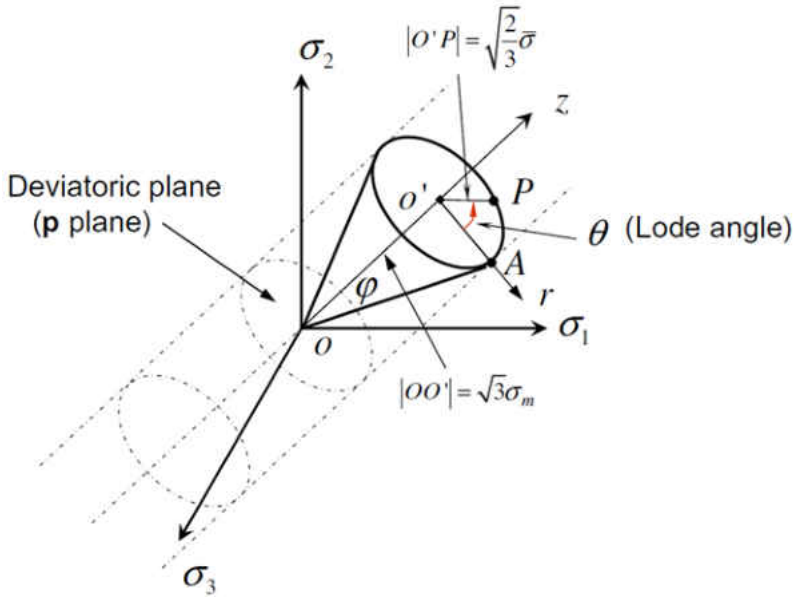

Figure 74. Geometrical representation of a general stress state in the principal-stress-space. Ref. (Bai & Wierzbicki, 2008)

All the loading conditions can be characterized by stress triaxiality and the Lode angle parameter. Table 18 presents the values of stress triaxiality and Lode angle parameters for some typical loading conditions (Bai & Wierzbicki, 2008).

Table 18. Lode angle parameter and stress triaxiality for typical loading conditions (Bai & Wierzbicki, 2008).

Typical loading condition	Analytical solution of stress triaxiality η	The Lode angle parameter $\bar{\theta}$
Uniaxial tension	$\frac{1}{3}$	1
Plastic plane strain tension	$\frac{\sqrt{3}}{3}$	0
Torsion or shear	0	0
Uniaxial compression	$-\frac{1}{3}$	-1
Equi-biaxial plane stress tension	$\frac{2}{3}$	-1
Equi-biaxial plane stress compression	$-\frac{2}{3}$	-1
Plastic plane strain compression	$-\frac{\sqrt{3}}{3}$	0

The modified Mohr-Coulomb model considers both stress triaxiality and the Lode angle parameter on material fracture strain, and it is now mainly used to describe the fracture behavior of metals and alloys.

$$\bar{\varepsilon}_f(\eta,\bar{\theta}) = \left\{\frac{A}{c_2}\left[c_\theta^s + \frac{\sqrt{3}}{2-\sqrt{3}}\left(c_\theta^{ax} - c_\theta^s\right)\left(\sec\left(\frac{\bar{\theta}\pi}{6}\right) - 1\right)\right]\left[\sqrt{\frac{1+c_1^2}{3}}\cos\left(\frac{\bar{\theta}\pi}{6}\right) + c_1\left(\eta + \frac{1}{3}\sin\left(\frac{\bar{\theta}\pi}{6}\right)\right)\right]\right\}^{-\frac{1}{n}}, \quad (62)$$

where A, n, c_θ^s, c_θ^{ax}, c_1 and c_2 are six parameters. The parameters A and n can be taken from the strain power hardening function (Eq. (63)). The value of c_θ^{ax} is a function of Lode angle parameter which is shown in Eq. (64). The four parameters c_θ^s, c_θ^{ax}, c_1 and c_2 need to be calibrated from fracture experiment data.

$$\sigma_f = A{\varepsilon_f}^n \tag{63}$$

$$c_\theta^{ax} = \begin{cases} 1 & if\ \bar{\theta} \geq 0 \\ c_\theta^c & if\ \bar{\theta} < 0 \end{cases} \tag{64}$$

For the fracture of nano composites, brittle fracture and ductile fracture may coexist inside the matrix material. In this way, stress-based fracture criterion could be more appropriate. Based on power hardening law which is presented in Eq. (63), the stress-based modified Mohr-Coulomb (sMMC) fracture model can be described as Eq. (65).

$$\sigma_{cf}(\eta, \bar{\theta}) = \left\{ c_2 \left[c_\theta^s + \frac{\sqrt{3}}{2-\sqrt{3}} (c_\theta^{ax} - c_\theta^s) \left(\sec\left(\frac{\bar{\theta}\pi}{6}\right) - 1 \right) \right] \left[\sqrt{\frac{1+c_1^2}{3}} \cos\left(\frac{\bar{\theta}\pi}{6}\right) + c_1 \left(\eta + \frac{1}{3} \sin\left(\frac{\bar{\theta}\pi}{6}\right) \right) \right] \right\}^{-1}, \tag{65}$$

where σ_{cf} is the fracture stress of composites. Note that the parameters A and n are canceled out after conversion from strain-based fracture criterion back to stress-based fracture criterion, and this further simplifies the model. Furthermore, the same material can present different fracture behaviors under different loading conditions (refer to Ref (Bai & Wierzbicki, 2008) for detailed description), and the format of the modified Mohr-Coulomb model provide the convenience to study the influence of different loading conditions. For example, uniaxial tension test and uniaxial compression test are the most common mechanical experiments in the material science related fields while torsion or shear tests are seldom carried out due to the limitation of testing facility or specimen fabrication equipment. Under such circumstance, $\left[c_\theta^s + \frac{\sqrt{3}}{2-\sqrt{3}} (c_\theta^{ax} - c_\theta^s) \left(\sec\left(\frac{\bar{\theta}\pi}{6}\right) - \right.\right.$

$1\big)\big]$ in the modified Mohr-Coulomb model can be omitted, and the whole model can be simplified to Eq. (66) where there are only two parameters, c_1 and c_2, left.

$$\sigma_{cf}(\eta,\bar{\theta}) = \left\{c_2\left[\sqrt{\frac{1+c_1^2}{3}}\cos\left(\frac{\bar{\theta}\pi}{6}\right) + c_1\left(\eta + \frac{1}{3}\sin\left(\frac{\bar{\theta}\pi}{6}\right)\right)\right]\right\}^{-1} \tag{66}$$

Eq. (66) represents the fracture stress of composites under the influence of stress triaxiality and the Lode angle parameter. For CNT reinforced metal composites, because the strength of CNT is much higher than that of the matrix, it is reasonable to assume that the fracture initiation of composites starts from the matrix. For composites, the fracture of the matrix also means the fracture of composites. Combine Eq. (63), Eq. (66) into Eq. (50), and the fracture strain can be obtained and it is shown in Eq. (67). For the sake of brevity, please refer to Eq. (51), Eq. (52), and Eq. (53) for the definitions of f_{load}, f_{Orowan} and $f_{thermal}$.

$$\bar{\varepsilon} = \left\{\frac{c_2}{A}\left[\sqrt{\frac{1+c_1^2}{3}}\cos\left(\frac{\bar{\theta}\pi}{6}\right) + c_1\left(\eta + \frac{1}{3}\sin\left(\frac{\bar{\theta}\pi}{6}\right)\right)\right]^{-1}\left(1-\left(\frac{T-T_{room}}{T_{melt}-T_{room}}\right)^m\right)^{-1}\left[(1+f_{load})(1+f_{Orowan})(1+f_{thermal})\right]^{-1}\right\}^{\frac{1}{n}} \tag{67}$$

There are seven adjustable parameters, a_1, a_2, A, n, c_1, c_2, and m in the present ductility model, among which the parameters a_1, a_2, and m are also the parameters for the strengthening analytical model. To validate and calibrate the model, there are two sequential calibration methods to follow.

If the strengthening analytical model is also used for the strengthening mechanism study, the values of a_1, a_2, and m can be obtained from Eq. (55). The value of c_1 can be obtained from tests of different loading conditions. The last parameters A, n, c_2 are free parameters for global adjustment.

However, if the strengthening analytical model is not employed in the first place, the seven free adjustable parameters can be treated as free mathematical parameters and be obtained by global optimization. This work can be easily done by software like Python or Excel. In this paper, all the optimization is achieved by Python with the module of inspired (Garrett, 2017).

This model considers the effects of different loading conditions, volume fraction of inclusions, temperature, and different strengthening mechanisms like load transfer effect, Orowan looping effect, and thermal expansion mismatch effect on the ductility of CNT reinforced metal matrix composites. Moreover, the application of the proposed model does not require high-temperature microstructure measurements. By applying this model, several mechanical experiments are enough to provide the holistic properties of composites under different loading conditions, volume fraction of inclusions, and temperature which provide valuable guidance on new material development and product design.

7.2 Model Prediction for Cu/CNT Nano Composites

In this section, The strength and ductility of CNT reinforced copper composites are predicted and compared with experimental results published in Refs. (Jiapeng Liu et al., 2019; Jiapeng Liu et al., 2018) by implementing our temperature-dependent strength and ductility models (Eq. (55) and Eq. (67)).

Liu et al. (Jiapeng Liu et al., 2019; Jiapeng Liu et al., 2018) fabricated CNT reinforced copper nanocomposites by flake powder metallurgy and the CNTs are uniformly dispersed in the matrix which leads to a high strengthening effect. With the fabricated CNT reinforced cooper composites, they carried out uniaxial tension mechanical tests for CNT reinforced copper composites with different volume fractions of CNTs (0, 0.5vol.%, and 1vol.%) and under different testing

temperatures (293K, 573K, and 773K). The microstructural details are presented in Refs. (Jiapeng Liu et al., 2019; Jiapeng Liu et al., 2018). The true stress-strain data of related mechanical tests are shown in Figure 75.

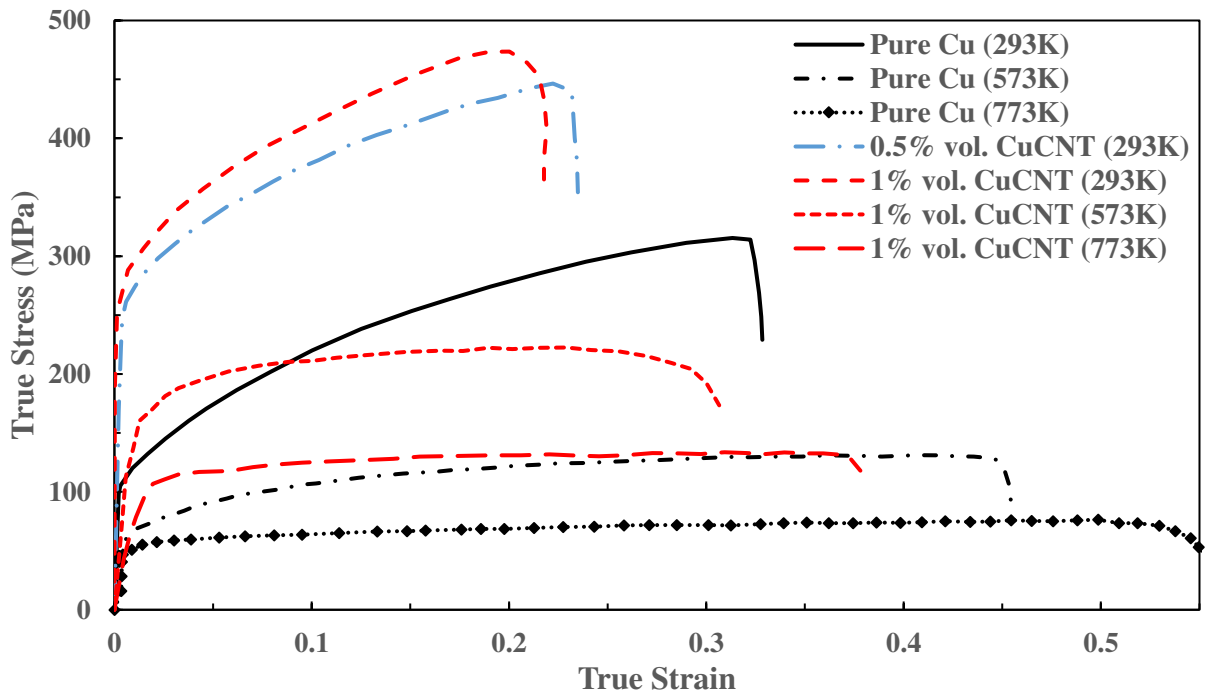

Figure 75. Tensile true stress-strain curves of the CNT reinforced copper composites with different volume fractions (0, 0.5 vol.%, and 1 vol.%)) of CNTs and under different testing temperatures (293K, 573K, and 773K) (Jiapeng Liu et al., 2019; Jiapeng Liu et al., 2018)

The material parameters of the composites and fabrication process parameters used during the calculation are listed in Table 19.

Table 19. Material parameters of CNT and copper, and the fabrication process parameters (Bai & Wierzbicki, 2008; Jiapeng Liu et al., 2019; Jiapeng Liu et al., 2018; Schelling & Keblinski, 2003; Shirasu et al., 2015)

Material parameters	Values
Shear modulus of copper (G_m)	$48\ GPa$
Burgers vector of copper (b)	$0.25563\ nm$
Thermal expansion coefficient of copper in room temperature (CTE_A)	$17 \times 10^{-6}\ K^{-1}$
Thermal expansion coefficient of CNT in room temperature (CTE_C)	$-0.9 \times 10^{-6}\ K^{-1}$
Diameter of CNT (d)	$20\ nm$
Maximum operating temperature (T_1)	$723\ K$
Minimum operating temperature (T_2)	$293\ K$
Melting temperature of copper (T_{melt})	$1358\ K$
Stress triaxiality of uniaxial tension (η)	$\frac{1}{3}$
Lode angle parameter of uniaxial tension ($\bar{\theta}$)	1

Regarding the calibration of the adjustable parameters, the values of a_1 and a_2 are determined by the room temperature testing results of different CNT reinforced composites (0, 0.5vol.% and 1vol.%). Then the parameter m can be obtained given the stress-strain data under different testing temperatures. As shown in Figure 75, compared to the specimens under high testing temperatures, there is much more strain hardening for the specimens under room temperature. To diminish the difference of the strain hardening for different temperatures, the average of initial yield stress and tensile strength is used as calibration data points for each specimen, and this average value is called "average yield stress" of corresponding composites thereafter for the sake of simplicity. The average stresses of different samples are shown in Table 20 and their values are normalized based on the room temperature average stresses. Then the parameter m is optimized based all the

experimental data. Figure 76 presents the temperature effect on the average yield stresses of different specimens under different testing temperatures and it shows that the material softening has been well captured by the proposed model.

Table 20. The average yield stresses of copper matrix composites with different volume fractions of CNT and under different temperatures before and after normalization

	$293\ K$	$593\ K$	$793\ K$
	Before normalization		
0 vol.% CNT	$208\ MPa$	$65\ MPa$	$57\ MPa$
1 vol.% CNT	$375\ MPa$	$140\ MPa$	$99\ MPa$
	After normalization		
0 vol.% CNT	$\frac{208}{208} = 1$	$\frac{65}{208} = 0.313$	$\frac{57}{208} = 0.274$
1 vol.% CNT	$\frac{375}{375} = 1$	$\frac{140}{375} = 0.373$	$\frac{99}{375} = 0.264$

With the values of a_1, a_2 and m obtained, the stress-strain curves for different CNT reinforced copper composites under different testing temperatures can be plotted. Figure 77 displays a comparison between experimental data and analytical solutions. It shows that strengthening analytical model can well capture the strengthening effects by the addition of CNTs as well as the thermal softening effect caused by elevated temperatures.

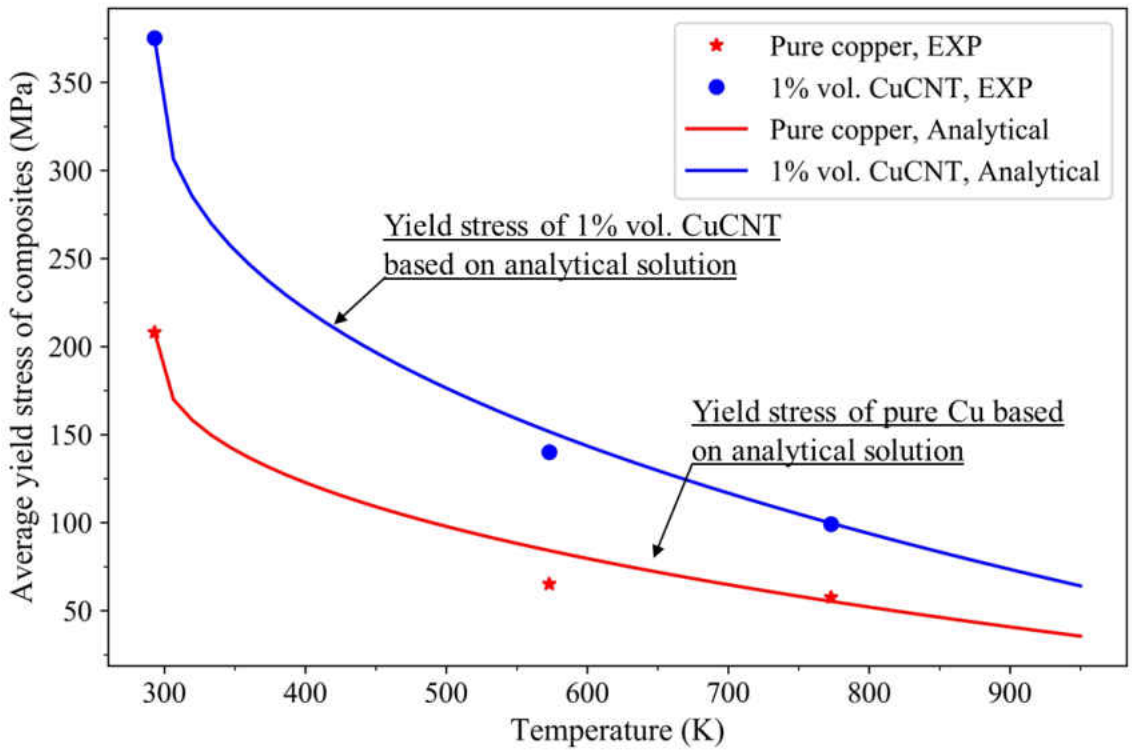

Figure 76. Temperature effects on the average yield stresses of different CNT reinforced copper composites.

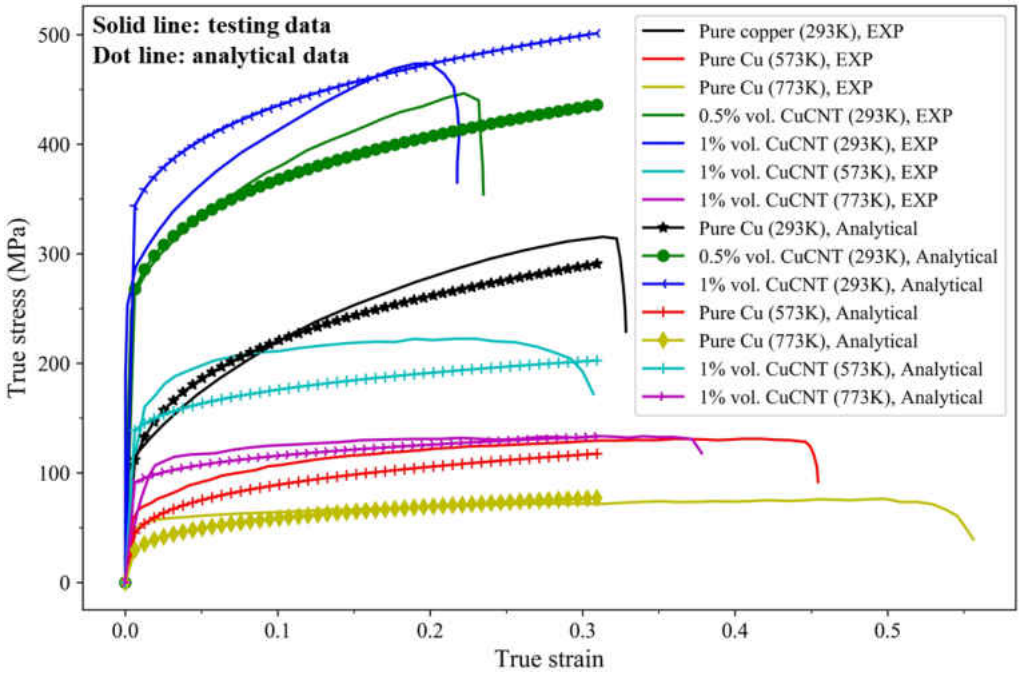

Figure 77. Comparison between experimental data and analytical solutions for CNT reinforced copper composites. A good correlation has been achieved for the strengthening effect. Note that ductility loss has not been considered here.

At last, the fracture strains (uniaxial tension as an example) of all the specimens can be obtained from the stress-strain curves, and these fracture strains values are used to determine the values of parameters A, n, c_1 and c_2. Since there is only one loading condition available, the global optimization of these four parameters is carried out. The predicted fracture strains by the proposed analytical model are displayed in Figure 78 and it shows great accuracy for the measured fracture strains. Furthermore, the analytical model further predicts the fracture strains for CNT reinforced copper composites with different volume fractions of inclusions and under different testing temperatures (which exceed testing ranges), and this can provide treasured guidance on the material design process.

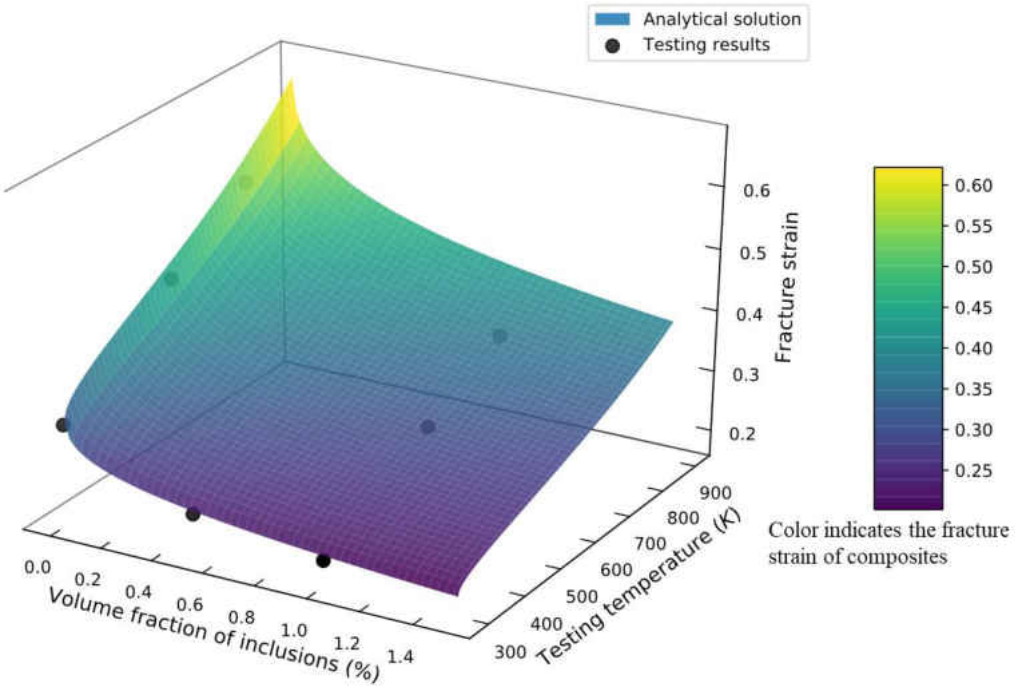

Figure 78. A comparison between experimental fracture strains (uniaxial tension) and analytical model predicted strains. The experimental data are presented with round dots and the analytical results are shown in the colored surface. A very good correlation is achieved between the experiment and the analytical model.

The model predicted fracture strains can also be marked on the stress-strain curves. Figure 79 demonstrates that there is a good correlation between the experimental results and the analytical model predictions for both the strengthening effects and ductility loss under different testing temperatures. The calibrated model parameters are listed in Table 21**.** The available tested loading condition was only uniaxial tension, but the MMC fracture model helps to predict the full 3D fracture locus under other complex loading conditions, for example, compression, shear, equi-biaxial tension, etc. Validated research on this subject can be found in (He et al., 2020)**.** Figure 80 presents the fracture locus in the 3D space based on the newly calibrated parameters.

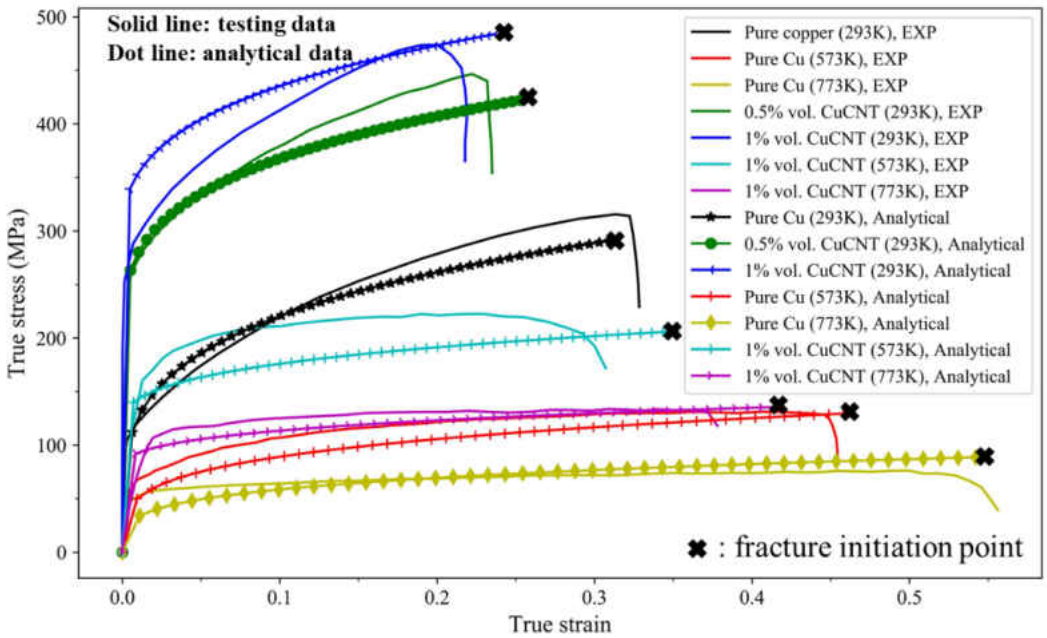

Figure 79. A comparison between the experimental data and the analytical predictions. Both the strengthening effect and ductility loss are well predicted by the proposed analytical models. The material softening which is caused by elevated temperature is also well captured.

Table 21. Calibrated parameter values for the strengthening analytical model and ductility loss analytical model of Cu/CNT composites.

Model Parameters	Values
a_1	0.08
a_2	0.85
m	0.34147
A	111.96
n	2.556
c_1	58.88
c_2	328.63

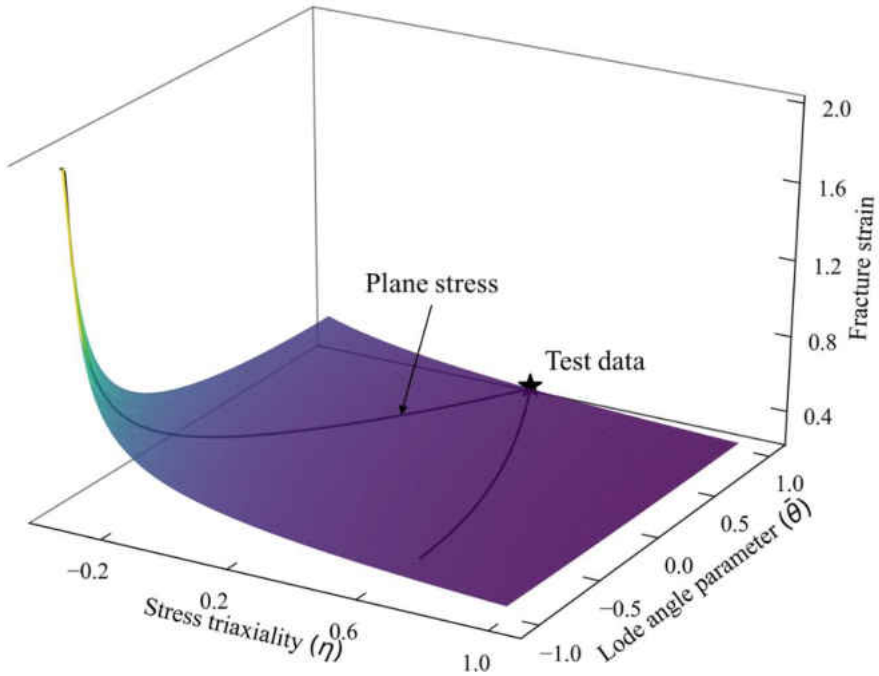

Figure 80. The multiaxial stress 3D fracture locus of Cu-0.5%vol. CNT composite under room temperature based on the calibrated ductility model.

7.3 Model Prediction for Al/NiCNT Nano Composites

As a second example, the ductility loss of Al/NiCNT nano composites, which was fabricated at the authors' lab recently, is predicted by the proposed analytical model in this section.

CNTs were purchased from Cheap Tubes Inc. with purity greater than 95% (CheapTubes). CNTs that were used had a diameter between 8-15 nm with an axial length between 10–50 µm. Al powder was purchased from Alfa Aesar with mesh size of -325 and purity of 99.8%. CNTs were first ultrasonically dispersed in an aqueous solution of HNO_3 (70%) at 80 °C for 2 hours for purification to remove all the impurities (Billah & Chen, 2017; Peng et al., 2007). HNO_3 treatment also alters surface properties for better dispersion in the electrolyte which is essential for the high-density activation sites formation in the subsequent reactions (B. Zhao et al., 2009). This process has great importance to improve the adherence of metallic particles to CNT surfaces. CNTs were then rinsed with deionized (DI) water. Each time, rinsing was continued until the solution was neutral. The

functionalized nanotubes were then coated with Ni in a two-step electroless nickel deposition process. At first, CNTs were ultrasonically dispersed in the electroless plating solution (Table 10) under ultra-violate (UV) exposure for 20 minutes, and then $NaBH_4$ solution was added to form the NiO clusters as the catalytic sites to activate the CNTs. Following washing CNTs with DI water, the activated CNTs were dispersed again into the plating solution at 50 ℃ for 20 minutes. Ammonia solution was used to adjusted pH to 8.5. Finally, the Ni-coated CNTs were cleaned with DI water, filtered off, and dried. Figure 81(a) shows an example of Ni-coated CNTs.

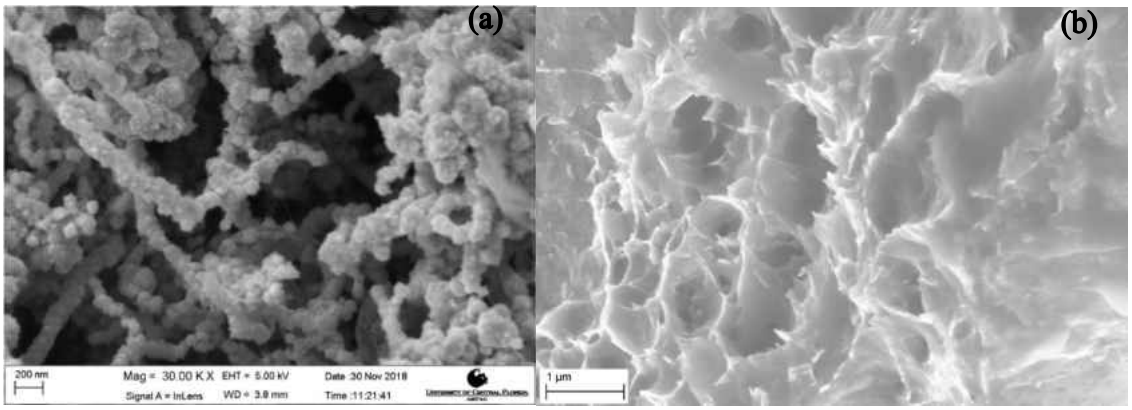

Figure 81 (a). An SEM image of Ni-coated CNTs. (b). An example of the fracture surface of Al/NiCNTs nanocomposites showing no interface debonding during loading. Dimples show material ductile fracture mode.

These Ni-coated CNTs were then ultra-sonicated for 2 hours in ethyl alcohol to avoid agglomeration. Later after adding Al powders, the mix was further ultra-sonicated for another 2 hours. Then the mixture was dried and pressed into a pellet of 13mm diameter under a unidirectional pressure of 400 MPa. All the pellets were sintered in the pure nitrogen atmosphere. Hot Isostatic Pressing (HIP) was further used for consolidation at 550 ℃ for 90 minutes at 200 MPa pressure.

The effects of Ni-coated CNTs addition on tensile strength were investigated using a Mechanical Testing and Simulation (MTS) Tytron 250 tensile test machine in the lab. Rectangular tensile

specimens were prepared according to ASTM E8/E8M–09. One example fracture surface of Al/NiCNT nano-composites is provided in Figure 81(b).

Table 22 Composition of Ni Plating Bath

$Chemicals$	$Concentration\ (g/L)$
$NiSO_4 \cdot 6H_2O$	8
NaH_2PO_2	35
$C_6H_5Na_3O_7$	18
$NH_3\ solution$	$For\ pH\ adjustment$

Different weight fractions of CNTs are used to investigate the strengthening effect. Typical results of calibrated true stress-strain curves for pure aluminum and two Al/NiCNT nanocomposites (0.5% wt. and 1% wt. of NiCNTs) are shown in Figure 82.

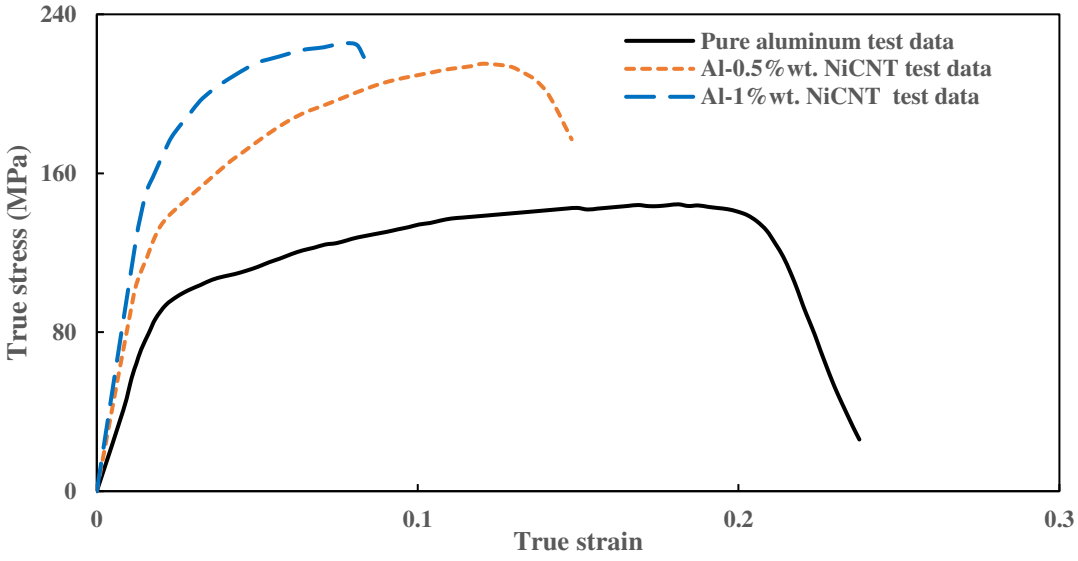

Figure 82 Calibrated true stress-strain curves of both pure aluminum and Al/NiCNTs with different weight fractions of NiCNTs

In this example, all experiments are carried out under room temperature, so the ductility equation of Eq. (67) can be simplified to Eq. (68). It's worth noting that the purpose of nickel addition is to

improve the dispersion of CNTs in the aluminum matrix, and to improve the interface between CNTs and metals. The volume fraction of the nickel is very limited. Thus, the influence of nickel on the strengthening is negligible and it is omitted in this analytical analysis. Following the same procedures of the above Cu/CNT example, the calibration can be done. First, based on the stress-strain data of pure aluminum and different CNT reinforced aluminum composites, the strengthening factors a_1 and a_2 are calibrated. Then given the fracture strains of each type of samples, the fracture model parameters are calibrated and presented in

Table 24. The comparison between experimental data and analytical model results is shown in Figure 83. One can see that the effect of NiCNT weight fraction is well captured. Again, the model is able to predict composite material's fracture strains under other complex loading conditions. For example, the 2D fracture locus under plane stress condition is plotted in Figure 84 even though there is only one available test data point.

$$\bar{\varepsilon} = \left\{ \frac{c_2}{A} \left[\sqrt{\frac{1+c_1^2}{3}} \cos\left(\frac{\bar{\theta}\pi}{6}\right) + c_1 \left(\eta + \frac{1}{3} \sin\left(\frac{\bar{\theta}\pi}{6}\right) \right) \right]^{-1} [(1+f_{load})(1+f_{Orowan})(1+f_{thermal})]^{-1} \right\}^{\frac{1}{n}} \quad (68)$$

Table 23. Material parameters of CNT and aluminum for the current case study, and the fabrication process parameters

Material parameters	Values
Shear modulus of aluminum (G_m)	$26\ GPa$
Burgers vector of copper (b)	$0.286\ nm$
Thermal expansion coefficient of copper in room temperature (CTE_A)	$23.1 \times 10^{-6}\ K^{-1}$
Thermal expansion coefficient of CNT in room temperature (CTE_C)	$-0.9 \times 10^{-6}\ K^{-1}$
Diameter of CNT (d)	$10\ nm$
Maximum operating temperature (T_1)	$823\ K$
Minimum operating temperature (T_2)	$293\ K$
Melting temperature of copper (T_{melt})	$933\ K$

Table 24. Calibrated parameters for the ductility analytical model of Al/NiCNT composites

Model Parameters	Values
a_1	0.408
a_2	0.105
A	221.89
n	2.53
c_1	20.7
c_2	71.24

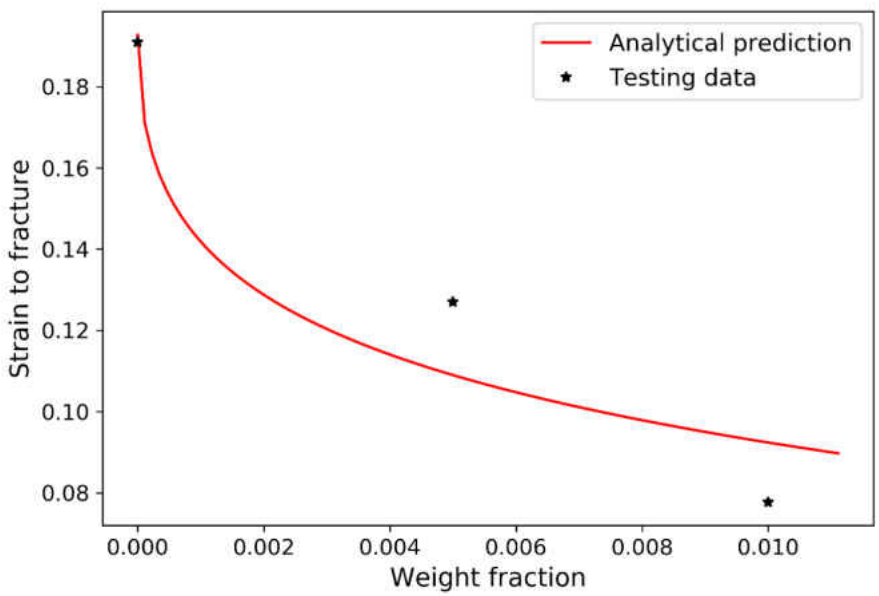

Figure 83. Comparison of fracture strain (uniaxial tension) between experimental data and analytical predictions for Al/NiCNT composites. The weight fraction means weight fraction of Ni coated CNTs.

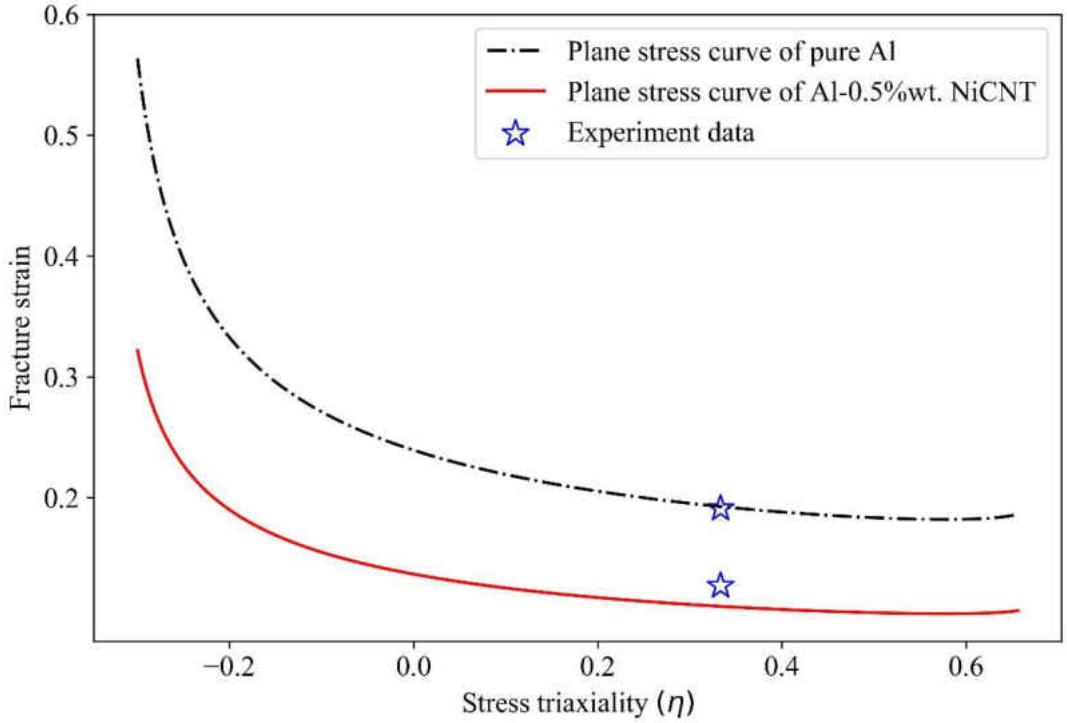

Figure 84. 2D fracture loci under plane stress condition of pure Al and Al-0.5%wt. NiCNT composites based on the calibrated analytical ductility model.

7.4 Summary

In this chapter, an analytical model that can predict the temperature-dependent strengthening effects for CNT reinforced metal matrix composites is proposed. This plastic model considers the strengthening effects of Orowan looping effect, thermal expansion mismatch effect, and load bearing effect. Combining the strengthening analytical model with sMMC ductile fracture model, an analytical model that can predict ductility loss of CNT reinforced metal matrix composites is then derived. This ductility loss analytical model also considers three strengthening effects (Orowan looping effect, thermal expansion mismatch effect, and load bearing effect) and the material softening effect by the temperature elevation. Additionally, this proposed ductility loss model takes the influence of different loading conditions (multiaxial stress states) into consideration. A good correlation has been obtained between the experimental data and model predictions. The proposed analytical models offer a new method to predict the temperature-

dependent material strength and ductility for CNT reinforced metal matrix composites, among which ductility loss has not been comprehensively investigated by analytical methods. By carrying out limited numbers of mechanical tests, the proposed models can help predict the strength and ductility of CNT reinforced metal matrix composites under different volume fractions of CNTs, under different temperatures, and different loading conditions (multiaxial stress states). These proposed analytical models can also be extended to other inclusion reinforced metal matrix composites, for example, graphene nanoplatelets or silicon carbide, and can provide valuable guidance on the material design which further saves costs and shorten the material development cycle.

CHAPTER 8 CONCLUSIONS AND FUTURE STUDIES

This dissertation provided a comprehensive study on the strength and ductility of CNT reinforced metallic composites which include experimental work, numerical simulations, and analytical solutions. The key contributions are summarized as follows:

- A comprehensive set of experiments have been carried out on pure copper to investigate the plasticity and ductility of pure copper under different loading conditions. The results show that pure copper has strong stress-state dependent plasticity and fracture properties. Though it has excellent ductility, its working hardening property is not strong. Copper-based CNT composites would be a good potential product for industrial applications.
- The strengthening mechanisms of CNT reinforced aluminum composites are investigated by both numerical method and analytical study. A good correlation between experiment, simulation, and analytical solutions has been achieved in terms of the plasticity property. Finite element analysis shows that volume fraction of interfacial hardened zone, hardened/residual plastic strain, and aspect ratios of carbon nanotubes have key influences on the strengthening of composites. The load bearing effect is taken into consideration by the aspect ratios of CNTs, and the Orowan effect and thermal expansion mismatch are considered mainly through the hardened zone volume fraction and hardened plastic strain. It is found that the aspect ratios of carbon nanotubes play the most important role in the strengthening of the composites. The composite strength can be well predicted with a set of appropriate model parameters.
- Digital workflow is proposed to numerically study the mechanical and thermal properties of CNT reinforced composites. A plug-in based on commercial finite element software Abaqus is generated and it automatically generates 3D representative volume element

which includes preprocessing, solving, and postprocessing. This tool considers the influences of aspect ratio, volume fraction, distribution pattern, and anisotropy of both inclusions and interface. Two case studies are also presented which show the accuracy of the proposed digital workflow.

- Based on the proposed digital workflow, a parametric study is then carried out to investigate the thermal conductivity of porous materials and composites by considering the influence of inclusion size, aspect ratio, orientation, and interfacial thermal resistance. This work also discussed the influence of thermal conductivity anisotropy of inclusions on the effective thermal conductivity of composites by the 3D RVE method which has not been done before. Spherical inclusions are used to investigate the effect of inclusion size, and cylindrical inclusions are deployed to explore the effects of inclusion aspect ratio, orientation, and interface property.
- This work also derived an analytical solution to solve the strength-ductility trade-off problems of CNT reinforced metal composites which offers a simple and easy-to-implement solution in the material design stage. The strength analytical solution combines the influences of Orowan looping effect, thermal mismatch effect, loading bearing effect, and temperature. Except for the aforementioned four influencing factors, the ductility solution also considers the influence of different stress states. A good correlation has been obtained between the experimental data and model predictions. The proposed analytical models offer a new method to predict the temperature-dependent material strength and ductility for CNT reinforced metal matrix composites.

The following topics are suggested for future studies.

- Analytical solution of strengthening mechanism of CNT reinforced composites. Gurson-type plasticity models (Gurson, 1977; Tvergaard, 1981, 1982; Tvergaard & Needleman, 1984) have been widely used for the modeling of porous materials. Similar to the Gurson model, the strengthening mechanism of CNT reinforced composites can also be studied. The only difference is that the inclusion will be stronger than the matrix, instead of assumed to be void.
- Extend the strength and ductility trade-off solution to other materials. In this work, it has been shown that the derived strength and ductility trade-off analytical solution can provide accurate results for CNT reinforced copper matrix composites and CNT reinforced aluminum matrix composites. Graphene nanoplate reinforced metal matrix composites and SiC reinforced aluminum matrix composites can also be investigated by the same method.
- Application of the strength and ductility trade-off solution (with temperature dependency) to extrusion simulation. The extrusion process is significantly affected by the temperature distribution in the workpiece and the stress state changes drastically during this process. The finite element analysis based on the provided strength and ductility trade-off solution could provide valuable insights and suggestions for better extrusion processes.
- Ductility study of copper-based composites with RVE method under different loading conditions. Material ductility is always one of the most important issues for engineering applications. It is more important for composites as the ductility will deteriorate with the addition of inclusions. RVE method provides a fast approach for such issue and the ductility study under different loading conditions can provide guidance on material design.

REFERENCES

Algarni, M., Bai, Y., & Choi, Y. (2015). A study of Inconel 718 dependency on stress triaxiality and Lode angle in plastic deformation and ductile fracture. *Engineering Fracture Mechanics, 147*, 140-157. doi:10.1016/j.engfracmech.2015.08.007

Amirbayat, J., & Hearle, J. (1969). Properties of unit composites as determined by the properties of the interface. Part I: Mechanism of matrix-fibre load transfer. *Fibre Science and Technology, 2*(2), 123-141.

An, L., Qu, J., Luo, J., Fan, Y., Zhang, L., Liu, J., . . . Blau, P. J. (2011). Aluminum nanocomposites having wear resistance better than stainless steel. *Journal of Materials Research, 26*(19), 2479-2483.

Ayer, R., Thirumalai, N. S., Jin, H.-W., Lillig, D. B., Fairchild, D. P., & Ford, S. J. (2014). High strength nickel alloy welds through strain hardening. In: Google Patents.

Bai, Y. (2007). Effect of loading history on necking and fracture. *PhD. Massachusetts Institute of Technology, Cambridge, USA*.

Bai, Y., & Atkins, T. (2012). Tension and shear cracking during indentation of ductile materials by opposed wedges. *Engineering Fracture Mechanics, 96*, 49-60. doi:10.1016/j.engfracmech.2012.06.014

Bai, Y., & Wierzbicki, T. (2008). A new model of metal plasticity and fracture with pressure and Lode dependence. *International Journal of Plasticity, 24*(6), 1071-1096. doi:10.1016/j.ijplas.2007.09.004

Bai, Y., & Wierzbicki, T. (2009). Application of extended Mohr–Coulomb criterion to ductile fracture. *International Journal of Fracture, 161*(1), 1-20. doi:10.1007/s10704-009-9422-8

Bai, Y., & Wierzbicki, T. (2015). A comparative study of three groups of ductile fracture loci in the 3D space. *Engineering Fracture Mechanics, 135*, 147-167. doi:10.1016/j.engfracmech.2014.12.023

Bailakanavar, M., Liu, Y., Fish, J., & Zheng, Y. (2012). Automated modeling of random inclusion composites. *Engineering with Computers, 30*(4), 609-625. doi:10.1007/s00366-012-0310-x

Bakshi, S. R., Lahiri, D., & Agarwal, A. (2013). Carbon nanotube reinforced metal matrix composites - a review. *International Materials Reviews, 55*(1), 41-64. doi:10.1179/095066009x12572530170543

Bakshi, S. R., Patel, R. R., & Agarwal, A. (2010). Thermal conductivity of carbon nanotube reinforced aluminum composites: A multi-scale study using object oriented finite element method. *Computational materials science, 50*(2), 419-428. doi:10.1016/j.commatsci.2010.08.034

Bao, Y., & Wierzbicki, T. (2004). On fracture locus in the equivalent strain and stress triaxiality space. *International Journal of Mechanical Sciences, 46*(1), 81-98. doi:10.1016/j.ijmecsci.2004.02.006

Barai, P., & Weng, G. J. (2011). A theory of plasticity for carbon nanotube reinforced composites. *International Journal of Plasticity, 27*(4), 539-559.

Bargmann, S., Klusemann, B., Markmann, J., Schnabel, J. E., Schneider, K., Soyarslan, C., & Wilmers, J. (2018). Generation of 3D representative volume elements for heterogeneous materials: A review. *Progress in Materials Science, 96*, 322-384. doi:10.1016/j.pmatsci.2018.02.003

Berber, S., Kwon, Y.-K., & Tománek, D. (2000). Unusually high thermal conductivity of carbon nanotubes. *Physical Review Letters, 84*(20), 4613.

Bhattacharyya, A., Rittel, D., & Ravichandran, G. (2005). Effect of strain rate on deformation texture in OFHC copper. *Scripta Materialia, 52*(7), 657-661. doi:10.1016/j.scriptamat.2004.11.019

Billah, M. M. (2017). *Carbon nanotube (CNT) metallic composite with focus on processing and the resultant properties.* (PhD). University of Central Florida, Electronic Theses and Dissertations. (5443.)

Billah, M. M., & Chen, Q. (2017). Thermal conductivity of Ni-coated MWCNT reinforced 70Sn-30Bi alloy. *Composites Part B: Engineering, 129*, 162-168.

Boey, F., & Lye, S. (1992). Void reduction in autoclave processing of thermoset composites: Part 1: High pressure effects on void reduction. *Composites, 23*(4), 261-265.

Böhm, H. J., Eckschlager, A., & Han, W. (2002). Multi-inclusion unit cell models for metal matrix composites with randomly oriented discontinuous reinforcements. *Computational materials science, 25*(1-2), 42-53.

Bridgman, P. W. (1952). *Studies in large plastic flow and fracture* (Vol. 177): McGraw-Hill New York.

Cao, C., Andrews, J. B., Kumar, A., & Franklin, A. D. (2016). Improving Contact Interfaces in Fully Printed Carbon Nanotube Thin-Film Transistors. *ACS Nano, 10*(5), 5221-5229. doi:10.1021/acsnano.6b00877

Cao, T.-S., Gachet, J.-M., Montmitonnet, P., & Bouchard, P.-O. (2014). A Lode-dependent enhanced Lemaitre model for ductile fracture prediction at low stress triaxiality. *Engineering Fracture Mechanics, 124*, 80-96.

Cao, T. S., Gachet, J. M., Montmitonnet, P., & Bouchard, P. O. (2014). A Lode-dependent enhanced Lemaitre model for ductile fracture prediction at low stress triaxiality. *Engineering Fracture Mechanics, 124-125*, 80-96. doi:10.1016/j.engfracmech.2014.03.021

Cazacu, O., & Barlat, F. (2004). A criterion for description of anisotropy and yield differential effects in pressure-insensitive metals. *International Journal of Plasticity, 20*(11), 2027-2045.

Cazacu, O., Plunkett, B., & Barlat, F. (2006). Orthotropic yield criterion for hexagonal closed packed metals. *International Journal of Plasticity, 22*(7), 1171-1194.

Cha, S. I., Kim, K. T., Arshad, S. N., Mo, C. B., & Hong, S. H. (2005). Extraordinary strengthening effect of carbon nanotubes in metal-matrix nanocomposites processed by molecular-level mixing. *Advanced Materials, 17*(11), 1377-1381. doi:10.1002/adma.200401933

Chai, G., Sun, Y., & Chen, Q. (2008). Mechanical properties of carbon nanotube–copper nanocomposites. *Journal of Micromechanics and Microengineering, 18*(3), 035013.

Che, J., Cagin, T., & Goddard III, W. A. (2000). Thermal conductivity of carbon nanotubes. *Nanotechnology, 11*(2), 65.

CheapTubes. Multi Walled Carbon Nanotubes 8-15nm. Retrieved from https://www.cheaptubes.com/product/multi-walled-carbon-nanotubes-8-15nm/

Chen, B., Kondoh, K., Li, J., & Qian, M. (2020). Extraordinary reinforcing effect of carbon nanotubes in aluminium matrix composites assisted by in-situ alumina nanoparticles. *Composites Part B: Engineering, 183*, 107691.

Chen, B., Li, S., Imai, H., Jia, L., Umeda, J., Takahashi, M., & Kondoh, K. (2015). Load transfer strengthening in carbon nanotubes reinforced metal matrix composites via in-situ tensile tests. *Composites Science and Technology, 113*, 1-8.

Chen, F., Ying, J., Wang, Y., Du, S., Liu, Z., & Huang, Q. (2016). Effects of graphene content on the microstructure and properties of copper matrix composites. *Carbon, 96*, 836-842.

Chen, Q., Chai, G., & Li, B. (2005). Exploration study of multifunctional metallic nanocomposite utilizing single-walled carbon nanotubes for micro/nano devices. *Proceedings of the Institution of Mechanical Engineers, Part N: Journal of Nanoengineering and Nanosystems, 219*(2), 67-72.

Cho, Y. J., Lee, W. J., & Park, Y. H. (2015). Effect of boundary conditions on plasticity and creep behavior analysis of particle reinforced composites by representative volume element approach. *Computational materials science, 100*, 67-75. doi:10.1016/j.commatsci.2014.11.036

Choi, H., Shin, J., & Bae, D. (2011). Grain size effect on the strengthening behavior of aluminum-based composites containing multi-walled carbon nanotubes. *Composites Science and Technology, 71*(15), 1699-1705.

Choi, H., Shin, J., Min, B., Park, J., & Bae, D. (2009). Reinforcing effects of carbon nanotubes in structural aluminum matrix nanocomposites. *Journal of Materials Research, 24*(8), 2610-2616.

Cöcen, Ü., & Önel, K. (2002). Ductility and strength of extruded SiCp/aluminium-alloy composites. *Composites Science and Technology, 62*(2), 275-282.

Coleman, J. N., Khan, U., Blau, W. J., & Gun'ko, Y. K. (2006). Small but strong: A review of the mechanical properties of carbon nanotube–polymer composites. *Carbon, 44*(9), 1624-1652. doi:10.1016/j.carbon.2006.02.038

Commission, I. E. (2007). Efficient electrical energy transmission and distribution. *Switzerland, IEC*.

contributors, W. (2019). Electrical wiring. Retrieved from https://en.wikipedia.org/w/index.php?title=Electrical_wiring&oldid=884141561

Daviran, S., Mohasseb, S., Kasaeian, A., & Mahian, O. (2017). Differential quadrature method for thermal shock analysis of CNT reinforced metal-ceramic functionally graded disc. *Composite Structures, 161*, 299-307. doi:10.1016/j.compstruct.2016.11.035

De Volder, M. F., Tawfick, S. H., Baughman, R. H., & Hart, A. J. (2013). Carbon nanotubes: present and future commercial applications. *Science, 339*(6119), 535-539.

Dong, S., Zhou, J., Hui, D., Wang, Y., & Zhang, S. (2015). Size dependent strengthening mechanisms in carbon nanotube reinforced metal matrix composites. *Composites Part A: Applied Science and Manufacturing, 68*, 356-364.

Drucker, D. C., & Prager, W. (1952). Soil mechanics and plastic analysis or limit design. *Quarterly of applied mathematics, 10*(2), 157-165.

Duan, W., Wang, Q., Liew, K. M., & He, X. (2007). Molecular mechanics modeling of carbon nanotube fracture. *Carbon, 45*(9), 1769-1776.

Dunand, M., & Mohr, D. (2011). On the predictive capabilities of the shear modified Gurson and the modified Mohr–Coulomb fracture models over a wide range of stress triaxialities and Lode angles. *Journal of the Mechanics and Physics of Solids, 59*(7), 1374-1394. doi:10.1016/j.jmps.2011.04.006

Duschlbauer, D., BÖhm, H. J., & Pettermann, H. E. (2006). Computational Simulation of Composites Reinforced by Planar Random Fibers: Homogenization and Localization by

Unit Cell and Mean Field Approaches. *Journal of Composite Materials, 40*(24), 2217-2234. doi:10.1177/0021998306062317

Ebbesen, T., Lezec, H., Hiura, H., Bennett, J., Ghaemi, H., & Thio, T. (1996). Electrical conductivity of individual carbon nanotubes. *Nature, 382*(6586), 54.

El Moumen, A., Kanit, T., Imad, A., & El Minor, H. (2015). Computational thermal conductivity in porous materials using homogenization techniques: Numerical and statistical approaches. *Computational materials science, 97*, 148-158. doi:10.1016/j.commatsci.2014.09.043

Emsley, J. (2011). *Nature's building blocks: an AZ guide to the elements*: Oxford University Press.

Engineeringtoolbox.com. (2017). Thermal Conductivities of Heat Exchanger Materials. Retrieved from https://www.engineeringtoolbox.com/heat-exchanger-material-thermal-conductivities-d_1488.html

Esawi, A., & Morsi, K. (2007). Dispersion of carbon nanotubes (CNTs) in aluminum powder. *Composites Part A: Applied Science and Manufacturing, 38*(2), 646-650.

Esawi, A. M. K., Morsi, K., Sayed, A., Taher, M., & Lanka, S. (2010). Effect of carbon nanotube (CNT) content on the mechanical properties of CNT-reinforced aluminium composites. *Composites Science and Technology, 70*(16), 2237-2241. doi:10.1016/j.compscitech.2010.05.004

Evans, J. W. (1993). Random and cooperative sequential adsorption. *Reviews of Modern Physics, 65*(4), 1281-1329. Retrieved from https://link.aps.org/doi/10.1103/RevModPhys.65.1281

Fan, G., Jiang, Y., Tan, Z., Guo, Q., Xiong, D.-b., Su, Y., . . . Zhang, D. (2018). Enhanced interfacial bonding and mechanical properties in CNT/Al composites fabricated by flake powder metallurgy. *Carbon, 130*, 333-339.

Fang, D., Qi, H., & Tu, S. (1996). Elastic and plastic properties of metal-matrix composites: geometrical effects of particles. *Computational materials science, 6*(4), 303-309.

Ferkel, H., & Mordike, B. (2001). Magnesium strengthened by SiC nanoparticles. *Materials Science and Engineering: A, 298*(1-2), 193-199.

Fu, S., Chen, X., & Liu, P. (2020). Preparation of CNTs/Cu composites with good electrical conductivity and excellent mechanical properties. *Materials Science and Engineering: A, 771*, 138656.

Fukuda, H., & Kawata, K. (1974). Stress and strain fields in short fibre-reinforced composites. *Fibre Science and Technology, 7*(2), 129-156.

Gao, X., Zhang, T., Hayden, M., & Roe, C. (2009). Effects of the stress state on plasticity and ductile failure of an aluminum 5083 alloy. *International Journal of Plasticity, 25*(12), 2366-2382.

Gao, X. L., & Li, K. (2005). A shear-lag model for carbon nanotube-reinforced polymer composites. *International Journal of Solids and Structures, 42*(5-6), 1649-1667. doi:10.1016/j.ijsolstr.2004.08.020

Garrett, A. (2017). Inspyred: A framework for creating bio-inspired computational intelligence algorithms in python. *Software available at https://aarongarrett. github. io/inspyred*.

George, R., Kashyap, K. T., Rahul, R., & Yamdagni, S. (2005). Strengthening in carbon nanotube/aluminium (CNT/Al) composites. *Scripta Materialia, 53*(10), 1159-1163. doi:10.1016/j.scriptamat.2005.07.022

Ghazali, S., Algarni, M., Bai, Y., & Choi, Y. (2020). A study on the plasticity and fracture of the AISI 4340 steel alloy under different loading conditions and considering heat-treatment effects. *International Journal of Fracture, 225*(1), 69-87.

Gong, Q.-m., Li, Z., Bai, X.-d., Li, D., Zhao, Y., & Liang, J. (2004). Thermal properties of aligned carbon nanotube/carbon nanocomposites. *Materials Science and Engineering: A, 384*(1-2), 209-214. doi:10.1016/j.msea.2004.06.006

Graebner, J., Jin, S., Kammlott, G., Herb, J., & Gardinier, C. (1992). Large anisotropic thermal conductivity in synthetic diamond films. *Nature, 359*(6394), 401.

Gruben, G., Hopperstad, O., & Børvik, T. (2012). Evaluation of uncoupled ductile fracture criteria for the dual-phase steel Docol 600DL. *International Journal of Mechanical Sciences, 62*(1), 133-146.

Gurson, A. L. (1977). Plastic flow and fracture behavior of ductile materials incorporating void nucleation, growth, and interaction.

Han, Z., & Fina, A. (2011). Thermal conductivity of carbon nanotubes and their polymer nanocomposites: a review. *Progress in Polymer Science, 36*(7), 914-944.

Hancock, J., & Brown, D. (1983). On the role of strain and stress state in ductile failure. *Journal of the Mechanics and Physics of Solids, 31*(1), 1-24.

Hancock, J., & Mackenzie, A. (1976). On the mechanisms of ductile failure in high-strength steels subjected to multi-axial stress-states. *Journal of the Mechanics and Physics of Solids, 24*(2-3), 147-160.

Hartmann, J., Voigt, P., Reichling, M., & Matthias, E. (1996). Photothermal measurement of thermal anisotropy in pyrolytic graphite. *Applied Physics B, 62*(5), 493-497.

Hasselman, D., & Johnson, L. F. (1987). Effective thermal conductivity of composites with interfacial thermal barrier resistance. *Journal of Composite Materials, 21*(6), 508-515.

He, X., Liu, J., & An, L. (2017). The mechanical behavior of hierarchical Mg matrix nanocomposite with high volume fraction reinforcement. *Materials Science and Engineering: A, 699*, 114-117.

He, X., Song, S., Luo, X., Liu, J., An, L., & Bai, Y. (2020). Predicting ductility of Mg/SiCp nanocomposite under multiaxial loading conditions based on unit cell modeling. *International Journal of Mechanical Sciences, 184*. doi:10.1016/j.ijmecsci.2020.105831

Hernández-Pérez, A., & Avilés, F. (2010). Modeling the influence of interphase on the elastic properties of carbon nanotube composites. *Computational materials science, 47*(4), 926-933. doi:10.1016/j.commatsci.2009.11.025

Hill, R. (1963). Elastic properties of reinforced solids: some theoretical principles. *Journal of the Mechanics and Physics of Solids, 11*(5), 357-372.

Hone, J., Whitney, M., Piskoti, C., & Zettl, A. (1999). Thermal conductivity of single-walled carbon nanotubes. *Physical Review B, 59*(4), R2514.

Hsueh, C.-H. (2000). Young's modulus of unidirectional discontinuous-fibre composites. *Composites Science and Technology, 60*(14), 2671-2680.

Hwang, J., Yoon, T., Jin, S. H., Lee, J., Kim, T. S., Hong, S. H., & Jeon, S. (2013). Enhanced mechanical properties of graphene/copper nanocomposites using a molecular‐level mixing process. *Advanced Materials, 25*(46), 6724-6729.

Iijima, S. (1991). Synthesis of carbon nanotubes. *Nature, 354*(6348), 56-58.

Imani Yengejeh, S., Kazemi, S. A., & Öchsner, A. (2017). Carbon nanotubes as reinforcement in composites: A review of the analytical, numerical and experimental approaches. *Computational materials science, 136*, 85-101. doi:10.1016/j.commatsci.2017.04.023

Jia, Y., & Bai, Y. (2016). Experimental study on the mechanical properties of AZ31B-H24 magnesium alloy sheets under various loading conditions. *International Journal of Fracture, 197*(1), 25-48.

Jiajun, W., & Xiao-Su, Y. (2004). Effects of interfacial thermal barrier resistance and particle shape and size on the thermal conductivity of AlN/PI composites. *Composites Science and Technology, 64*(10-11), 1623-1628.

Jiang, L.-l., Xu, G.-d., Cheng, S., Lu, X.-m., & Zeng, T. (2014). Predicting the thermal conductivity and temperature distribution in 3D braided composites. *Composite Structures, 108*, 578-583. doi:10.1016/j.compstruct.2013.09.030

Jiang, L., Li, Z., Fan, G., Cao, L., & Zhang, D. (2012). Strong and ductile carbon nanotube/aluminum bulk nanolaminated composites with two-dimensional alignment of carbon nanotubes. *Scripta Materialia, 66*(6), 331-334.

Johnson, G. R. (1983). A constitutive model and data for materials subjected to large strains, high strain rates, and high temperatures. *Proc. 7th Inf. Sympo. Ballistics*, 541-547.

Johnson, G. R., & Cook, W. H. (1985). Fracture characteristics of three metals subjected to various strains, strain rates, temperatures and pressures. *Engineering fracture mechanics, 21*(1), 31-48.

Kanit, T., Forest, S., Galliet, I., Mounoury, V., & Jeulin, D. (2003). Determination of the size of the representative volume element for random composites: statistical and numerical approach. *International Journal of Solids and Structures, 40*(13-14), 3647-3679. doi:10.1016/s0020-7683(03)00143-4

Kari, S., Berger, H., & Gabbert, U. (2007). Numerical evaluation of effective material properties of randomly distributed short cylindrical fibre composites. *Computational materials science, 39*(1), 198-204. doi:10.1016/j.commatsci.2006.02.024

Kari, S., Berger, H., Rodriguez-Ramos, R., & Gabbert, U. (2007). Computational evaluation of effective material properties of composites reinforced by randomly distributed spherical particles. *Composite Structures, 77*(2), 223-231.

Kassem, G. A. (2009). *Micromechanical Material Models For Polymer Composites Through Advanced Numerical Simulation Techniques.* (PhD). RWTH Aachen University, Retrieved from http://publications.rwth-aachen.de/record/51389/files/3230.pdf

Kim, W. J., Lee, T. J., & Han, S. H. (2014). Multi-layer graphene/copper composites: Preparation using high-ratio differential speed rolling, microstructure and mechanical properties. *Carbon, 69*, 55-65. doi:10.1016/j.carbon.2013.11.058

Kurzepa, L., Lekawa‐Raus, A., Patmore, J., & Koziol, K. (2014). Replacing copper wires with carbon nanotube wires in electrical transformers. *Advanced Functional Materials, 24*(5), 619-624.

Kwon, H., Estili, M., Takagi, K., Miyazaki, T., & Kawasaki, A. (2009). Combination of hot extrusion and spark plasma sintering for producing carbon nanotube reinforced aluminum matrix composites. *Carbon, 47*(3), 570-577. doi:10.1016/j.carbon.2008.10.041

Kwon, H., & Leparoux, M. (2012). Hot extruded carbon nanotube reinforced aluminum matrix composite materials. *Nanotechnology, 23*(41), 415701.

Laborde-Lahoz, P., Maser, W., Martínez, T., Benito, A., Seeger, T., Cano, P., . . . Miravete, A. (2005). Mechanical characterization of carbon nanotube composite materials. *Mechanics of Advanced Materials and Structures, 12*(1), 13-19. doi:10.1080/15376490590491792

Lennon, A., & Ramesh, K. (2004). The influence of crystal structure on the dynamic behavior of materials at high temperatures. *International Journal of Plasticity, 20*(2), 269-290.

Li, P., Chen, T., & Qin, H. (2017). The microstructure and mechanical properties of Al2024-SiC p composite fabricated by powder thixoforming. *Journal of Materials Research, 32*(11), 2079-2091.

Li, Q., Viereckl, A., Rottmair, C. A., & Singer, R. F. (2009). Improved processing of carbon nanotube/magnesium alloy composites. *Composites Science and Technology, 69*(7-8), 1193-1199. doi:10.1016/j.compscitech.2009.02.020

Li, X., Fan, X., Zhu, Y., Li, J., Adams, J. M., Shen, S., & Li, H. (2012). Computational modeling and evaluation of the thermal behavior of randomly distributed single-walled carbon nanotube/polymer composites. *Computational materials science, 63*, 207-213. doi:10.1016/j.commatsci.2012.06.034

Li, Y., & Wierzbicki, T. (2010). Prediction of plane strain fracture of AHSS sheets with post-initiation softening. *International Journal of Solids and Structures, 47*(17), 2316-2327. doi:10.1016/j.ijsolstr.2010.04.028

Liew, K. M., He, X. Q., & Wong, C. H. (2004). On the study of elastic and plastic properties of multi-walled carbon nanotubes under axial tension using molecular dynamics simulation. *Acta Materialia, 52*(9), 2521-2527. doi:10.1016/j.actamat.2004.01.043

Liu, J., Fan, G., Tan, Z., Guo, Q., Su, Y., Li, Z., & Xiong, D.-B. (2019). Mechanical properties and failure mechanisms at high temperature in carbon nanotube reinforced copper matrix nanolaminated composite. *Composites Part A: Applied Science and Manufacturing, 116*, 54-61. doi:10.1016/j.compositesa.2018.10.022

Liu, J., Xiong, D.-B., Tan, Z., Fan, G., Guo, Q., Su, Y., . . . Zhang, D. (2018). Enhanced mechanical properties and high electrical conductivity in multiwalled carbon nanotubes reinforced copper matrix nanolaminated composites. *Materials Science and Engineering: A, 729*, 452-457.

Liu, J., Zhao, K., Zhang, M., Wang, Y., & An, L. (2015). High performance heterogeneous magnesium-based nanocomposite. *Materials Letters, 143*, 287-289.

Liu, Y., & Chen, X. (2003). Evaluations of the effective material properties of carbon nanotube-based composites using a nanoscale representative volume element. *Mechanics of Materials, 35*(1-2), 69-81.

Liu, Z., Xiao, B., Wang, W., & Ma, Z. (2017). Modelling of carbon nanotube dispersion and strengthening mechanisms in Al matrix composites prepared by high energy ball milling-powder metallurgy method. *Composites Part A: Applied Science and Manufacturing, 94*, 189-198.

Llorca, J., Needleman, A., & Suresh, S. (1991). An analysis of the effects of matrix void growth on deformation and ductility in metal-ceramic composites. *Acta Metallurgica et Materialia, 39*(10), 2317-2335.

Long, X., Bai, Y., Algarni, M., Choi, Y., & Chen, Q. (2015). Study on the strengthening mechanisms of Cu/CNT nano-composites. *Materials Science and Engineering: A, 645*, 347-356. doi:10.1016/j.msea.2015.08.012

Lu, T., & Chen, C. (1999). Thermal transport and fire retardance properties of cellular aluminium alloys. *Acta Materialia, 47*(5), 1469-1485.

Luo, M., Dunand, M., & Mohr, D. (2012). Experiments and modeling of anisotropic aluminum extrusions under multi-axial loading – Part II: Ductile fracture. *International Journal of Plasticity, 32-33*, 36-58. doi:10.1016/j.ijplas.2011.11.001

Ma, Z., Guo, Z., Zhang, H., & Chang, T. (2017). Extremely high thermal conductivity anisotropy of double-walled carbon nanotubes. *AIP Advances, 7*(6), 065104.

Maghsoudlou, M. A., Barbaz Isfahani, R., Saber-Samandari, S., & Sadighi, M. (2019). Effect of interphase, curvature and agglomeration of SWCNTs on mechanical properties of polymer-based nanocomposites: Experimental and numerical investigations. *Composites Part B: Engineering, 175*. doi:10.1016/j.compositesb.2019.107119

Maxwell, J. C. (1881). *A treatise on electricity and magnetism* (Vol. 1): Clarendon press.

Mayandi, K., & Jeyaraj, P. (2015). Bending, buckling and free vibration characteristics of FG-CNT-reinforced polymer composite beam under non-uniform thermal load. *Proceedings of the Institution of Mechanical Engineers, Part L: Journal of Materials: Design and Applications, 229*(1), 13-28.

McClintock, F. (1968). A Criterion for Ductile Fracture by the Growth of Holes. *Journal of Applied Mechanics, 35*, 363-371.

McClintock, F. A. (1968). A criterion for ductile fracture by the growth of holes. *Journal of applied mechanics, 35*(2), 363-371.

Melro, A., Camanho, P., & Pinho, S. (2008). Generation of random distribution of fibres in long-fibre reinforced composites. *Composites Science and Technology, 68*(9), 2092-2102.

Meyers, M. A., Andrade, U. R., & Chokshi, A. H. (1995). The effect of grain size on the high-strain, high-strain-rate behavior of copper. *Metallurgical and materials transactions A, 26*(11), 2881-2893.

Mishra, A., Martin, M., Thadhani, N., Kad, B., Kenik, E. A., & Meyers, M. (2008). High-strain-rate response of ultra-fine-grained copper. *Acta Materialia, 56*(12), 2770-2783.

Mokdad, F., Chen, D. L., Liu, Z. Y., Xiao, B. L., Ni, D. R., & Ma, Z. Y. (2016). Deformation and strengthening mechanisms of a carbon nanotube reinforced aluminum composite. *Carbon, 104*, 64-77. doi:10.1016/j.carbon.2016.03.038

Nabovati, A., Llewellin, E. W., & Sousa, A. C. M. (2009). A general model for the permeability of fibrous porous media based on fluid flow simulations using the lattice Boltzmann method. *Composites Part A: Applied Science and Manufacturing, 40*(6-7), 860-869. doi:10.1016/j.compositesa.2009.04.009

Nahshon, K., & Hutchinson, J. (2008). Modification of the Gurson model for shear failure. *European journal of mechanics. A, Solids, 27*(1), 1.

Nairn, J. A. (2011). Aspect ratio requirements for nanotube-reinforced, polymer–matrix composites. *Composites Part A: Applied Science and Manufacturing, 42*(11), 1850-1855. doi:10.1016/j.compositesa.2011.08.012

Nakayama, Y. (2007). Plasticity of carbon nanotubes: aiming at their use in nanosized devices. *Japanese Journal of Applied Physics, 46*(8R), 5005.

Namilae, S., & Chandra, N. (2005). Multiscale model to study the effect of interfaces in carbon nanotube-based composites. *Journal of Engineering Materials and Technology, 127*(2), 222-232.

Nan, C.-W., Birringer, R., Clarke, D. R., & Gleiter, H. (1997). Effective thermal conductivity of particulate composites with interfacial thermal resistance. *Journal of Applied Physics, 81*(10), 6692-6699. doi:10.1063/1.365209

Nan, C. W., Shi, Z., & Lin, Y. (2003). A simple model for thermal conductivity of carbon nanotube-based composites. *Chemical Physics Letters, 375*(5-6), 666-669. doi:10.1016/s0009-2614(03)00956-4

Ni, Z., Bu, H., Zou, M., Yi, H., Bi, K., & Chen, Y. (2010). Anisotropic mechanical properties of graphene sheets from molecular dynamics. *Physica B: Condensed Matter, 405*(5), 1301-1306.

Nie, K., Deng, K., Wang, X., & Wu, K. (2017). Characterization and strengthening mechanism of SiC nanoparticles reinforced magnesium matrix composite fabricated by ultrasonic vibration assisted squeeze casting. *Journal of Materials Research, 32*(13), 2609-2620.

Omairey, S. L., Dunning, P. D., & Sriramula, S. (2018). Development of an ABAQUS plugin tool for periodic RVE homogenisation. *Engineering with Computers, 35*(2), 567-577. doi:10.1007/s00366-018-0616-4

Ondracek, G., & Schulz, B. (1973). The porosity dependence of the thermal conductivity for nuclear fuels. *Journal of Nuclear Materials, 46*(3), 253-258.

Ordonez-Miranda, J., & Alvarado-Gil, J. J. (2012). Effect of the pore shape on the thermal conductivity of porous media. *Journal of Materials Science, 47*(18), 6733-6740. doi:10.1007/s10853-012-6616-7

Palaci, I., Fedrigo, S., Brune, H., Klinke, C., Chen, M., & Riedo, E. (2005). Radial elasticity of multiwalled carbon nanotubes. *Physical Review Letters, 94*(17), 175502. doi:10.1103/PhysRevLett.94.175502

Pan, Y., Iorga, L., & Pelegri, A. A. (2008). Analysis of 3D random chopped fiber reinforced composites using FEM and random sequential adsorption. *Computational materials science, 43*(3), 450-461. doi:10.1016/j.commatsci.2007.12.016

Park, T., Dillard, D. A., & Ward, T. C. (2000). Anisotropy in the thermal shrinkage of polyimide film. *Journal of Polymer Science Part B: Polymer Physics, 38*(24), 3222-3229.

Peng, Y., Hu, Y., & Wang, H. (2007). Tribological behaviors of surfactant-functionalized carbon nanotubes as lubricant additive in water. *Tribology Letters, 25*(3), 247-253.

Pop, E., Varshney, V., & Roy, A. K. (2012). Thermal properties of graphene: Fundamentals and applications. *MRS Bulletin, 37*(12), 1273-1281.

Qian, D., Dickey, E. C., Andrews, R., & Rantell, T. (2000). Load transfer and deformation mechanisms in carbon nanotube-polystyrene composites. *Applied Physics Letters, 76*(20), 2868-2870.

Qiao, Y., Liu, J., Jia, Y., Xu, C., An, L., & Bai, Y. (2016). Study on coexistence of brittle and ductile fractures in nano reinforcement composites under different loading conditions. *International Journal of Fracture, 204*(2), 205-224. doi:10.1007/s10704-016-0174-y

Reddy, M. P., Shakoor, R., Parande, G., Manakari, V., Ubaid, F., Mohamed, A., & Gupta, M. (2017). Enhanced performance of nano-sized SiC reinforced Al metal matrix nanocomposites synthesized through microwave sintering and hot extrusion techniques. *Progress in Natural Science: Materials International, 27*(5), 606-614.

Riaño, L., & Joliff, Y. (2019). An Abaqus™ plug-in for the geometry generation of Representative Volume Elements with randomly distributed fibers and interphases. *Composite Structures, 209*, 644-651. doi:10.1016/j.compstruct.2018.10.096

Rice, J. R., & Tracey, D. M. (1969). On the ductile enlargement of voids in triaxial stress fields∗. *Journal of the Mechanics and Physics of Solids, 17*(3), 201-217.

Richmond, O., & Spitzig, W. (1980). Pressure dependence and dilatancy of plastic flow. *Theoretical and applied mechanics*, 377-386.

Rittel, D., Ravichandran, G., & Lee, S. (2002). Large strain constitutive behavior of OFHC copper over a wide range of strain rates using the shear compression specimen. *Mechanics of Materials, 34*(10), 627-642.

Saber - Samandari, S., & Afaghi - Khatibi, A. (2007). Evaluation of elastic modulus of polymer matrix nanocomposites. *Polymer Composites, 28*(3), 405-411.

Salvetat, J.-P., Bonard, J.-M., Thomson, N., Kulik, A., Forro, L., Benoit, W., & Zuppiroli, L. (1999). Mechanical properties of carbon nanotubes. *Applied Physics A, 69*(3), 255-260.

Saoudi, T., El-Moumen, A., Kanit, T., Belouchrani, M. E. A., Benseddiq, N., & Imad, A. (2020). Numerical Evaluation of the Thermal Properties of UD-Fibers Reinforced Composites for Different Morphologies. *International Journal of Applied Mechanics*, 2050032.

Saravanan, R., & Surappa, M. (2000). Fabrication and characterisation of pure magnesium-30 vol.% SiCP particle composite. *Materials Science and Engineering: A, 276*(1-2), 108-116.

Schelling, P., & Keblinski, P. (2003). Thermal expansion of carbon structures. *Physical Review B, 68*(3), 035425.

Seidel, G. D., & Lagoudas, D. C. (2006). Micromechanical analysis of the effective elastic properties of carbon nanotube reinforced composites. *Mechanics of Materials, 38*(8-10), 884-907. doi:10.1016/j.mechmat.2005.06.029

Sharma, N. K., Misra, R., & Sharma, S. (2017). Finite element modeling of effective thermomechanical properties of Al–B 4 C metal matrix composites. *Journal of materials science, 52*(3), 1416-1431.

She, W., Zhao, G., Cai, D., Jiang, J., & Cao, X. (2018). Numerical study on the effect of pore shapes on the thermal behaviors of cellular concrete. *Construction and Building Materials, 163*, 113-121. doi:10.1016/j.conbuildmat.2017.12.108

Shi, X. L., Yang, H., Shao, G. Q., Duan, X. L., Yan, L., Xiong, Z., & Sun, P. (2007). Fabrication and properties of W–Cu alloy reinforced by multi-walled carbon nanotubes. *Materials Science and Engineering: A, 457*(1-2), 18-23. doi:10.1016/j.msea.2006.12.038

Shin, S., Choi, H., Shin, J., & Bae, D. (2015). Strengthening behavior of few-layered graphene/aluminum composites. *Carbon, 82*, 143-151.

Shirasu, K., Yamamoto, G., Tamaki, I., Ogasawara, T., Shimamura, Y., Inoue, Y., & Hashida, T. (2015). Negative axial thermal expansion coefficient of carbon nanotubes: Experimental determination based on measurements of coefficient of thermal expansion for aligned carbon nanotube reinforced epoxy composites. *Carbon, 95*, 904-909.

Shokrieh, M., & Rafiee, R. (2010). A review of the mechanical properties of isolated carbon nanotubes and carbon nanotube composites. *Mechanics of Composite Materials, 46*(2), 155-172.

Simulia, D. (2017). Abaqus 2017, Documentation.

Smalc, M., Shives, G., Chen, G., Guggari, S., Norley, J., & Reynolds, R. A. (2005). *Thermal performance of natural graphite heat spreaders.* Paper presented at the ASME 2005 Pacific Rim Technical Conference and Exhibition on Integration and Packaging of MEMS, NEMS, and Electronic Systems collocated with the ASME 2005 Heat Transfer Summer Conference.

So, K. P., Kushima, A., Park, J. G., Liu, X., Keum, D. H., Jeong, H. Y., . . . Lee, Y. H. (2018). Intragranular Dispersion of Carbon Nanotubes Comprehensively Improves Aluminum Alloys. *Adv Sci (Weinh), 5*(7), 1800115. doi:10.1002/advs.201800115

Solórzano, E., Reglero, J. A., Rodríguez-Pérez, M. A., Lehmhus, D., Wichmann, M., & de Saja, J. A. (2008). An experimental study on the thermal conductivity of aluminium foams by using the transient plane source method. *International Journal of Heat and Mass Transfer, 51*(25-26), 6259-6267. doi:10.1016/j.ijheatmasstransfer.2007.11.062

Song, S., Billah, M., Zhou, Q., Ren, L., Zheng, L., Chen, Q., & Bai, Y. (2020). Study on Plastic Strengthening Mechanisms of Aluminum Matrix Nano-Composites Reinforced by Nickel Coated CNTs. *Composite Interfaces*, 1-22. doi:10.1080/09276440.2020.1844528

Spitzig, W., & Richmond, O. (1984). The effect of pressure on the flow stress of metals. *Acta Metallurgica, 32*(3), 457-463.

Subramaniam, C., Yamada, T., Kobashi, K., Sekiguchi, A., Futaba, D. N., Yumura, M., & Hata, K. (2013). One hundred fold increase in current carrying capacity in a carbon nanotube-copper composite. *Nat Commun, 4*, 2202. doi:10.1038/ncomms3202

Suh, Y. S., Joshi, S. P., & Ramesh, K. T. (2009). An enhanced continuum model for size-dependent strengthening and failure of particle-reinforced composites. *Acta Materialia, 57*(19), 5848-5861. doi:10.1016/j.actamat.2009.08.010

Sun, C., & Vaidya, R. (1996). Prediction of composite properties from a representative volume element. *Composites Science and Technology, 56*(2), 171-179.

Sunday, D. Distance between 3D lines & segments. *Geometry algorithms home.* Retrieved from http://geomalgorithms.com/a07-_distance.html

Swartz, E. T., & Pohl, R. O. (1989). Thermal boundary resistance. *Reviews of Modern Physics, 61*(3), 605-668. doi:10.1103/RevModPhys.61.605

Systèmes, D. (2008). Abaqus Scripting User's Manual. *Providence, RI, USA*.

Systèmes, D. (2012). Abaqus documentation. *Abaqus Inc*.

Tandon, G. P., & Weng, G. J. (1984). The effect of aspect ratio of inclusions on the elastic properties of unidirectionally aligned composites. *Polymer Composites, 5*(4), 327-333.

Tanner, A. B., McGinty, R. D., & McDowell, D. L. (1999). Modeling temperature and strain rate history effects in OFHC Cu. *International Journal of Plasticity, 15*(6), 575-603.

Tchalla, A., Belouettar, S., Makradi, A., & Zahrouni, H. (2013). An ABAQUS toolbox for multiscale finite element computation. *Composites Part B: Engineering, 52*, 323-333. doi:10.1016/j.compositesb.2013.04.028

Thostenson, E. T., Ren, Z., & Chou, T.-W. (2001). Advances in the science and technology of carbon nanotubes and their composites: a review. *Composites Science and Technology, 61*(13), 1899-1912.

Treacy, M. J., Ebbesen, T., & Gibson, J. (1996). Exceptionally high Young's modulus observed for individual carbon nanotubes. *Nature, 381*(6584), 678.

Tsai, J.-L., & Lu, T.-C. (2009). Investigating the load transfer efficiency in carbon nanotubes reinforced nanocomposites. *Composite Structures, 90*(2), 172-179.

Tserpes, K. I., & Chanteli, A. (2013). Parametric numerical evaluation of the effective elastic properties of carbon nanotube-reinforced polymers. *Composite Structures, 99*, 366-374. doi:10.1016/j.compstruct.2012.12.004

Tvergaard, V. (1981). Influence of voids on shear band instabilities under plane strain conditions. *International Journal of Fracture, 17*(4), 389-407.

Tvergaard, V. (1982). On localization in ductile materials containing spherical voids. *International Journal of Fracture, 18*(4), 237-252.

Tvergaard, V., & Needleman, A. (1984). Analysis of the cup-cone fracture in a round tensile bar. *Acta Metallurgica, 32*(1), 157-169.

Wang, D., Song, P., Liu, C., Wu, W., & Fan, S. (2008). Highly oriented carbon nanotube papers made of aligned carbon nanotubes. *Nanotechnology, 19*(7), 075609. doi:10.1088/0957-4484/19/7/075609

Wang, H., Zhang, Z.-H., Hu, Z.-Y., Song, Q., Yin, S.-P., Kang, Z., & Li, S.-L. (2018). Improvement of interfacial interaction and mechanical properties in copper matrix composites reinforced with copper coated carbon nanotubes. *Materials Science and Engineering: A, 715*, 163-173.

Wang, Y., Wu, J., & Wei, F. (2003). A treatment method to give separated multi-walled carbon nanotubes with high purity, high crystallization and a large aspect ratio. *Carbon, 41*(15), 2939-2948. doi:10.1016/S0008-6223(03)00390-7

Wang, Z., Kulkarni, A., Deshpande, S., Nakamura, T., & Herman, H. (2003). Effects of pores and interfaces on effective properties of plasma sprayed zirconia coatings. *Acta Materialia, 51*(18), 5319-5334. doi:10.1016/s1359-6454(03)00390-2

Weng, G. (1984). Some elastic properties of reinforced solids, with special reference to isotropic ones containing spherical inclusions. *International Journal of Engineering Science, 22*(7), 845-856.

Williams, S. R., & Philipse, A. P. (2003). Random packings of spheres and spherocylinders simulated by mechanical contraction. *Phys Rev E Stat Nonlin Soft Matter Phys, 67*(5 Pt 1), 051301. doi:10.1103/PhysRevE.67.051301

Xu, R., Tan, Z., Xiong, D., Fan, G., Guo, Q., Zhang, J., . . . Zhang, D. (2017). Balanced strength and ductility in CNT/Al composites achieved by flake powder metallurgy via shift-speed ball milling. *Composites Part A: Applied Science and Manufacturing, 96*, 57-66.

Xue, L. (2008). Constitutive modeling of void shearing effect in ductile fracture of porous materials. *Engineering Fracture Mechanics, 75*(11), 3343-3366.

Xue, Q. Z. (2005). Model for thermal conductivity of carbon nanotube-based composites. *Physica B: Condensed Matter, 368*(1-4), 302-307. doi:10.1016/j.physb.2005.07.024

Yang, D. J., Zhang, Q., Chen, G., Yoon, S. F., Ahn, J., Wang, S. G., . . . Li, J. Q. (2002). Thermal conductivity of multiwalled carbon nanotubes. *Physical Review B, 66*(16). doi:ARTN 165440
10.1103/PhysRevB.66.165440

Yang, X., Lu, T., & Kim, T. (2013). Effective Thermal Conductivity Modelling for Closed-Cell Porous Media with Analytical Shape Factors. *Transport in Porous Media, 100*(2), 211-224. doi:10.1007/s11242-013-0212-4

Yengejeh, S. I., Kazemi, S. A., & Öchsner, A. (2017). Carbon nanotubes as reinforcement in composites: a review of the analytical, numerical and experimental approaches. *Computational materials science, 136*, 85-101.

Yoshida, K., & Morigami, H. (2004). Thermal properties of diamond/copper composite material. *Microelectronics Reliability, 44*(2), 303-308. doi:10.1016/S0026-2714(03)00215-4

Zalamea, L., Kim, H., & Pipes, R. B. (2007). Stress transfer in multi-walled carbon nanotubes. *Composites Science and Technology, 67*(15-16), 3425-3433. doi:10.1016/j.compscitech.2007.03.011

Zhang, D., & Zhan, Z. (2016). Strengthening effect of graphene derivatives in copper matrix composites. *Journal of Alloys and Compounds, 654*, 226-233.

Zhang, H., Zhao, Y., Yan, Y., Fan, J., Wang, L., Dong, H., & Xu, B. (2017). Microstructure evolution and mechanical properties of Mg matrix composites reinforced with Al and nano SiC particles using spark plasma sintering followed by hot extrusion. *Journal of Alloys and Compounds, 725*, 652-664.

Zhang, X., Li, W., Ma, J., Li, Y., Deng, Y., Yang, M., . . . Dong, P. (2020). Temperature dependent strengthening mechanisms and yield strength for CNT/metal composites. *Composite Structures*. doi:10.1016/j.compstruct.2020.112246

Zhang, Z., & Chen, D. (2006). Consideration of Orowan strengthening effect in particulate-reinforced metal matrix nanocomposites: A model for predicting their yield strength. *Scripta Materialia, 54*(7), 1321-1326. doi:10.1016/j.scriptamat.2005.12.017

Zhang, Z., & Chen, D. L. (2008). Contribution of Orowan strengthening effect in particulate-reinforced metal matrix nanocomposites. *Materials Science and Engineering: A, 483-484*, 148-152. doi:10.1016/j.msea.2006.10.184

Zhao, B., Yadian, B., Li, Z., Liu, P., & Zhang, Y. (2009). Improvement on wettability between carbon nanotubes and Sn. *Surface Engineering, 25*(1), 31-35.

Zhao, C., & Wang, J. (2014). Fabrication and tensile properties of graphene/copper composites prepared by electroless plating for structrual applications. *Physica Status Solidi (A), 211*(12), 2878-2885.

Zhu, L., & Narh, K. A. (2004). Numerical simulation of the tensile modulus of nanoclay-filled polymer composites. *Journal of Polymer Science Part B: Polymer Physics, 42*(12), 2391-2406. doi:10.1002/polb.20112